Development of micro-actuators and micro-sensors for the on-chip interrogation of cells and *in vitro* generated tissues

by

Sasha Cai Lesher-Pérez

A dissertation submitted in partial fulfillment
of the requirements for the degree of
Doctor of Philosophy
(Biomedical Engineering)
in The University of Michigan
2015

Doctoral Committee:

Professor Shuichi Takayama, Chair

Professor Mark A. Burns

Professor Raoul Kopelman

Professor Gary D. Luker

Professor Mary-Ann Mycek

Assistant Professor Sunitha Nagrath

Dedication

This dissertation is dedicated to my mother and father: Jeanett Pérez-Lesher and Kevin J. Lesher.

To my mother for paving forward my path of opportunities and growth, while bestowing on me the gifts of curiosity and exploration, and providing me with unending support.

To my father, in life and memory, has remained one of my greatest role models, all the while allowing me to grow with those precious words: “And we are put on earth a little space,

That we may learn to bear the beams of love;”

This dissertation is also dedicated to my grandparents: Argemiro Pérez, Maria Vitalia Arguelles, Nancy Lesher, and Jay Lesher, for all their work and sacrifices to get our families where they are, for teaching me so much about the world, myself, and giving me the gift of a wonderful, caring family.

Finally, I would like to dedicate this dissertation to Elena Garcia, for being part of me throughout this process, and embarking with me on our next adventure. Looking forward to “When I get older, losing my hair, many years from now.” Hopefully you will still be sending me a valentine, birthday greetings, bottle of wine…

Acknowledgements

I would like express my sincere gratitude to my advisor, Dr. Shuichi Takayama, for all his support and guidance. His enthusiasm and excitement about new ideas and science has been a continual reminder of why I came to Michigan to pursue my doctorate under his tutelage. His continual kindness, ingenuity and open door policy has given me the needed support to continue persevering through this process. He allowed me the space, time, and support to explore for myself and learn while always giving me a kind ear, and help adjusting my trajectory when I needed it. He has imparted truly valuable lessons on how to pursue research, and explore interesting ideas by focusing on the two extremes of the bell shaped curve of ideas - whether the foolhardy, simple ideas or the technically complex, mystifying ones. As he simply put it to me one day, "these extremes are the revolutionary ones, everything in between is just okay". I would also like to express my appreciation to all my committee members, Dr. Mark A. Burns, Dr. Raoul Kopelman, Dr. Gary D. Luker, Dr. Mary-Ann Mycek, Dr. Sunitha Nagarth for their support and guidance through this dissertation process. I would like to give an especially big thank you to Dr. Gary D. Luker, his feedback, discussions, positive attitude, and approach to research always helped give me clarity and focus through these years. I would like to thank all my lab mates, current and former, in the Takayama Lab over the years for their help and friendship. It has been a great privilege to share in your professional and personal lives, with so many of you, including but not limited to: Amy Hsiao, Andreja Jovic, Angela Dixon, Arlyne Simon, Bobak Mosadegh, Brendan Leung, Byoung Choul Kim, Cameron Yaminishi, Cedric Bathany, Chao Zhang, Christopher Moraes, Chuan-Hsien Jason Kuo, Chungmin Han, David Lai,

Eric Enace, Ge-ah Kim, Geeta Mehta, Hossein Tavana, Jihye So, John Frampton, Joseph Labuz, Josh White, Joong-Yull Park, Joyce Han-Ching Chiu, Madhuresh Sumit, Mayank Agarwal, Mayte Brown, Minsub Han, Nick Douville, Priyan Weerappuli, Roberto Miguez, Ryuji Yokokawa, Sanda Mong, Se Joong Kim, Steve Cavnar, Sung-Jin Kim, Taisuke Kojima, Taylor Petri, Tejash Patel, Tom Bersano-Begey, Toshiki Matsuoka, Wansik Cha, Yan-Chen Liu, Yi-Chung Tung, and Yu-suke Torisawa. I would like to give a special thank you to Dr. Sung-Jin Kim, Dr. Christopher Moraes, Dr. Brendan Leung, Dr. Bobak Mosadegh and Dr. Andreja Jovic, for their great friendship over the years, as well as all the mentoring, collaborations, support and insight into research and help molding me and my time in the doctoral program by being model scientists and mentors. I would also like to give an extra thank you to Priyan Weerappuli for all the riveting conversations, late night collaborations, and coffee runs. I would like to acknowledge the people who co-authored publications with me that comprise this dissertation: Dr. Sung-Jin Kim, Priyan Weerappuli, Chao Zhang, Dr. Brendan Leung, Dr. Christopher Moraes, Dr. Chuan-Hsien Jason Kuo, Sanda Mong, Taisuke Kojima.

I would also like to thank all the staff of the BME department, particularly Maria Steele, Mayte Brown, Kathy McCrumb, Dana Jackson, Chuck Nicholas, and Brandon Baier for all their work and help over the years, and making everything run so well.

My time at Michigan led to many wonderful friendships and experiences. I cannot give enough thanks to all those people whom provided so much friendship, love, time and energy and have made my time here so memorable. I would like to give an especially big thank you to Dr. André Monteiro da Rocha for not only your friendship and amazing meals, as well as your collaboration, suggestions and guidance these years.

I would like to extend the most outrageous, vaudevillian, food-wine-beer indulged thank you to Iverson C. Bell III, Garen Vartanian, and Erik Yusko. You three not only provided great adventures and opportunities for me to enter into dance-offs or conga lines, but also provided great times, ubiquitous laughter, hot beats, good cooking, and so much more, making this path endurable, and delightful – "ain't nobody fresher than my … clique".

A huge, huge thank you to **all my family**, including Anita, Sebastian, and Dario Gonzalez, Luz Adriana Camacho-Seidensticker, John Seidensticker, Chuck Stephens, Tomoko Sakita, Kunihiko Imamura, Jim, Mary, Will, Paul, and Leah Escalante, and Alfonso, Patty, Alex, Martin, and Camila Gutierrez for being there all those years leading up to this – without you this would not be possible. I would like to extend a tremendous thank you to my mother for everything you have done, to help me get here, become the person I am, and for being a continuous inspiration, in science and in life. Finally, thank you to Elena Garcia for patiently waiting for me, your constant reassurance, support, love, and inspiration.

Contents

List of Figures

List of Tables

Abstract

Microscale systems enable interrogation of biological mechanisms beyond the capacity of conventional macroscale techniques. The large surface-to-volume ratio of microscale platforms allows investigators to better control the spatial and temporal microenvironment presented to biological samples, manipulating samples at scales reminiscent of their native microenvironments. This research describes microscale technologies to advance the design, complexity, and control of tissue culture microenvironments in three areas – chemical stimulation, regulating cell culture dimensionality, and oxygen monitoring. These tools improve *in vitro* models to better emulate the native biological response.

To regulate temporal patterns of biochemical stimulation I developed an autonomous microfluidic oscillator circuit that enables dynamic control of delivered fluids without external control signals. This work produced to (1) a practical system to modulate the duty cycle of an applied stimulus in a user-defined manner without requiring modification of the device itself; and (2) a method to couple multiple independent oscillators together to ensure uniformity of experimental parameters, such as frequency and duty cycle, across multiple devices. In other work, reproducibility of three-dimensional spheroid cultures was achieved by culture additives to generate increasingly complex, and robust microscale cultures. We also developed dispersible

microsensors for tissue culture oxygen measurements. When recreating physiologic microenvironments, it is critical to monitor and quantify the presence of oxygen. The untethered biocompatible oxygen sensors can be embedded or dispersed within diverse culture conditions for the real-time/continuous detection of oxygen *in vitro*. Dispersible microsensors were used to visualize the oxygen environment within in vitro tumor models, which allow for the informed generation of tumor models to more accurately capitulate the necessary oxygen environments.

Chapter 1: Introduction

Animal studies of development, homeostasis, and disease mechanisms is a critical step in understanding, predicting and eventually controlling biological function in humans. However, such *in vivo* models can be expensive, highly variable, difficult to manipulate, and experimental results can often be confounded or challenging to interpret. Animals, are in the end, not humans. As a result, in the pharmaceutical industry for example, *in vivo* studies require exorbitant resources but often fail to translate promising *in vitro* results for drug compounds to clinically viable solutions[1].

The other spectrum of understanding human biology is to use *in vitro* culture of human cells in a dish. While such systems can utilize actual human cells, static Petri dish culture is simply unable to capture the structural, mechanical, chemical, and communicative complexity of *in vivo* systems. A diversity of engineered tissue culture strategies have been generated to bridge this gap, and recent efforts have focused on making these models more relevant by recreating various aspects of the cellular microenvironment. Microengineered strategies have been implemented for the dynamic control and increased definition of the cellular microenvironment[3]. The resulting microscale systems are well-positioned for interrogating aspects of cellular biology due to the favorable cell-to-tissue level scaling domain[4].

The objective of this thesis research was to develop microscale technologies to advance the design, complexity, and control of tissue culture microenvironments for improved biomedical research. Specifically, we cover three areas – stimulation, monitoring, and culturing

dimensionality – we believe tool sets are needed for the development of improved, surrogate *in vitro* models to better emulate the native biological response. Chapters II and III describe the development of microfluidic oscillators for recreating physiological fluid flows and for cellular interrogation. These microfluidic oscillators are developed for increased practicality and utility in a non-microtechnology lab setting. To this end, our work led toward (Chapter II) development of an approach through which the duty cycle of an applied stimulus could be defined by the end-user without requiring modification of the device itself[5]; (Chapter III) coupling independent oscillators to ensure uniformity of experimental parameters, such as frequency and duty cycle, across multiple devices. Part 2, comprised of Chapter IV and V, respectively covers the development of robust methods for 3D spheroid tissue generation, and stable micro-scale sensors for real-time, continuous monitoring of oxygen levels within a diversity of tissue culture microenvironments. Chapter IV focuses on the high-throughput, reproducible spheroid cultures using additive supplements in hanging drop plate arrays[6]. Chapter V describes the development of stable micro-scale sensors, or microsensors, to perform long-term, continuous, real-time monitoring of oxygen levels within a diversity of tissue culture microenvironments. Our work generated the robust microfluidic-based fabrication of biocompatible, dispersible, PDMS micro-bead sensors. Paired with a phase fluorimetric imaging modality, these microsensors demonstrated reliable measurements, easy incorporation into various cell culture platforms, and capacity as real-time oxygen sensors. These microsensors enabled the spatial mapping of oxygen in cell-patterned hydrogels, allowing us to demonstrate the effect culture systems have on oxygen levels within the tissue cultures.

1.1 References

[1] Williams CH, Hong CC. Multi-step usage of in vivo models during rational drug design and discovery. Int J Mol Sci 2011;12:2262–74. doi:10.3390/ijms12042262.

[2] Huh D, Matthews BD, Mammoto A, Montoya-Zavala M, Hsin HY, Ingber DE. Reconstituting Organ-Level Lung Functions on a Chip. Science 2010;328:1662–8. doi:10.1126/science.1188302.

[3] Young EWK, Beebe DJ. Fundamentals of microfluidic cell culture in controlled microenvironments. Chem Soc Rev 2010;39:1036–48. doi:10.1039/b909900j.

[4] Warrick JW, Murphy WL, Beebe DJ. Screening the Cellular Microenvironment: A Role for Microfluidics. IEEE Rev Biomed Eng 2008;1:75–93. doi:10.1109/RBME.2008.2008241.

[5] Lesher-Perez SC, Weerappuli P, Kim S-J, Zhang C, Takayama S. Predictable Duty Cycle Modulation through Coupled Pairing of Syringes with Microfluidic Oscillators. Micromachines 2014;5:1254–69. doi:10.3390/mi5041254.

[6] Leung BM, Lesher-Perez SC, Matsuoka T, Moraes C, Takayama S. Media additives to promote spheroid circularity and compactness in hanging drop platform. Biomater Sci 2015;3:336–44. doi:10.1039/C4BM00319E.

Chapter 2: Predictable Duty Cycle Modulation through Coupled Pairing of Syringes with Microfluidic Oscillators

2.1 Introduction

Emerging interest in microfluidic machines that directly utilize fluidic energy to execute core operations has prompted the development of self-regulated machines that, by virtue of their autonomous operation, have also garnered much attention as potential platforms for basic biomedical research [1–3].

Biological and physiological systems are fundamentally regulated by oscillatory processes operating at discrete spatial and temporal scales. Our understanding of these systems, consequently, has benefited from the development of pulsatile stimulation techniques capable of manipulating the temporal dynamics of these processes and investigating the role of timing within them. Historically, the *in vitro* study of these processes in cultured cells was advanced primarily by two types of assays: one in which a single stimulus is bath-applied and later washed off (e.g., pulse-chase analysis [4,5], and BrdU "birth dating" [6]); and one in which a continuous long-term temporal stimulation pattern is applied by way of an external control apparatus [7]. Advancements in microfluidic technology have catalyzed the translation of such assays, in parallel with the development of novel counterparts, to forms supported by these emerging micro-scale—"lab-on-a-chip"—platforms [8–11].

Microfluidic devices often emulate electronic circuitry and utilize integrated conduits and embedded valves to direct and manipulate fluid flows. The control systems underlying their

operation, however, have typically remained external from the fluidic devices themselves [12–14]. An awareness that this rise in peripheral equipment cost may limit "next-generation" microfluidic systems has motivated the development of autonomous, pre-programmed, fluidic systems [1,12–17]. Foremost among these is the microfluidic oscillator [18].

Not unlike how electronic oscillators were among the first broadly adopted automated electrical circuits; self-oscillating microfluidic devices provide a simple, yet useful, first target for microfluidic automation [1,2] as evidenced by the growing body of literature describing experimental methods, wherein cells cultured within micro-devices are chemically stimulated in a pulsatile, rather than continuous, manner [8,10,19,20]. One such method for cellular interrogation modifies stimulation events by altering the duration of an applied stimulus and/or rest period; effectively manipulating the oscillation frequency and duty cycle of the stimulatory system [19]. Through this approach, it has been observed that different responses may be elicited from the same population of cells by manipulating these stimulatory parameters.

The work presented here was motivated by the questions: how can a single microfluidic oscillator circuit be designed to best support multiple stimulatory frequencies and rest periods; and how can this be done in a manner that is easy to understand and perform by non-microfluidic experts? We have previously demonstrated the ability to alter oscillation frequency by modifying flow rate, and to alter duty cycle by modifying the device itself [1,2]. As the technical burden of repeatedly designing and fabricating different devices for each desired duty cycle is both difficult and tedious; we asked if a continuous and predictable modification of duty cycle could be achieved by simply modifying the syringes used to provide volumetric inflow.

The challenge associated with modifying volumetric inflow rate lies in the effect this may have upon the threshold opening pressure of each valve [21]. Due to the complexity of the relationship

between volumetric flow rate and duty cycle, predicting the duty cycle resulting from a change in volumetric flow rate is not trivial. Additional challenges arise if two syringe pumps are used to generate differing volumetric inflows, owing largely to inherent pump-to-pump variability and general inflow rate unsteadiness that may produce unstable oscillations [22]. Here we report the predictable modulation of duty cycle using two syringes mounted upon a single syringe pump such that volumetric flow rate ratio and fluidic capacitance are coupled. This setup is advantageous in that it allows duty cycle to be considered simply as a function of the volumetric inflow rate ratio; requiring no modifications of the microfluidic circuit to robustly produce distinct duty cycles.

2.2 Working Principle

The microfluidic oscillator functions by converting two constant volumetric flow rate inflows to one oscillatory outflow through the activity of two normally-closed three-way valves that generate oscillations in fluid outflow through the alternate obstruction of each inflow (Fig. 2-1).

Briefly, if we denote the two valves *valve 1* and *valve 2*, and arbitrarily assume that *valve 2* is initially in an open position—allowing fluid to flow across it; a portion of the outflow from *valve 2* will be diverted from its drain terminal to the gate terminal of *valve 1*. The gate terminal refers to the conduit leading to the region below the membrane valve unit. The accumulation of fluid within this region supplies the gate pressure of *valve 1* (P_{G1}); preventing the downward deflection of the membrane, and consequently preventing *valve 1* from transitioning to an open position while P_{G1} exceeds the source pressure of *valve 1* (P_{S1}) generated by the accumulation of fluid in the portion of the valve upstream from the *valve 1* gate.

When P_{S1} has surpassed the sum of P_{G1} and the inherent pressure threshold of *valve 1* (P_{th1}), determined by the specific mechanical properties of the membrane, the membrane is deflected

downward, and fluid is allowed to travel through *valve 1*. A portion of this outflow is then diverted from its drain terminal to the gate terminal of *valve 2*, as the outflow from *valve 1* had been diverted previously, and supplies the gate pressure necessary to force the accumulation of fluid upstream of *valve 2*, until the difference between P_{S2} and P_{G2} has exceeded P_{th2} (Fig. 2-1a,b). The coordination of these processes, resulting in the anti-synchronized opening and closing of both valve units, produces an oscillatory outflow (described in greater detail in previous work [2,21]).

Functionally, as the gate pressure of the valve regulating one flow is itself regulated by the volumetric outflow rate across the other, we assume the following characteristic:

$$Q_{in} = C \times \frac{dP}{dt} \tag{1}$$

$$Q_{in} = C \times \frac{P_{th}}{T_{off}} \tag{2}$$

This expression, where Q_{in}, C and P represent inflow rate, fluidic capacitance, and pressure respectively, may be expanded to describe the threshold-dependent mechanism underlying the functionality of the valves. Conceptually, the transition between a closed-to-open or open-to-closed valve-state is governed by the values of P_{th} and P_G set by the mechanical properties of the membrane and buildup of fluid pressure below the membrane (Fig. 2-1b), respectively, and the rate at which fluid pressure builds within the valve region above the membrane (P_S) [2]. The relationship between inflow rate and capacitance, thus, may be used to determine duty cycle as a function of time:

$$\frac{T_1}{T_1 + T_2} = \frac{\frac{C_1 \times P_{th1}}{Q_1}}{\left[P_{th1} \times \frac{C_1}{Q_1}\right] + \left[P_{th2} \times \frac{C_2}{Q_2}\right]} \tag{3}$$

Under symmetric flow conditions, $Q_1 \cong Q_2$, where the mechanical properties of the membrane and valve compartments are preserved across both valves, the assumption is $P_{th1} \cong P_{th2}$ and $C_1 \cong C_2$, allowing us to consequently define duty cycle solely as a function of volumetric flow rate.

$$\frac{T_1}{T_1 + T_2} \approx \frac{Q_1}{Q_1 + Q_2} \tag{4}$$

Equation (4) depicts an attractive relationship that relates duty cycles simply to volumetric inflow ratios. By this definition, the introduction of asymmetry to the volumetric inflow rates of each fluid, Q_i, would produce asymmetric duty cycles. However, in asymmetric conditions where $Q_1 \neq Q_2$ (e.g., $Q_1 < Q_2$), the syringe supplying the greater volumetric inflow (Q_2) will result in a greater threshold pressure for the valve regulating the lesser volumetric inflow, and consequently, $P_{th1} > P_{th2}$. The presence of this asymmetry suggests that the use of two identical syringes, evacuated at asymmetric linear velocities, would rely upon a complex balance between Q_{in}, C, and P such that the duty cycles produced may not be accurately modeled by Equation (4).

One way to maintain the relationship shown in Equation (4) would be to modulate C_i together with Q_i so that $P_{thi} \times C_i \approx$ constant. One way to achieve this conveniently is by mounting two plastic syringes of different cross-sectional area on one syringe pump (Fig. 2-2), and utilizing the compliance of the syringe components [23] and resulting capacitive differences of the syringes [12]. Within the described system, as syringe outflow rate is a function of velocity and syringe cross-sectional area, and as both syringes are evacuated at the same linear velocity, we may further refine our definition of duty cycle as being a function of syringe diameter (Fig. 2-2b). By using syringes of different diameters, we apply Equation (4) and demonstrate predictability of duty cycle values as a function of the combination of syringes used (Table 2-1).

2.3 Materials and Methods

Master Mold Fabrication

Microfluidic oscillator master molds were fabricated upon 4″-silicon wafers using the negative photoresist, SU-8 (MicroChem, Newton, MA, USA). Following air-cleaning of the wafer, SU-8 2075 photoresist was deposited on the wafer and spin-coated at 500 rpm (acceleration of 440 rpm/s) for 10 s and at 2100 rpm (acceleration of 440 rpm/s) for 30 s. The coated wafer was then placed on a hotplate for pre-exposure baking at 65 °C for 5 min, 95 °C for 20 min and then allowed to gradually cool to room temperature by allowing it to remain on the hotplate after the plate was turned off. The SU-8 substrate was then exposed with conventional UV (~17 mJ/cm^2) for 30 s using a mask aligner (Hybrid Technology Group), and then placed on a hotplate for post-exposure baking at 65 °C for 5 min, 95 °C for 10 min and then allowed to gradually cool to room temperature as before. Unexposed regions of photoresist were dissolved by repeatedly immersing the wafer in fresh SU-8 developer solution (MicroChem, Newton, MA, USA) for 60 s intervals until all non-exposed/cross-linked regions of SU-8 were removed. The completed mold was then placed within a gravity convection oven (DX-400, Yamato Scientific America, Santa Barbara, CA, USA) for 15 min at 120 °C and, upon returning to room temperature, was treated (silanized) in a desiccator for 1 h in the presence of vaporized tridecafluoro-1,1,2,2-tetrahydrooctyl-1-trichlorosilane (United Chemical Tech., Bristol, PA, USA).

Microfluidic Oscillator Fabrication

The microfluidic oscillator device consists of three polydimethylsiloxane (PDMS) layers assembled as previously described [1,2]. Briefly, the device features (100 μm height) were imprinted in the top and bottom layers, and a PDMS membrane (target thickness: 20 μm) was positioned between them (Fig. 2-1).

1:10 PDMS (Sylgard 184, Dow Corning, Midland, MI, USA) was poured onto the master mold and allowed to cure within a gravity convection oven at 60 °C for 6 h. The cured PDMS slab was then removed from the mold and cut into individual device layers. Concurrently, PDMS membranes were fabricated by spin-coating 1:10 PDMS onto glass slides pre-treated with silane as before. PDMS membranes were then cured within a gravity convection oven for 5 min at 120 °C and 10 min at 60 °C. Prior to final assembly, a 2-mm biopsy punch was used to remove PDMS from the inlet and outlet ports of the top device layer. The bottom layer and membrane were then treated by plasma oxidation (Covance MP, FemtoScience, Hwaseong-si, Gyeonggi-do, South Korea) to facilitate bonding and, following bonding, were then placed in a gravity convection oven at 120 °C for 5 min and at 60 °C for 10 min. Thru-holes were then made in the membrane to allow fluid communication between the top and bottom device layers, using a 350-μm biopsy punch (Ted Pella Inc., Redding, CA, USA). The top layer was then treated by plasma oxidation to facilitate bonding with the membrane-bottom layer assembly. Following treatment, but preceding bonding, the normally closed region of the top layer was "deactivated" by being brought into direct contact with an unoxidized PDMS "stamp". Following final bonding, assembled devices were incubated for 2 min within a gravity convection oven at 120 °C.

Microfluidic Oscillator Testing and Data Processing

Microfluidic oscillators were tested by connecting pressure sensors (Model 142PC05D, Honeywell, NJ, USA) at the device inlets via Tygon tubing (Saint-Gobain™ Tygon™ R-3603 Clear Laboratory Tubing, Saint-Gobain Performance Plastics, Akron, OH, USA) to measure source pressure. Source pressure data was collected for both valves to quantify pressure buildup and release corresponding to fluid accumulation and evacuation, respectively, through the valves; our previous work highlighted the relationship between source pressure and drain pressure [24]. The occurrence of fluidic oscillations and the coincident timing of these oscillations relative to source pressure profiles were verified visually. All subsequent quantification and assessment, however, was performed using source pressure data. Data was obtained at a sampling rate of 1000 Hz, every 100 data points were averaged (resulting in 1 data point per 100 ms), and stored using LabVIEW (National Instruments, Austin, TX, USA). Data was recorded for a minimum of four hours, of which the data acquired during the first hour for each condition was examined and discarded to ensure the volumetric flow and capacitance of the fluidic system had stabilized, and only the subsequent time (three hours) was assessed. Syringe pumps (Model KDS220, KD Scientific, Holliston, MA, USA and Model Fusion 200, Chemyx, Stafford, TX, USA) were used to provide constant volumetric flow to the device. One input, a 3 mL syringe (*Syringe 1*) remained connected to one inlet port for the entirety of the study, while the second (*Syringe 2*) was allowed to alternate between 3 mL, 10 mL, 30 mL and 60 mL plastic syringes (Becton, Dickinson and Company, Franklin Lakes, NJ, USA). The syringe pump was programmed with total volumetric inflow rates appropriate for each syringe pairing, such that $Q_2 \geq Q_1$ and $Q_2 + Q_1 = Q_{total}$.

Voltage data were collected using LabVIEW and processed, in part, using the open-source peakdet [25].

2.4 Results and Discussion

Predictive Duty Cycle Control

Using Equation (4), we calculated and experimentally measured duty cycle as a function of volumetric flow rate ratios achieved through the simple utilization of two plastic syringes of different cross-sectional area mounted on a single syringe pump (Table 2-1). The estimates generated by Equation (4) agreed with experimental observations.

Highlighted values represent syringe combinations studied experimentally. The duty cycle values presented are calculated with respect to *Syringe 2*. Utilizing this system, we succeeded in achieving duty cycles ranging from 50% to 90% (Fig. 2-3a), reproducible across multiple devices (n = 3) (Fig. 2-3b).

Mounting Syringes on Separate Syringe Pumps Produces Unstable Duty Cycles

To verify that Equation (4) did not accurately predict duty cycles produced through the sole modification of volumetric flow rate; two identical syringes were mounted on two independent syringe pumps and tested for their ability to produce predictable duty cycles. Flow was initiated at a total volumetric flow rate of 20 μL/min, and the resulting duty cycles were recorded and analyzed. The duty cycles produced via this setup deviated from their predicted values and were unstable, appearing to shift sporadically from one oscillation pattern to another, interspersed by brief periods during which the oscillations would appear stable. This instability was also present at additional total volumetric inflow rates (data not shown), and ultimately affected the predictability of the duty cycles produced (Fig. 2-4).

The sources of the observed deviation and instability are likely two-fold. The deviation likely arises as a consequence of the asymmetric linear pressures experienced by each syringe that result in a change in relative P_{th}, but not in C; necessary for performing the reduction yielding Equation (4), and consequently, for the simplified and accurate prediction of duty cycle. The source of the observed instability at a specific flow rate ratio may be multifaceted; deriving from differences in manufacturing of the pumps themselves, differences in their calibration or age, and general unsteadiness inherently observed in syringe pumps [22,26]. As the presence of variability between syringe pumps is unavoidable, the use of multiple syringe pumps presents an inherent risk that predictability of the resulting duty cycle will be adversely effected due to an uncoupling between the pump-derived variability experienced by each individual syringe. Mounting multiple syringes upon a single syringe pump, however, ensures that each syringe experiences similar pump-derived variability. This coupling then ensures that slight instabilities in linear output are experienced simultaneously by both syringes; resulting in a predictable and stable duty cycle.

Maximum Pressure Profile Remains Relatively Constant

The use of asymmetric inflow rates generated by mounting two syringes of varying diameter onto a single syringe pump alters the pressure profiles generated from each valve (Fig. 2b). As we are unable to directly measure gate pressure within our experimental system, we use the previously established approximation, where $P_{S2} \cong P_{G1}$ and $P_{S1} \cong P_{G2}$ at the time of an open-to-close transition [2]. By this approximation, we conclude the asymmetric P_{th} values observed, even under extreme asymmetric conditions ($|P_{th1} - P_{th2}| < 2$ kPa), are far below those reported in previous work ($|P_{th1} - P_{th2}| < 55$ kPa) utilizing asymmetric valve units [8].

The P_{max} values recorded for each valve under the examined flow conditions are equivalent under symmetric volumetric inflow rates, but diverge from these values as the asymmetry between the two inflow rates is increased (Table 2-2).

Because the transition of each valve from a closed-to-open state is triggered by the accumulation of sufficient fluidic pressure (P_{max}); the initial outflow velocity from each valve is higher (Q_{max}) relative to the stabilized baseline velocity subsequently achieved [24]. The lower P_{max} values observed within this system, relative to values previously-reported [2], suggests a reduction in Q_{max} and, thus, in the magnitude of the transient fluctuation in flow velocity accompanying the transition of each valve from a closed-to-open state. Despite this reduction, as fluidic shear is known to influence the morphological and phenotypical properties of cultured cells and tissues, the mere presence of this fluctuation may nonetheless represent a parameter which must be considered when utilizing this device for the performance of biological analyses.

A comparison of P_{max} values across both valves in one device demonstrates P_{max} values for *valve 1* increase relative to P_{max} values for *valve 2* in proportion to the degree of asymmetry between the inflow rate ratios across the two valves. All data presented is derived from one device, as inter-device variability led to differing absolute P_{max} values across devices. Similar trends, however, were observed across all devices examined.

Syringe Properties Influence Capacitance

Syringe size has previously been shown to impact overall compliance in a syringe-driven system, where, independent of material and design, increases in syringe diameter are correlated with increases in syringe compliance [27]. This effect, underappreciated within the field of microfluidics, was observed within our experimental system (Fig. 2-5), and presented a source

for concern, as external capacitance could influence the period of the oscillatory output [24]. The good agreement between the duty cycles predicted by the simplified Equation (4) and the actual observed duty cycles are explained by looking at Equation (3), where there is an approximate inverse relationship between C and P_{th} observed under asymmetric inflow rates (described in greater detail below).

Different Asymmetric Inflow Rates at Constant Total Volumetric Inflow Rate Produce Distinct Periods

Previous work provides an approximation of the off-time for each valve that can be used to estimate oscillatory period [2], thereby assisting in contextualizing any observed shift in period:

$$t_{off-i} = \left(\frac{C}{Q_{in}}\right) \times P_{th-i} \tag{5}$$

We calculated P_{th} using experimental data collected under multiple inflow conditions. We found that under asymmetric flow regimes, P_{th} and C exhibit an inverse relationship, where P_{th} is higher for the valve experiencing the lower flow rate (*valve 1*), lower for the valve experiencing the higher flow rate (*valve 2*) and where the absolute difference between P_{th} (*i.e.*, $|P_{\mathrm{th1}} - P_{\mathrm{th2}}|$) increases with the degree of asymmetry between the syringes used. As C is proportional to the size of a given syringe, it is consequently proportional to Q_{in}, which increases with the size of the syringe used. This finding is in agreement with previous results reported for four-way valves, where an increase in volumetric inflow rate through one valve increases calculated P_{th} for the opposite valve [21].

From Equation (5), we infer that increasing P_{th} in conditions with lower Q_{in}, will produce higher t_{off}; and that as the asymmetry between the flow rate across each valve increases, t_{off} will increase

for the valve with a lower inflow rate, producing larger oscillation periods. Using the averaged values of P_{th} and C for each respective syringe pairing, we approximated t_{off} for both valves. We then compared the calculated period approximation with experimental data (Fig. 2-6), and observed that the relationship between volumetric flow rate and period is preserved. We limited the presented period data to one device, as all devices tested exhibited similar trends, with slight variations in absolute values. Such variations may originate from differences in device size (e.g., thickness of the PDMS membrane), fabrication procedure or material batch characteristics. In addition, larger standard deviations in the period, prominent at greater asymmetric inflow rates, may also originate from fluctuations in syringe pump pressure [26].

This observation highlights the utility of our approach and underscores the motivation for this work. Mounting two syringes of the same size on two independent syringe pumps and evacuating them at two different volumetric flow rates will produce changes in P_{th}, but not in C, introducing a source of complexity to the relationship between volumetric flow rate ratio and duty cycle. Practically, this would result in the inability to reduce down to Equation (4). However, by utilizing syringes of differing diameter, volumetric flow rate-dependent changes in P_{th} are counteracted, allowing one to perform straightforward prediction of duty cycle as a function of volumetric flow rate ratio.

4.6. Estimating Rest and Stimulation Pulse Duration for Control of Rhythmic Stimulation

The described microfluidic oscillator is designed to translate two independent fluid inputs into a single oscillatory fluid output. In practice, if one input contains a fluid stimulant, and the other a neutral “wash” solution, this system may be utilized to conduct biological experiments in which a population of cells (or tissue explant) cultured downstream is presented with this fluid stimulant at a fixed concentration, and for a pre-determined period of time—referred to as the

stimulation duration (*D*); followed by a "wash"—or rest period (*R*). The functional significance of the presented asymmetric operating technique is that it allows the user to dynamically control the duty cycle of this oscillatory outflow, and in doing so, to characterize biological responses to multiple stimulation regimes characterized by variations in *D* and *R* (e.g., fixed *D* separated by variable *R*). Within a biological context, control of these parameters is critical as both have been reported to elicit distinct cellular responses [19].

Within the context of the presented device system, *D* and *R* may be calculated as a function of relative inflow rates. To do so, *C* and P_{th} for each valve must be measured with respect to its corresponding syringe and input Q_i values, respectively. Measurements of P_{th} for each valve must be conducted at two total volumetric inflow rates (we used 5 μL/min and 40 μL/min, the minimal and maximal total volumetric inflow rates, respectively) to approximate the linear relationship $P_{th-i} = m \times Q_i + b$. This relationship may then be used to approximate intermediate P_{th-i} values for different inflow rates, and for each syringe pairing. The P_{th-i}, *C*, and Q_i values may then be used, in equation (5), to determine the off-time for each valve. The sum of the off-times will estimate the periodicity of the device for a given syringe combination. By this method, a curve in general agreement with empirical data, and representing the periodicity as a function of the ratio between syringe diameters, may be generated (Figure 6). This curve may then be utilized to identify an appropriate total volumetric inflow to produce a desired *D* and *R* for the specific syringe combination being used. Conversely, this curve may also be utilized to identify the appropriate combination of syringes necessary to modify the length of *D* or *R*.

2.5 Conclusions

The volumetric flow-regulated microfluidic oscillator system described herein greatly increases the versatility and utility of our previously described micro-machine as a tool for generating and delivering pulsatile stimulation. Furthermore, in allowing users to reliably produce a desired duty cycle through the simple manipulation of volumetric inflow rate, the system described greatly reduces the barrier for adoption otherwise presented by placing the burden for "programming" the device upon the end-user. Notably, the benefit of using one syringe pump to drive both syringes is that inherent syringe pump unsteadiness and subsequent inflow fluctuations are applied to both syringes simultaneously; negating their impact on duty cycle, and resulting in a more consistent and stable oscillation.

2.6 References

[1] Mosadegh B, Kuo CH, Tung YC, Torisawa YS, Bersano-Begey T, Tavana H, et al. Integrated elastomeric components for autonomous regulation of sequential and oscillatory flow switching in microfluidic devices. Nat Phys. 2010;6:433-7.

[2] Kim SJ, Yokokawa R, Lesher-Perez SC, Takayama S. Constant flow-driven microfluidic oscillator for different duty cycles. Anal Chem. 2012;84:1152-6.

[3] Walker GM, Beebe DJ. A passive pumping method for microfluidic devices. Lab Chip. 2002;2:131-4.

[4] Jamieson JD, Palade GE. Intracellular transport of secretory proteins in the pancreatic exocrine cell. I. Role of the peripheral elements of the Golgi complex. J Cell Biol. 1967;34:577-96.

[5] Gratzner HG. Monoclonal antibody to 5-bromo- and 5-iododeoxyuridine: A new reagent for detection of DNA replication. Science. 1982;218:474-5.

[6] Dolmetsch RE, Xu K, Lewis RS. Calcium oscillations increase the efficiency and specificity of gene expression. Nature. 1998;392:933-6.

[7] Taylor RJ, Falconnet D, Niemisto A, Ramsey SA, Prinz S, Shmulevich I, et al. Dynamic analysis of MAPK signaling using a high-throughput microfluidic single-cell imaging platform. Proc Natl Acad Sci U S A. 2009;106:3758-63.

[8] Tay S, Hughey JJ, Lee TK, Lipniacki T, Quake SR, Covert MW. Single-cell NF-kappaB dynamics reveal digital activation and analogue information processing. Nature. 2010;466:267-71.

[9] Cheong R, Wang CJ, Levchenko A. High content cell screening in a microfluidic device. Mol Cell Proteomics. 2009;8:433-42.

[10] Sackmann EK, Fulton AL, Beebe DJ. The present and future role of microfluidics in biomedical research. Nature. 2014;507:181-9.

[11] Mosadegh B, Bersano-Begey T, Park JY, Burns MA, Takayama S. Next-generation integrated microfluidic circuits. Lab Chip. 2011;11:2813-8.

[12] Leslie DC, Easley CJ, Seker E, Karlinsey JM, Utz M, Begley MR, et al. Frequency-specific flow control in microfluidic circuits with passive elastomeric features. Nature Physics. 2009;5:231-5.

[13] Duncan PN, Nguyen TV, Hui EE. Pneumatic oscillator circuits for timing and control of integrated microfluidics. Proc Natl Acad Sci U S A. 2013;110:18104-9.

[14] Rhee M, Burns MA. Microfluidic pneumatic logic circuits and digital pneumatic microprocessors for integrated microfluidic systems. Lab Chip. 2009;9:3131-43.

[15] Collino RR, Reilly-Shapiro N, Foresman B, Xu K, Landers JP, Begley MR. Flow switching in microfluidic networks using passive features and frequency timing. Lab Chip. 2013;13:3668-74.

[16] Toepke MW, Abhyankar VV, Beebe DJ. Microfluidic logic gates and timers. Lab Chip. 2007;7:1449-53.

[17] Kim S-J, Lai D, Park JY, Yokokawa R, Takayama S. Microfluidic Automation Using Elastomeric Valves and Droplets: Reducing Reliance on External Controllers. Small. 2012;8:2925-34.

[18] Jovic A, Howell B, Cote M, Wade SM, Mehta K, Miyawaki A, et al. Phase-locked signals elucidate circuit architecture of an oscillatory pathway. PLoS Comput Biol. 2010;6:e1001040.

[19] Jovic A, Howell B, Takayama S. Timing is everything: using fluidics to understand the role of temporal dynamics in cellular systems. Microfluid Nanofluid. 2009;6:717-29.

[20] Korczyk P, Cybulski O, Makulska S, Garstecki P. Effects of unsteadiness of the rates of flow on the dynamics of formation of droplets in microfluidic systems. Lab Chip. 2011;11:173-5.

[21] Rooke GA, Bowdle TA. Syringe pumps for infusion of vasoactive drugs: mechanical idiosyncrasies and recommended operating procedures. Anesth Analg. 1994;78:150-6.

[22] Kim SJ, Yokokawa R, Takayama S. Microfluidic oscillators with widely tunable periods. Lab Chip. 2013;13:1644-8.

[23] Li Z, Mak SY, Sauret A, Shum HC. Syringe-pump-induced fluctuation in all-aqueous microfluidic system implications for flow rate accuracy. Lab Chip. 2014.

[24] Weiss M, Hug MI, Neff T, Fischer J. Syringe size and flow rate affect drug delivery from syringe pumps. Can J Anaesth. 2000;47:1031-5.

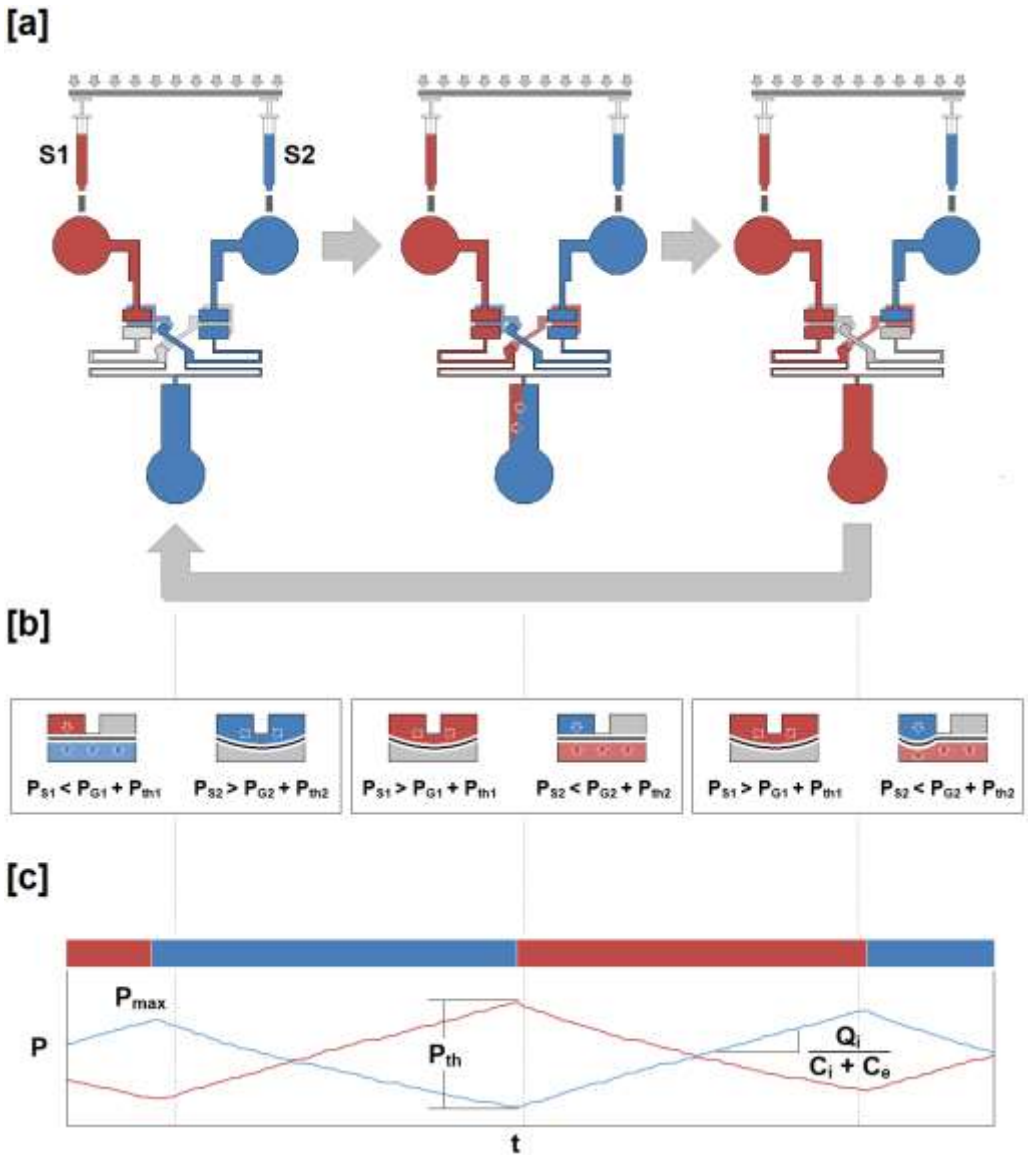

Figure 2-1: Schematic for experimental system

Schematic for the experimental system. The three panels displayed represent the behavior of the microfluidic oscillator at three time points during operation under symmetric flow conditions. (a) Two fluids (blue and red) are introduced through two syringes mounted on a single syringe pump. The fluids enter the device at a constant rate, but are converted into an oscillatory outflow when passing through the valves. (b) A cross section of each valve unit at the time points displayed in panel A. Initially, the source pressure (P_{S1}) is insufficient ($P_{S1} < P_{G1} + P_{th1}$) to displace the membrane downward, allowing the blue fluid to outflow. When the pressure has reached its maximum value (P_{max}), the membrane is displaced ($P_{S1} > P_{G1} + P_{th1}$), allowing the red fluid to outflow until sufficient source pressure (P_{S2}) has accumulated within the chamber above the opposite membrane ($P_{S2} > P_{G2} + P_{th2}$) allowing the blue fluid to outflow. (c) The time points within the pressure data time series corresponding to the valve and outflow profiles presented in panels a and b are indicated. A sample P_{max} and P_{th} are also represented, as well as the relationship between inflow rate (Q_i), internal capacitance (C_i), and external capacitance (C_e).

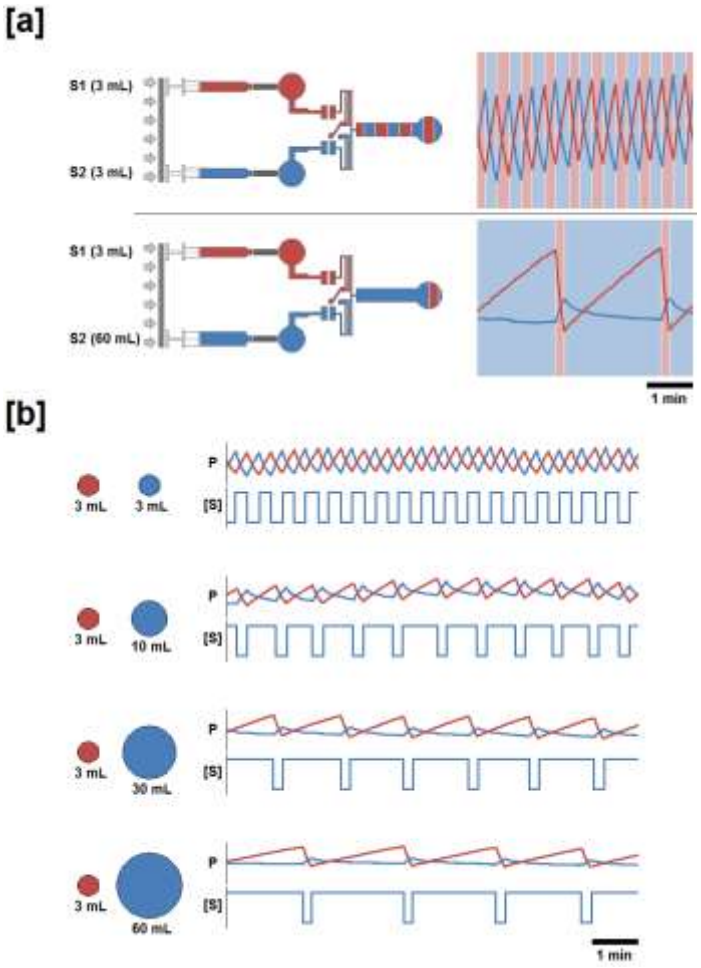

Figure 2-2: Schematic for generation of symmetric and asymmetric volumetric flow rates - changes in duty cycle and pressure profile produced as a function of syringe diameter
(a) Two sample conditions where *Syringe 1*, (red), and *Syringe 2*, (blue), are mounted on a single syringe pump. The ratios illustrated are the symmetric 3 mL:3 mL (upper) and asymmetric 3 mL:60 mL (lower). Within the experimental protocol , *Syringe 1* was held constant in all pairings while *Syringe 2* was varied to achieve symmetric (50%) and asymmetric (>50%) duty cycles; and total volumetric inflow rate remained constant. Experimentally generated pressure profile waveforms are presented against alternating background bands representing the fluid outflow profile. (b) Pressure profile and stimulation period for the four inflow ratio regimes. Pressure profiles were generated while the syringe pump was moving at a constant linear velocity such that the total volumetric inflow rate (the sum of the inflows supplied by each syringe) was maintained at a volumetric flow rate of 20 μL/min. The pressure profiles recorded (*P*) are presented above each trace representing the concentration of a fluidic stimulant ([*S*]) provided via *Syringe 2*, in the outflow.

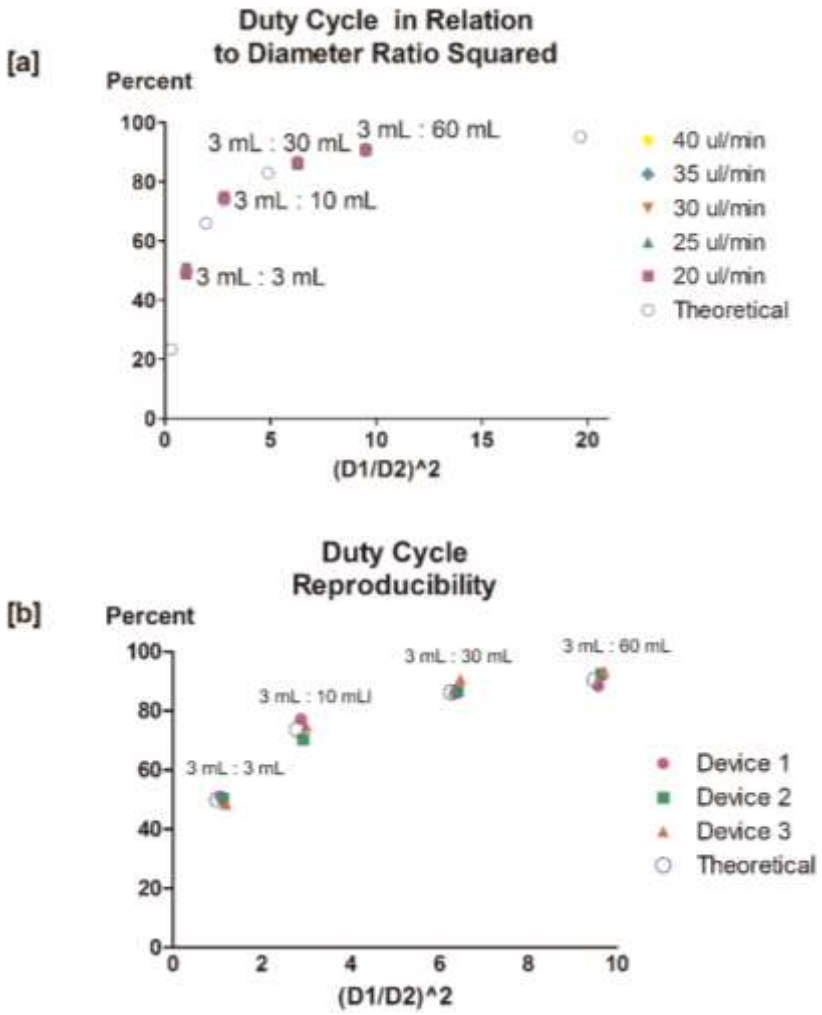

Figure 2-3: Experimental duty cycles overlap predicted values; flow rate ratio manipulation stably and reproducibly regulates duty cycle across multiple devices.
(a) Filled symbols represent duty cycle values observed and averaged across four syringe combinations and at five different total volumetric inflow rates. Unfilled blue circles represent predicted duty cycle values. All values are derived from time series data containing >6 oscillations. Duty cycle values are plotted against the squared ratio between syringe diameter (*Syringe* 2:*Syringe* 1) to illustrate the general trend observed. (b) Duty cycle data collected from multiple devices (n = 3) is presented against the squared ratio between syringe diameter (*Syringe* 2:*Syringe* 1). Filled symbols represent duty cycle values recorded and averaged across four syringe combinations for total volumetric inflow rates ranging from 5 to 40 μL/min. Unfilled circles represent theoretical (predicted) duty cycle values. All averaged values are derived from time series data containing >6 oscillations. Error bars represent the calculated standard deviation for all duty cycle values recorded from each of three devices for all tested inflow rate ranges.

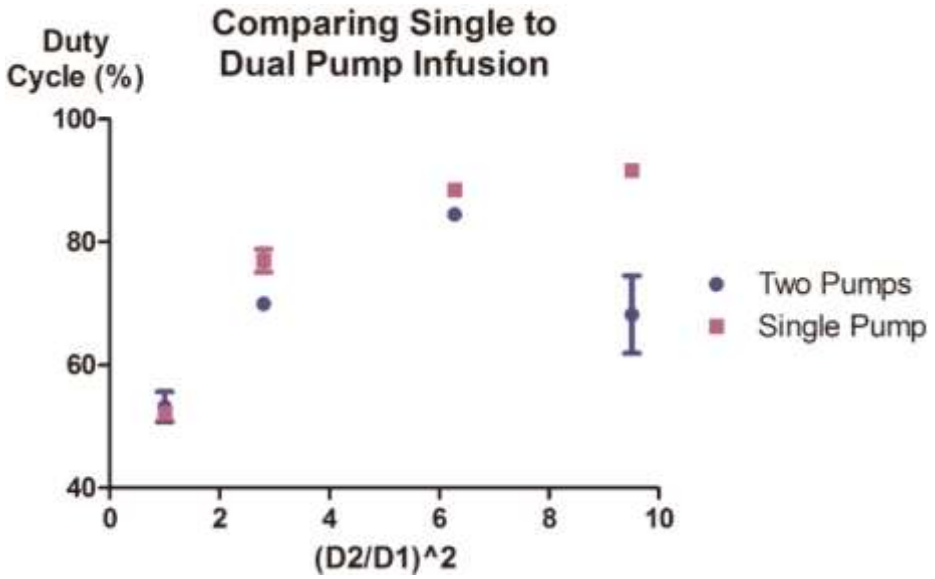

Figure 2-4: Single syringe pump setup results in more robust duty cycle control than two pump setup.

A minimum of 7 sequential oscillations were observed using two experimental setups (either comprised of a multiple syringes mounted upon a single pump or single syringes mounted upon multiple pumps) to identify reproducibility and consistency of duty cycle. The data presented was acquired using both experimental setups at a total volumetric inflow rate of 20 μL/min. Error bars represent the 95% confidence intervals for experimentally observed results. Two different syringe pump models were utilized in the multiple syringe pump setup.

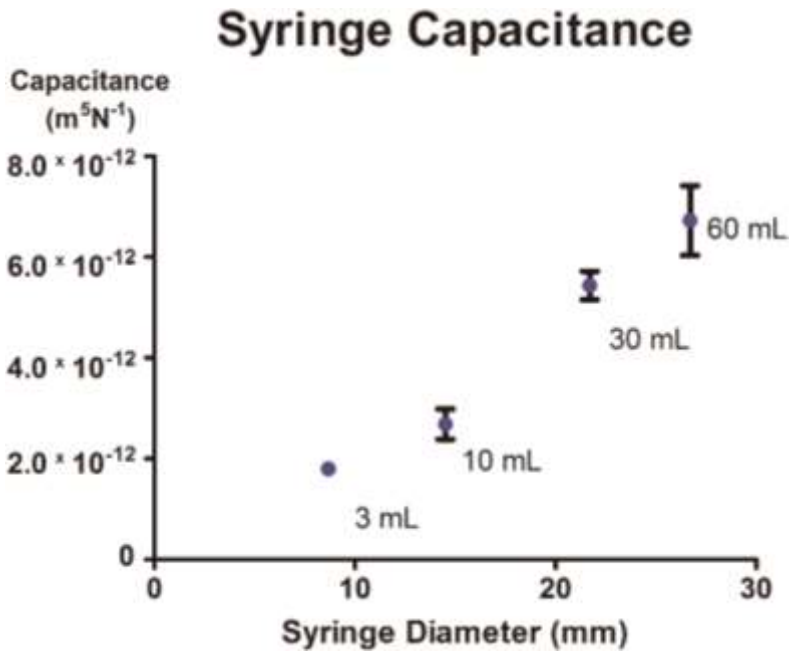

Figure 2-5: Fluidic capacitance increases significantly with increasing syringe volume. Fluidic capacitance increases significantly with increasing syringe volume. Capacitance values were averaged for individual syringes using data collected at multiple volumetric flow rates (ranging from 10 to 40 μL/min). All values are derived from time series data containing >6 oscillations, with five replicates ($p < 0.0002$). Error bars represent the 95% confidence intervals of all capacitance values obtain over multiple inflow rate ranges.

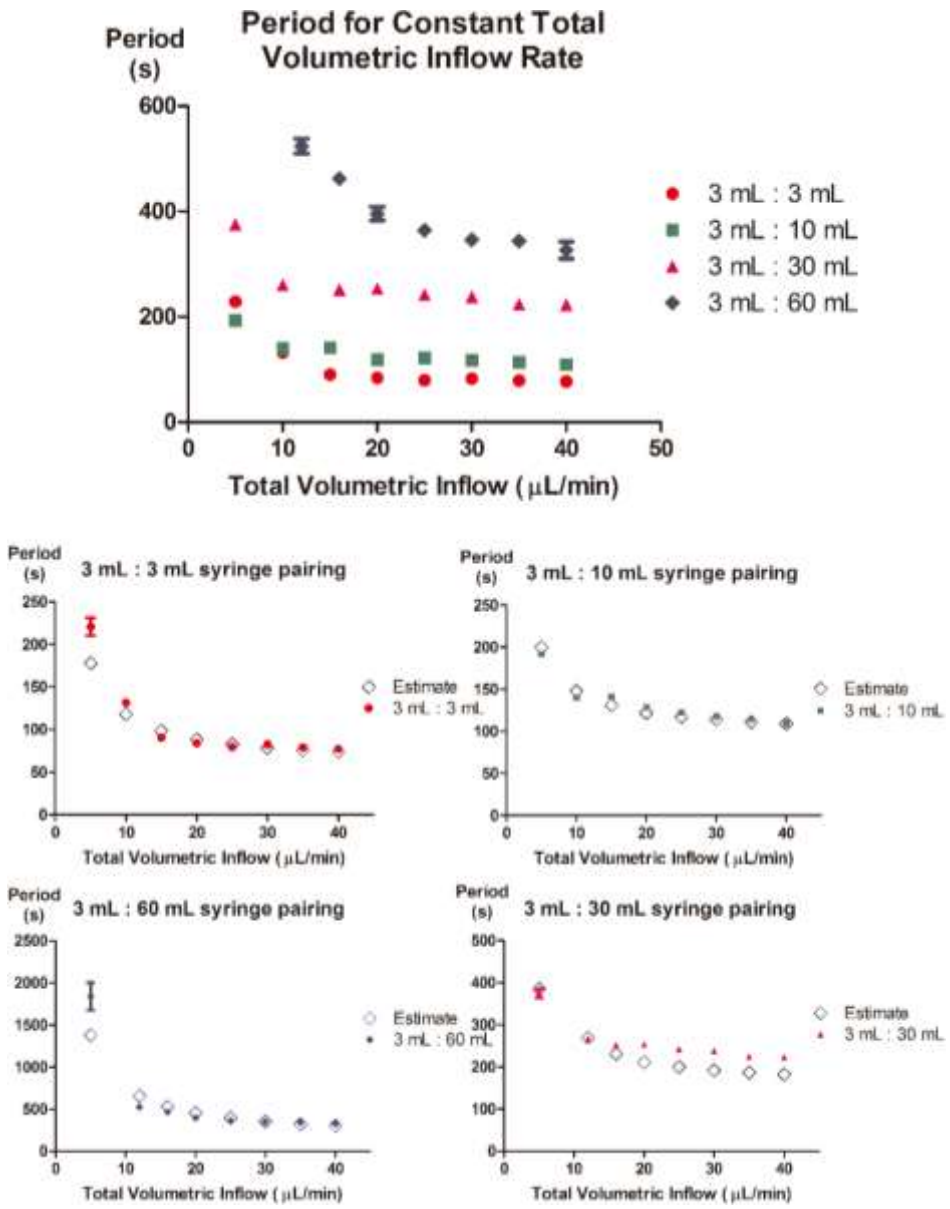

Figure 2-6: Asymmetric inflow rates produce markedly different periodicity, yet can be estimated relatively-well.

Observed period values for each syringe combination demonstrate the range of periodicities generated for each of the four combinations tested. The estimated oscillatory period was calculated by applying Equation (5) for each syringe combination; values for C and P_{th} were derived from the minimal and maximal volumetric inflow rates tested, and were used to establish a linear relationship for P_{th-i} where $P_{th-i} = m \times Q_i + b$. Predicted period values (unfilled) were then compared to the averaged measured period values (filled). All values are derived from time series data containing >12 oscillations, and error bars represent 95% confidence intervals for experimentally observed results.

Syringe 1			*Syringe 2*			**Duty Cycle (Expected)**	**Duty Cycle (Observed)**
Volume (mL)	**Diameter (mm)**	**Inflow Rate (µL/min)**	**Volume (mL)**	**Diameter (mm)**	**Inflow Rate (µL/min)**		
3	8.66	15.33	1	4.78	4.67	23.35%	-
3	8.66	10.00	3	8.66	10.00	50.00%	48.71%
3	8.66	6.80	5	12.06	13.20	65.98%	-
3	8.66	5.26	10	14.5	14.74	73.71%	74.59%
3	8.66	3.40	20	19.13	16.60	82.99%	-
3	8.66	2.75	30	21.7	17.25	86.26%	86.00%
3	8.66	1.90	60	26.7	18.10	90.48%	90.82%
3	8.66	0.97	140	38.4	19.03	95.16%	-

Table 2-1: Syringe pairing combinations for differential duty cycles

Different syringe pairings on a single syringe pump enables different duty cycles to be achieved, while maintaining a constant total volumetric inflow rate of 20 µL/min. Highlighted rows indicate those experimentally tested.

Total Volumetric Inflow Rate (µL/min)	3 mL:3 mL		3 mL:10 mL		3 mL:30 mL		3 mL:60 mL	
	Valve 1 (kPa)	Valve 2 (kPa)	Valve 1 (kPa)	Valve 2 (kPa)	Valve 1 (kPa)	Valve 2 (kPa)	Valve 1 (kPa)	Valve 2 (kPa)
20	3.30	3.34	3.49	3.32	3.51	2.76	3.67	3.04
25	4.08	4.16	4.20	4.01	4.28	3.48	4.53	3.80
30	4.77	4.92	5.03	4.83	5.20	4.28	5.44	4.58
35	5.52	5.70	5.72	5.54	6.11	5.08	6.34	5.35
40	6.31	6.52	6.52	6.29	6.98	5.86	7.18	5.94

Table 2-2: Different syringe pairing combinations produce different maximum source pressures

Larger maximum pressures observed in valve receiving smaller inflow rate.

Chapter 3: Capacitive coupling synchronizes autonomous microfluidic oscillators

3.1 Introduction

Efforts to minimize requirements for external controllers has led to the development of self-regulating microfluidic circuits, which contain embedded controls for autonomous execution of preprogrammed fluidic operations [1–5]. Such transition to self-regulated microfluidic devices are envisioned to facilitate transfer of technology from microfluidic device developers to biological end users [6]. An autonomous fluid circuit type that is of general usefulness in biology are microfluidic oscillators that convert two constant input flows into alternating fluid flows to allow periodic delivery of chemicals or to mimic the pulsatile nature of biological fluid flows such as blood flow [1]. A key requirement for biological studies in general is the ability to perform duplicate and triplicate experiments with the same conditions as well as to perform control experiments, such as exposing a system to the same pulsed flow conditions but with and without the presence of a stimulant chemical in the solutions. Because of circuit-to-circuit variability that lead to slightly different oscillation characteristics, it is currently difficult to perform such required multiplicate and control experiments with multiple independent autonomous fluidic oscillator circuits.

To minimize device-to-device variability between autonomous fluidic oscillators and to synchronize the frequency of the system, we explore coupled systems. First described by Huygens, in the classical case of periodic self-sustained oscillators, interactions or coupling between the individual systems leads to synchronized behaviors [7]. In this work we demonstrate

that two coupled microfluidic oscillators via a coupling capacitive unit, results in automatically synchronized oscillations. As paired nonlinear oscillators have been shown to produce different behavior depending on the coupling strength between the individual subunits [8], we investigated, the "strength" or impact of our coupling element. Consistent with theoretical understanding of synchronization, we observed that weak coupling results in synchronicity between similar frequency oscillators but non-coupled behavior and phase drift between oscillators with differing natural frequencies. Such non-coupling and phase drift could be overcome by increasing the capacitance in the coupling element. Theory states that overly strong coupling would quench each other, pulling each oscillator unit into a zero-amplitude standstill or "oscillation death" [9]. In our system, excessive capacitance is avoided by the shallowness of the capacitive unit where the flexible membrane, no matter how large, will be limited in their capacitive capability due to bumping into the chamber ceilings or floors. Thus, experimentally, we only observed oscillation death in very isolated conditions. This is convenient in allowing use of larger membrane coupling units to improve synchronization without significant worry of disrupting the oscillatory output. Simulations further show that the minimum coupling capacitance required is dependent on the internal capacitance of the microfluidic valve units used in the oscillators.

3.2 Materials and methods

Device Fabrication

Methods used for microfluidic oscillators and coupling capacitor master mold fabrication were similar to those previously presented [10]. The microfluidic oscillator device consists of three polydimethylsiloxane (PDMS) layers assembled as previously described. Briefly, the device features (66 μm height) were imprinted in the top and bottom layers, and a PDMS membrane

(target thickness: 11 μm) was positioned between them. 1:10 PDMS (Sylgard 184, Dow Corning, Midland, MI, USA) was poured onto the master mold and allowed to cure within a gravity convection oven at 60 °C for 6 h. The cured PDMS slab was then removed from the mold and cut into individual device layers. Concurrently, PDMS membranes were fabricated by spin-coating 1:10 PDMS onto glass slides pre-treated with silane as before. PDMS membranes were then cured within a gravity convection oven for 5 min at 120 °C and 10 min at 60 °C. Prior to final assembly, a 2-mm biopsy punch was used to remove PDMS from the inlet and outlet ports of the top device layer. The bottom layer and membrane were then treated by plasma oxidation (Covance MP, FemtoScience, Hwaseong-si, Gyeonggi-do, South Korea) to facilitate bonding and, following bonding, were then placed in a gravity convection oven at 120 °C for 5 min and at 60 °C for 10 min. Thru-holes were then made in the membrane to allow fluid communication between the top and bottom device layers, using a 350-μm biopsy punch (Ted Pella Inc., Redding, CA, USA). The top layer was then treated by plasma oxidation to facilitate bonding with the membrane-bottom layer assembly. Following treatment, but preceding bonding, the normally closed region of the top layer was "deactivated" by being brought into direct contact with an unoxidized PDMS "stamp". Following final bonding, assembled devices were incubated for 2 min within a gravity convection oven at 120 °C. Coupling capacitors were fabricated in the same fashion, except they did not require thru-holes to be punched within them, or have any region deactivated.

Coupling simulations

In the present study, commercial software (PLECS, Plexim GmbH, Switzerland) was used for the numerical simulation of the microfluidic oscillators and coupling capacitor. Based on electro-hydraulic circuit analogy, microfluidic channels are simulated as electric resistors, flexible

membranes correspond to capacitors, and the flow rates are transformed into electric current. The input flow rates and coupling capacitance were adjusted according to the settings of each experiment. All other parameters used in the model were from experimental measurements [11].

Microfluidic Oscillator Testing and Data Processing

Microfluidic oscillators were tested by connecting pressure sensors (Model 142PC05D, Honeywell, NJ, USA) at the device inlets via Tygon tubing (Saint-Gobain™ Tygon™ R-3603 Clear Laboratory Tubing, Saint-Gobain Performance Plastics, Akron, OH, USA) to measure source pressure. Source pressure data was collected for valves with quantify pressure buildup and release corresponding to fluid accumulation and evacuation, respectively, through the valves. The occurrence of fluidic oscillations and the coincident timing of these oscillations relative to source pressure profiles were initially verified visually, all subsequent quantification and assessment, however, was performed using source pressure data. Data was obtained at a sampling rate of 1000 Hz, every 100 data points were averaged (resulting in 1 data point per 100 ms), and stored using LabVIEW (National Instruments, Austin, TX, USA). Syringe pump (Model KDS220, KD Scientific, Holliston, MA, USA) was used to provide constant volumetric flow to the device. 3 mL syringes (Becton, Dickinson and Company, Franklin Lakes, NJ, USA) were connected to the inlet ports. Voltage data were collected using LabVIEW and processed to demonstrate oscillation frequency of the microfluidic oscillators tested.

3.3 Results and discussions

Two separate microfluidic oscillators, designed and fabricated with the same parameters when operated under the same infusion flow rate, e.g. 5 µL/min (Fig. 3-1a), are expected to execute equivalent operations. Yet, like any manufacturing process, inherent variability exists. Additional idiosyncrasies [10] arise due to the instabilities of syringe pump systems [12] and syringes [13].

Combined, these parameters lead to device-to-device variability as shown experimentally for two presumably "identical" oscillators operated under "identical" conditions by a pressure change over time plot (Fig. 3-1b) and a phase portrait (Fig. 3-1c).

In this work, we define microfluidic oscillator synchronization as the simultaneous switching by the valve units in each oscillator; where the opening and closing of the membrane valve is determined by the relative difference between the source minus gate pressure versus the threshold pressure [11]. Learning from electrical systems, we utilized various sizes of microfluidic capacitors (Table 1) [14], comprised of a flexible membrane that allows exchange of fluidic energy or pressure through it without passing of actual fluid (Fig. 3-2), to couple the two oscillators (Fig. 3-1d). With the incorporation of the microfluidic coupling capacitor we accomplished synchronized behavior with regards to pressure profiles between the two oscillators (Fig. 3-1f, g).

As a key component in the coupled oscillators, the microfluidic capacitor consists of three components: two layers of PDMS and one piece of PDMS membrane (Fig. 3-2a, b). Each PDMS layer has one chamber with the dimension of a mm × a mm × 60 μm. "a" is variable from 1.5 mm to 2.0 mm, 2.2 mm, 2.5 mm and 3.0 mm (Table 3-1).. The length and width of the chamber were used to define the capacitor size, in our presented work. The PDMS membrane has a thickness of 11 μm. It deforms when there is pressure difference between the upper chamber and lower chamber. Fluidic energy is transformed to elastic potential energy in the deformation.

The liquid on the higher pressure side applies force on the liquid on the lower pressure side, increasing the pressure on the lower pressure side. Thus, the microfluidic capacitor can balance the pressure difference without fluid passing though (Fig. 3-2b). The microfluidic coupling capacitor's fluidic capacitance can be derived by plate theory as

$$C = \frac{6w^6(1-v^2)}{\pi^4 * Eh^3} \quad (1)$$

where *w* is membrane width (*m*), *E* is Young's modulus of the membrane (N/m^2), *h* is membrane height (*m*) and *v* is Poisson's ratio of the membrane (dimensionless) [1].

To study how the microfluidic capacitor synchronizes the oscillators, we use air bubbles as an indicator to visualize the interaction between the two coupled oscillators. Air bubbles were injected into the tubing between the valve and the microfluidic capacitor (Fig. 3-2c). The tubing was marked with for quantitative measurement of air bubble movement (Fig. 3-2d). Source pressure of the coupled oscillators, as well as the location of the air bubbles were recorded at the same time. As seen in Fig. 3-2e, the two oscillators synchronize when using the microfluidic capacitor. The location of the air bubbles reveal the pressure difference at the two sides of the microfluidic capacitor (Fig. 3-2f). As a consequence, the air bubble moves with the liquid in the tubing, leading to the deformation of the PDMS membrane in the microfluidic capacitor. This equates to the fluid on the higher pressure side translating force to the lower pressure side, resulting in oscillator valves to open and close almost simultaneously. Fig. 3-2g is the distance between the two air bubbles. The distance is not constant, indicating the microfluidic capacitor is capable of restoring and releasing fluidic engery by deformation.

As the fluidic capacitance was increased, we found increased synchronization between the two coupled microfluidic oscillators (Fig. 3-3b, c). The measured oscillator valve pressures were implemented in eq 1, [15,16] to quantify the coupling strength afforded by different coupling capacitors.

$$\frac{d\varphi}{dt} = \Delta\omega + \varepsilon \sin\varphi, \quad (2)$$

Here ω is the natural frequency of the oscillator, ε is the coupling strength, and φ is phase difference of the two oscillators; for brief description and derivation of equation (2) for the analysis of phase synchronization for more in depth description see previous literature in oscillator locking and synchronization [15,16]. Using the empirical data, and assuming the equation goes to steady state ($\frac{d\varphi}{dt}$ = 0), we determine the maximum coupling strength reached within our system.

In addition to experimental studies, we performed simulations of the individual and coupled oscillators. We have previously showed that electrical circuit simulation software can effectively capture features of microfluidic oscillators. Here we simulate two "identical" oscillators exhibiting device-to-device variability as devices with differences in the phase of oscillation or with both differences in phase and frequency. We could identify a minimum critical capacitance needed for effective coupling, which was dependent on the magnitude of the parasitic capacitance of the valves within the oscillators (Fig. 3-4). Simulations predicted that out of phase oscillations could be synchronized with a critical coupling capacitance of 1 x 10^{-14} m^5/N (Fig. 4) but that oscillators that are both out of phase and with different frequencies from each other require a stronger coupling (e.g. 1×10^{-12}). Most importantly, we show through simulations the size range of coupling capacitance needed relative to the parasitic capacitance of the oscillator valves and inflow rates into the valves.

Table 3-1 shows experimental results of how larger capacitors result in increasing synchronization between oscillators. We characterized the behavior through both the pressure profiles of the valve units in each oscillator, as well as the phase portraits of these pressures. We found that by using smaller capacitors, such as the 1.5 mm x 1.5 mm capacitor, the oscillators become unstably synchronized (Fig. 3-3a). The coupled oscillators appear to have some

synchronicity, however, they shift in and out of this synchronized state, most likely indicating that the coupling strength of 0.0915 is insufficient to reach complete entrainment, but rather produces unstable synchronization. This is further reinforced when visualizing the phase portrait of P_1 vs. P_2, where a triangular pattern emerges, however this coordinated behavior seems to be unstable as the positioning of this pattern shifts through the entirety of the experimental data. Increasing the coupling capacitance, we see the stable synchronization between the oscillators (Fig. 3-3b, c), where the phase portrait of P_1 vs. P_2 shows a consistent triangular pattern with increasingly fixed positions with increasing coupling capacitance. The coupling strength for the larger microfluidic capacitors, 8.073 and 43.15, concomitantly increases with synchronized behavior of the oscillators.

The microfluidic capacitor is capable of coupling the oscillators while preventing the liquid from passing through it, however, the presence of the elastic PDMS membrane may limit the extent of the force translated from one oscillator to the other. Implementing a direct connection may be experimentally unideal for cell based experiments, as the mixing of solutions may compromise experimental conditions when utilizing differing media compositions and biomolecule stimulants; however, considering the dynamics of our system, we identified that this would result in the strongest coupling behavior (Fig. 3-3d). Direct coupling of the oscillators with tubing results in the source pressure waveforms being tightly synchronized, overlapping more so than that seen with microfluidic capacitor coupling, reaching a maximum coupling strength of 45.307. Additionally, the phase portrait of P_1 vs. P_2 shows a diagonal pattern, indicating a high degree of entrainment between the two oscillators. Coupling also appeared to result in frequency stabilization, generally demonstrating a reduction in period variation with increasing coupling strength (Fig. 3-5).

In addition to oscillators that have even duty cycles (50% - 50% in terms of time valve open for each of the two valves of an oscillator) we analyzed synchronization between oscillators operated with asymmetric input flowrates that give asymmetric duty cycles[10]. Figure 3-6 shows experiments using oscillators with asymmetric input flow rate combinations of: 1) 5 µL/min flow rates into the coupled valve units via syringes B and D, and 2.6 µL/min into the non-coupled valve units via syringe A and C; 2) 2.6 µL/min flow rates into the coupled valve units via syringes B and D, and 5 µL/min into the non-coupled valve units via syringe A and C; 3) non-paired input flow rates, with 5 µL/min input via syringes A and D, and 2.6 µL/min input via syringes B and C. When using combination 1 we achieved synchronization in all coupling conditions except when using the smallest microfluidic coupling capacitor, whereas the other two asymmetric input flowrate combinations only resulted in synchronized behavior when the oscillators were directly connected. We expect the inability to synchronize the oscillators in condition 2 and 3, is the insufficient energy translated via the fluidic capacitor.

In biological experiments more than two microfluidic oscillators may be required to function in parallel, under the same oscillatory behavior. For example, in the study of cellular signal pathway architecture, parallel experiments might require oscillators outputting oscillatory flow with the same frequencies, but different concentrations. Figure 3-7a demonstrates the ability to scale oscillator coupling from two to four oscillators. The four oscillators are coupled by three capacitors with 3.0 mm chambers. All four oscillators have a constant input flow rate of 5 µL/min. The pressure profiles of the oscillators demonstrate robust entrainment (Fig. 3-7b). These results demonstrate that the coupling phenomena, can be implemented when an array of synchronized oscillators are needed, as long as the coupling strength meets the minimum requirement for the system.

3.4 Conclusions

In this work we demonstrate that multiple microfluidic oscillators can be coupled via fluidic capacitors to automatically synchronize their oscillations. Simulations identified a relationship between the internal capacitance of the microfluidic valve units and the coupling capacitors capacitance, such that a minimal critical capacitance needs to be used to generate sufficient coupling strength to synchronize the two oscillators. Microfluidic oscillators with asymmetric inflow pairings can also be synchronized, provided the oscillators are coupled through the valves receiving the larger inflows.

3.5 References

[1] Mosadegh B, Kuo C-H, Tung Y-C, Torisawa Y, Bersano-Begey T, Tavana H, et al. Integrated elastomeric components for autonomous regulation of sequential and oscillatory flow switching in microfluidic devices. Nat Phys 2010;6:433–7. doi:10.1038/nphys1637.

[2] Duncan PN, Nguyen TV, Hui EE. Pneumatic oscillator circuits for timing and control of integrated microfluidics. Proc Natl Acad Sci 2013;110:18104–9. doi:10.1073/pnas.1310254110.

[3] Leslie DC, Easley CJ, Seker E, Karlinsey JM, Utz M, Begley MR, et al. Frequency-specific flow control in microfluidic circuits with passive elastomeric features. Nat Phys 2009;5:231–5. doi:10.1038/nphys1196.

[4] Toepke MW, Abhyankar VV, Beebe DJ. Microfluidic logic gates and timers. Lab Chip 2007;7:1449–53. doi:10.1039/B708764K.

[5] Collino RR, Reilly-Shapiro N, Foresman B, Xu K, Utz M, Landers JP, et al. Flow switching in microfluidic networks using passive features and frequency tuning. Lab Chip 2013;13:3668–74. doi:10.1039/C3LC50481F.

[6] Rhee M, Burns MA. Microfluidic assembly blocks. Lab Chip 2008;8:1365–73. doi:10.1039/B805137B.

[7] Rosenblum MG, Pikovsky AS, Kurths J. Phase Synchronization of Chaotic Oscillators. Phys Rev Lett 1996;76:1804–7. doi:10.1103/PhysRevLett.76.1804.

[8] Ozden I, Venkataramani S, Long MA, Connors BW, Nurmikko AV. Strong Coupling of Nonlinear Electronic and Biological Oscillators: Reaching the ``Amplitude Death'' Regime. Phys Rev Lett 2004;93:158102. doi:10.1103/PhysRevLett.93.158102.

[9] Author AP, Rosenblum M, Kurths J, Hilborn RC. Synchronization: A Universal Concept in Nonlinear Science. Am J Phys 2002;70:655–655. doi:10.1119/1.1475332.

[10] Lesher-Perez SC, Weerappuli P, Kim S-J, Zhang C, Takayama S. Predictable Duty Cycle Modulation through Coupled Pairing of Syringes with Microfluidic Oscillators. Micromachines 2014;5:1254–69. doi:10.3390/mi5041254.

[11] Kim S-J, Yokokawa R, Takayama S. Analyzing threshold pressure limitations in microfluidic transistors for self-regulated microfluidic circuits. Appl Phys Lett 2012;101. doi:10.1063/1.4769985.

[12] Li Z, Mak SY, Sauret A, Shum HC. Syringe-pump-induced fluctuation in all-aqueous microfluidic system implications for flow rate accuracy. Lab Chip 2014;14:744–9. doi:10.1039/C3LC51176F.

[13] Neff SB, Neff TA, Gerber S, Weiss MM. Flow rate, syringe size and architecture are critical to start-up performance of syringe pumps. Eur J Anaesthesiol 2007;24:602–8. doi:10.1017/S0265021506002328.

[14] Kim S-J, Yokokawa R, Takayama S. Microfluidic oscillators with widely tunable periods. Lab Chip 2013;13:1644–8. doi:10.1039/C3LC41415A.

[15] Pikovsky A, Rosenblum M, Kurths J. Phase synchronization in regular and chaotic systems. Int J Bifurc Chaos 2000;10:2291–305. doi:10.1142/S0218127400001481.

[16] Adler R. A Study of Locking Phenomena in Oscillators. Proc IRE 1946;34:351–7. doi:10.1109/JRPROC.1946.229930.

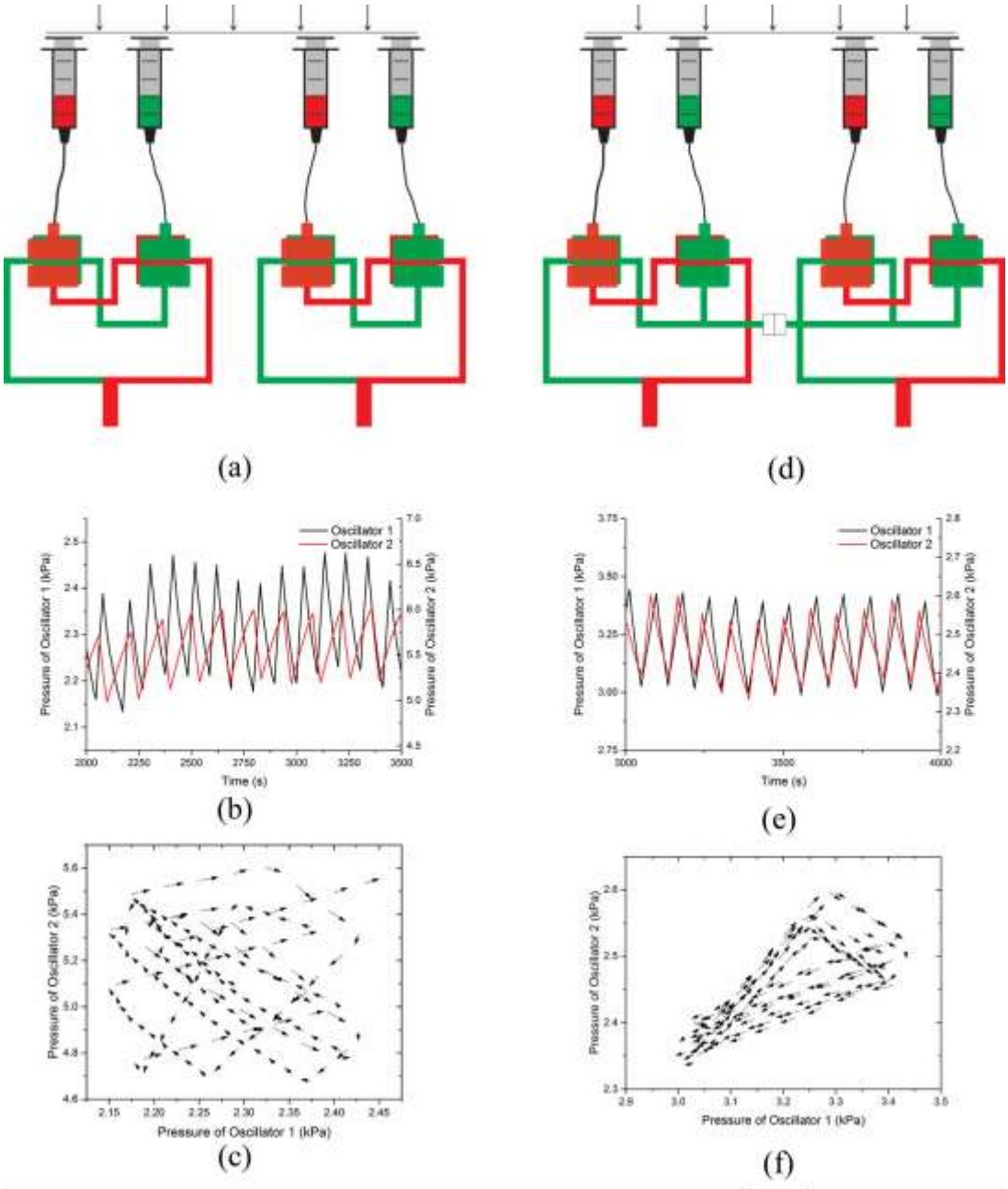

Figure 3-1: Coupled microfluidic oscillators results in synchronous behavior.
(a) Schematic of two separate oscillators intended for parallel experiment. (b) Experimentally measured source pressure changes of the two separate oscillators over time (The valves connected to the syringe with red liquid are measured). (c) Oscillator pressure phase portrait of experimentally observed pressure profiles between oscillator 1 vs. oscillator 2 when the oscillators are not coupled. (d) Schematic of two oscillators coupled by a microfluidic capacitor. (e) Experimentally measured source pressure changes of the two coupled oscillators over time. (f) Oscillator pressure phase portrait of experimentally observed pressure profiles between oscillator 1 vs. oscillator 2 when the oscillators are coupled. All the oscillators in the experiment have a constant input flow rate of 5 µL/min from syringe pump.

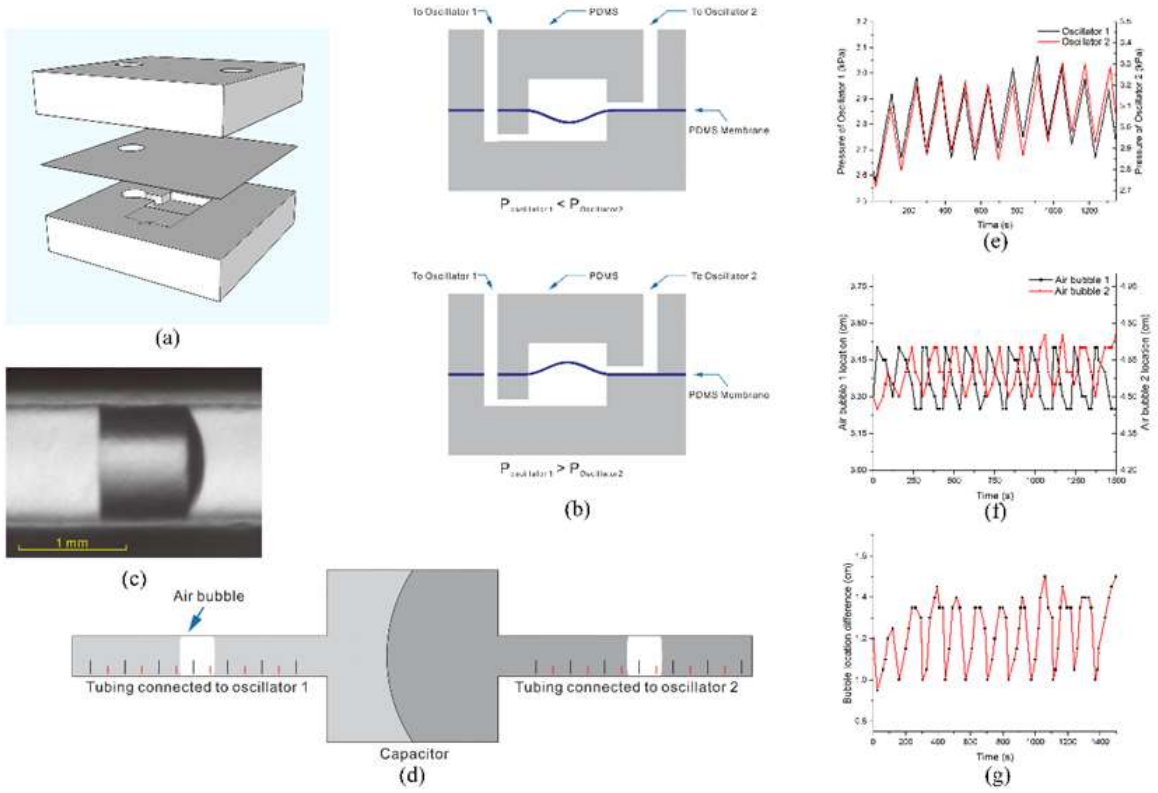

Figure 3-2:Structure and characteristic response of the microfluidic capacitor.
(a) Three dimensional view of the microfluidic capacitor. The microfluidic capacitor consists of two layers of PDMS and one PDMS membrane in the middle. (b) Cross-sectional views of the capacitor. The bottom chamber is connected to the oscillator 1 and the top chamber is connected to the oscillator 2. The PDMS membrane deforms when there is pressure difference between the two chambers. (c), (d) Air bubble is injected into the tubing as an indicator to reveal the interaction between the two oscillators. The tubing connected to the capacitor is marked with ruler to measure quantitatively the movement of the air bubbles. (e) The source pressure of the two oscillators. (f) The location of the air bubbles. (g) The location difference of the air bubbles. (e), (f) and (g) were recorded at the same time.

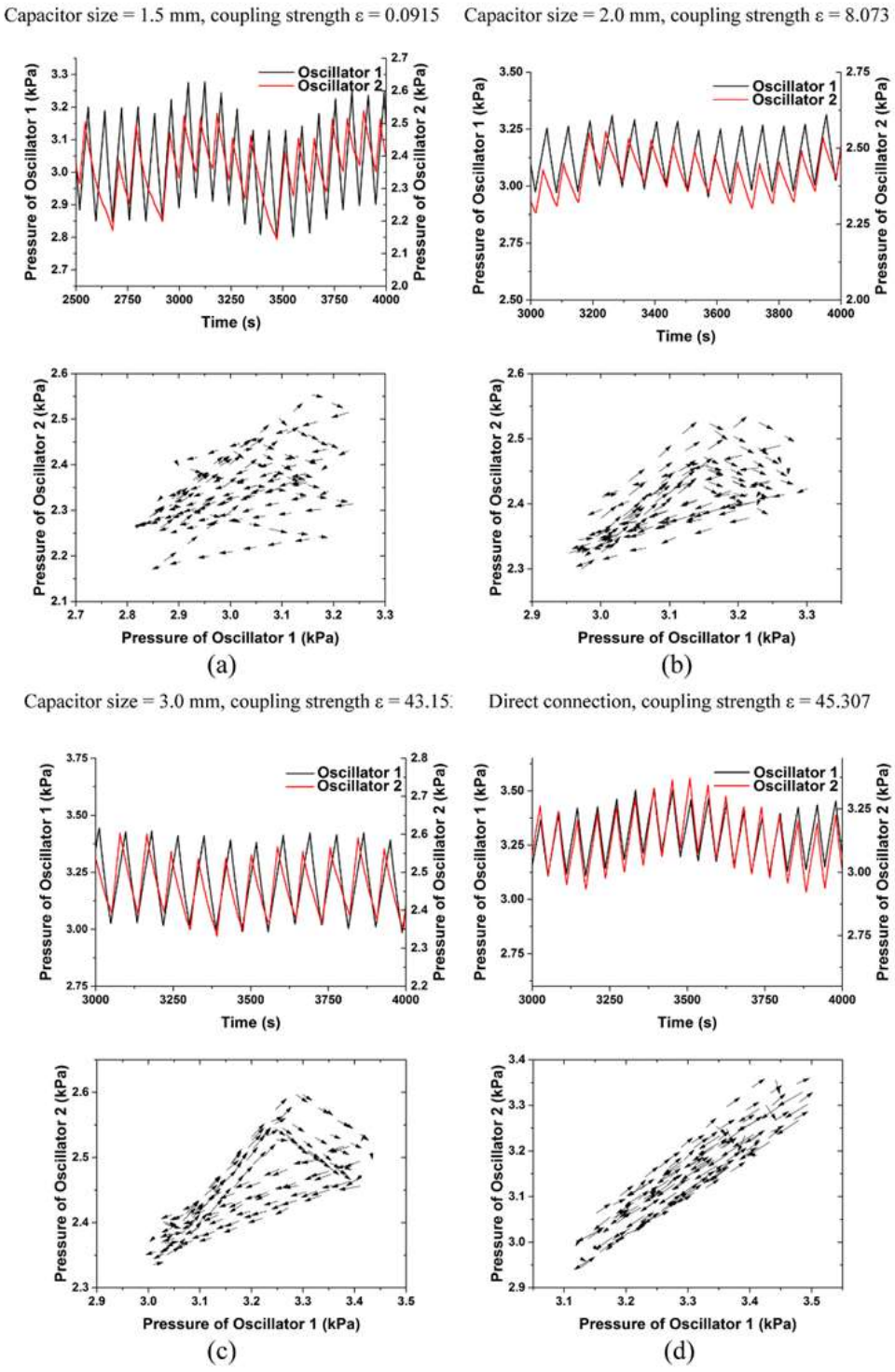

Figure 3-3: Increasing oscillator entrainment with increasing coupling strength.
Source pressure profiles of oscillator 1 and 2 along with the associated coupling strength. Phase portrait, P1 vs. P2, presented under oscillator pressure profiles. (a) Separate oscillators. (b) Capacitor size = $(1.5\ \text{mm})^2$. (c) Capacitor size = $(2.5\ \text{mm})^2$. (d) Direct connection.

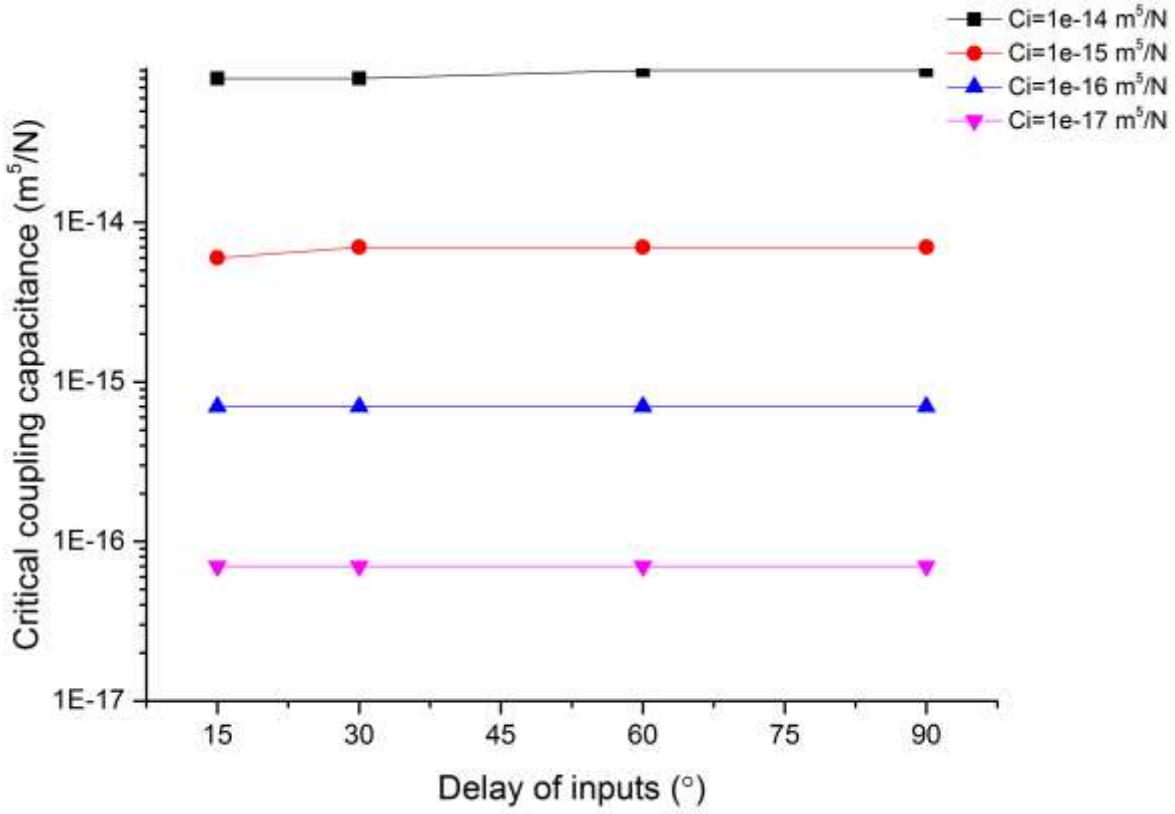

Figure 3-4: Critical coupling capacitance dependent on internal microfluidic oscillator valve capacitance.

PLECS simulations of two out of phase, equivalent oscillators with identical frequencies coupled to identify minimal, or critical, coupling capacitance to induce synchronization of oscillators. Simulations of the coupled microfluidic oscillators, demonstrated that the critical coupling capacitance is dependent on the capacitance of the transistor-like valves in the microfluidic oscillator.

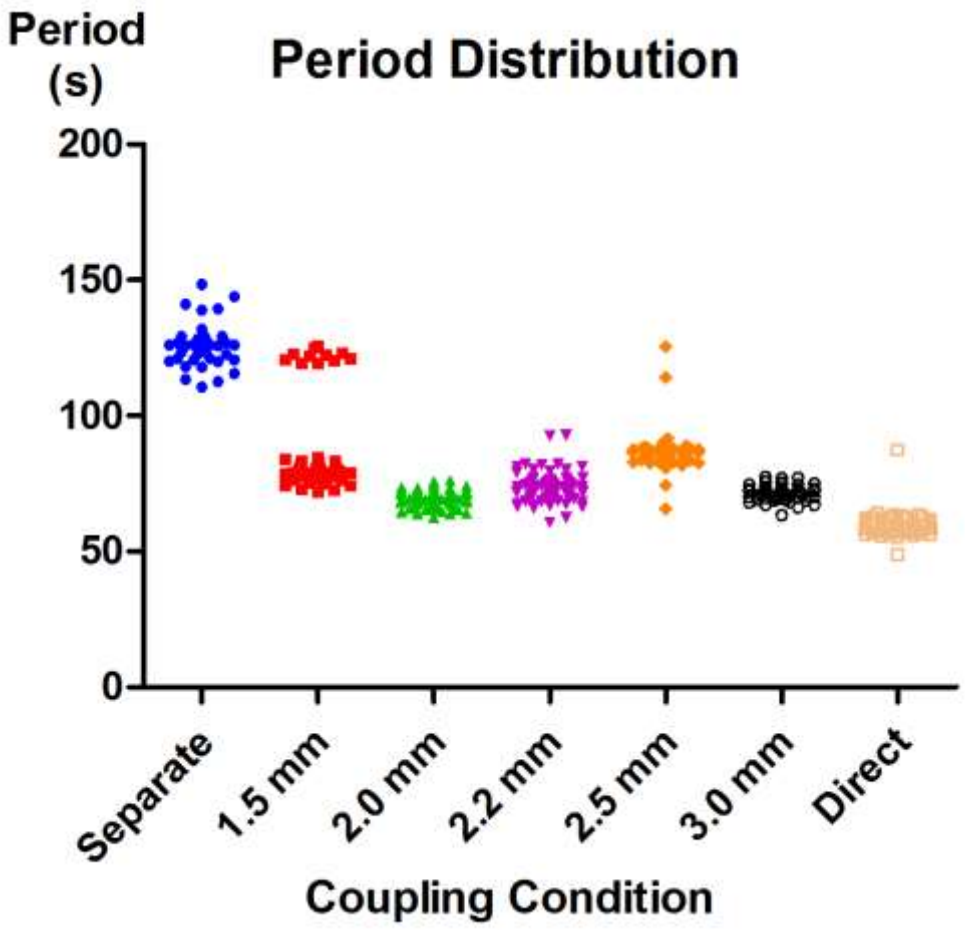

Figure 3-5: Period Stabilization with increased coupling strength.
Period fluctuation over time was plotted for different coupling capacitor sizes demonstrating a stabilization effect when coupling the oscillators. An increase in stability and reproducibility of the same oscillation period, predominantly occurred with increasing coupling strength.

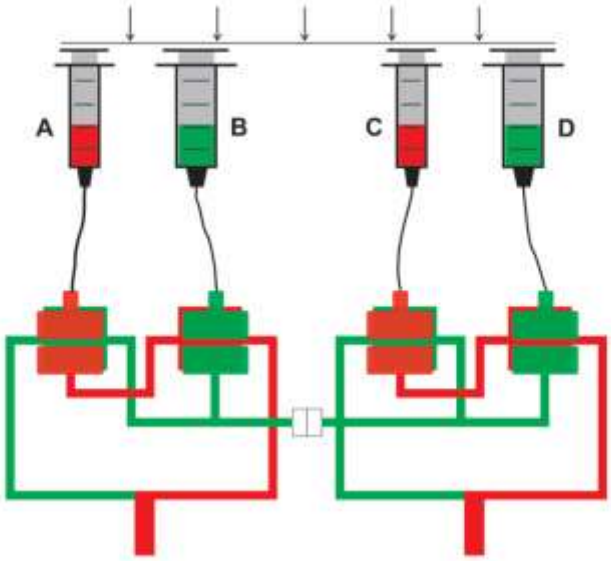

(a)

ε	a=c=2.6 mL/min b=d=5 mL/min	a=c=5 mL/min b=d=2.6 mL/min	a=d=2.6 mL/min b=c=5 mL/min
1.5 mm	0.004	0.050	0.036
2.0 mm	0.274	0.045	0.033
2.2 mm	0.581	0.077	0.033
2.5 mm	0.682	0.062	0.030
3.0 mm	2.672	0.085	0.029
Direct connection	5.409	10.462	11.337

* Synchronized
Non-synchronized

(b)

Figure 3-6: Asymmetric oscillator with adjustable duty cycles and their coupling strength under different conditions.
(a) Asymmetric inflow via differential syringe size into coupled oscillators. (b) Coupling strength for different combinations of input flow rates.

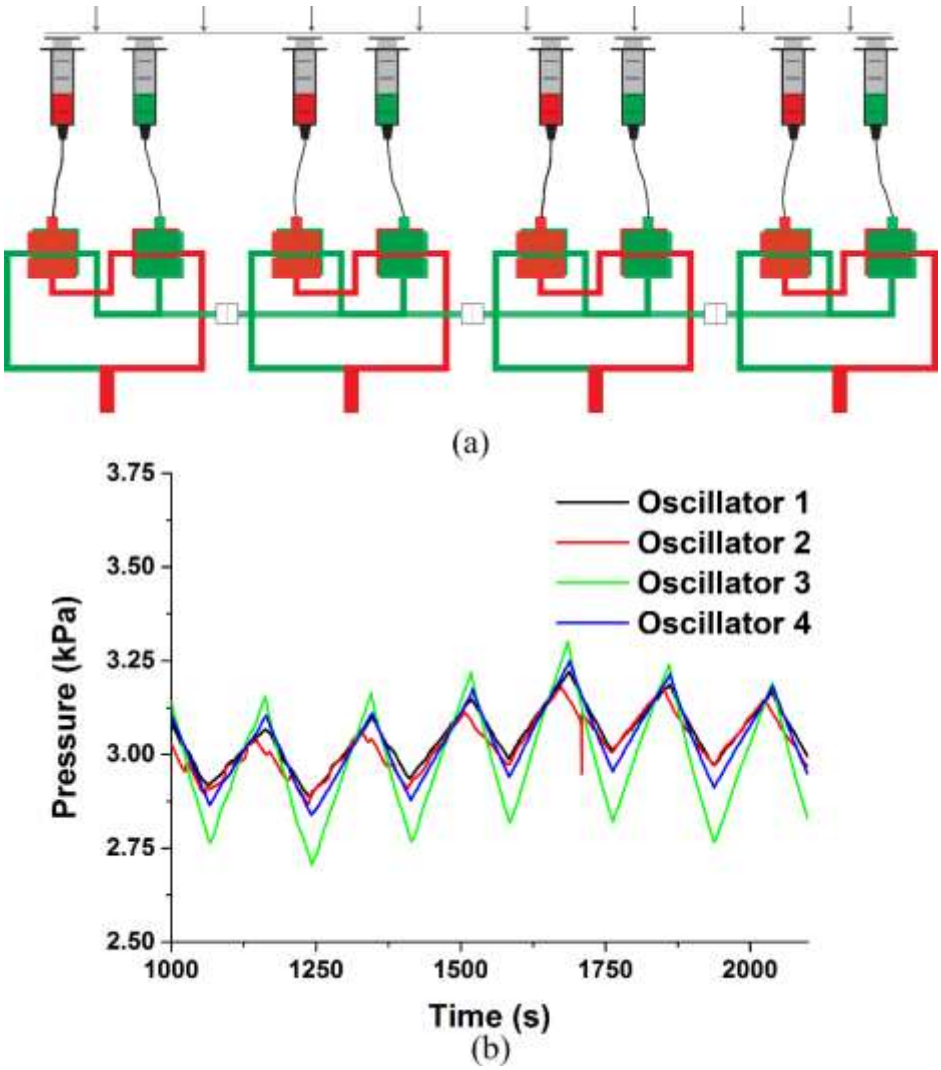

Figure 3-7: Synchronization of more than two oscillators coupled by microfluidic capacitors. (a) Four oscillators coupled by three microfluidic capacitors. Each oscillator has a constant input flow rate of 5 µL/min. The microfluidic capacitor size is 3.0 mm. (b) Source pressure of the four oscillators over time. Pressure sensors are connected to the syringes with red liquid as shown in Fig. 4a.

Chamber length/width (mm)	Capacitance (m^5/N)
1.5	1×10^{-12}
2.0	1×10^{-11}
2.2	1×10^{-10}
2.5	1×10^{-9}
3.0	1×10^{-8}

Table 3-1: Capacitor size and its corresponding capacitance

Chapter 4: Media additives to promote spheroid circularity and compactness in hanging drop platform

4.1 Introduction

Conventional methods for high throughput screening have primarily utilized two-dimensional cell cultures in well plates. Recently, the trend has been shifting towards three-dimensional (3-D) drug screening, especially in cancer therapeutics, due to the unique characteristics of these culture platforms. These cell aggregates allow for increased cell-cell interactions such as adhesion and junctional connections, reduced proliferation rates more aligned with physiological growth rates, restricted and non-linear diffusion gradients resulting in non-uniform metabolic gradients [1]. Additionally, 3-D culturing is desirable as some cells have shown to lose their physiologic phenotypes and functions when cultured in two dimensional culture platforms, however, these phenotypes can be retrieved by culturing cells in 3-D emulating conditions [2]. Spheroid culture has also been applied to creating complex co-culture systems [3]. Multicellular spheroids represent an attractive platform because it provides a model of oxygen, metabolite, nutrient, and drug gradients observed in tumors due to non-uniform vascular perfusion in a radially symmetric architecture that is easier to reproduce and mathematically model.

Multicellular spheroid models have been generated through various methods, and reviewed thoroughly in recent literature [4, 5]. One of the common methods described is the 'hanging drop' technique, in which cells are placed in a suspended drop of media and as a result of gravity and the meniscus incurred by the air-liquid interface, cells localize at the bottom of the hanging drop, typically resulting in intercellular aggregation and adherence. This method of generating

spheroids has been applied to fabricate 3-D tissues such as embryoid bodies, cancer tumor models, microlivers, microhearts, microcartilage [6-9]. Spheroid culture in hanging drops has garnered popularity as a high throughput tool supported by published systems and methods for more standardized, robust generation and maintenance of hanging drop cultures [6, 10, 11]. A major advantage of this system also extends from the ability to culture and image spheroids directly from the hanging drops over extended periods of time (weeks to months)[11], whereas, in 2-D cultures, cells grown on the culture surface eventually form a confluent monolayer and begin to slough off the surface as a sheet or clump.

Requirements we believe critical to 3-D spheroid screening models are 1) tightly aggregated spheroids to facilitate physiologically relevant cell density, 2) the formation of diffusion gradients, and 3) tuneable and reproducible spheroid size based on initial seeding density. However, not all cell types have demonstrated spontaneous aggregation in spheroid cultures, resulting in loose aggregates, or disconnected, floating cells [12]. This phenomenon poses a barrier in testing different cell types, which may only be able to establish weak intercellular interactions, if any, resulting in an inability to form spheroids. In order to overcome this inability to coalesce, researchers have applied different methods to induce cellular aggregation in cells of interest [4, 5]. One such method is the inclusion of additives to 3-D cultures for improved spheroid formation. Both biological and synthetic additives have been successfully employed, with mechanisms varying between cross-linking agents [13, 14], adhesion stimulation [15], or rheological modifiers and crowding agents [16]. Supplementation of cross-linking agents has generally been done with extracellular matrix proteins, such as collagen, fibronectin and reconstituted basement membrane matrigel [12, 17]. Additional methods of using cross-linkers to improve spheroidal aggregation include the use of polymer nanospheres [13] or chemically

modifying cell surfaces via biotinylation and culturing in the presence of supplemented avidin [14]. Similar to using cross-linking agents, spheroid formation has also been accomplished by using β1-integrin-stimulating monoclonal antibodies [15]. Unlike supplements that directly tether or act as a tether to cells, certain additives have improved the formation of spheroids through rheological modification or as a crowding agent. Methylcellulose (MethoCel) has been applied to spheroid formation and even though the mode of action has not been conclusively determined, it has been attributed to MethoCel's inert semi-solid gel like properties, or viscosity, or additionally crowding effect induced by the molecule [16, 18, 19]. The addition of MethoCel to hanging drop cultures has been solely applied [18] or co-supplemented with cross-linking additives, such as matrigel [17]; these modifications have shown improvement in cellular aggregation and formation of 3-D structures. Additionally, supplemented cultures demonstrated increased reliability and robustness for spheroid formation; however concentrations of supplemented MethoCel have not been characterized.

In this study we aim to compare the individual and combined effects of two widely used additives (collagen and MethoCel) in hanging drop cultures to promote the circularity and compactness of 3-D spheroids for a variety of cell types. To focus exclusively on the impact of additives of spheroids within the context of high throughput screening, we used previously reported high throughput hanging drop array plates [6] coupled with a liquid handling robot to minimize sample variability, provide robust culturing conditions with minimal to no spreading, loss of shape, or rupturing of hanging drops as compared to the more commonly known inverted lid methodology[6]. Using finite element models we first demonstrate the importance of these two morphologic parameters in the establishment of radial transport gradients, a hallmark feature of spheroid models. We then compare the effects of different macromolecule thickening agents

in hanging drop cultures. Even though increasing viscosity results in a reduction of spheroid motion while imaging, we identify that modulating viscosity is not the sole requirement to induce spheroid formation, indicating the need to consider other molecular characteristics when selecting additives to promote spheroid morphology.

4.2 Results and discussion

Effects of spheroid geometry and physical characteristics on diffusion gradient

Diffusion kinetics is a major factor that influences cellular responses in 3-D spheroids. Nutrients and waste byproducts face diffusion resistance as they enter or leave a spheroid, respectively. Additional compounds in the surrounding medium will similarly develop gradients as they penetrate the spheroid. The rate of diffusion and steepness of the diffusion gradient are primarily influenced by the circularity and compactness of a spheroid. Circularity refers to the symmetry of a spheroid, with an ideal equidistant symmetry from the center of the spheroid to any point on the surface. This ideal symmetry would result in a concentric diffusion gradient field; facilitating robust modeling of molecular diffusion into the spheroid. In contrast, elliptical 3-D cellular masses would result in an increase of surface area and a reduction of average distance from the long axis to the spheroid's center of mass. As expected this was confirmed using a finite element model to compare oxygen diffusion into an ideal spheroid versus an ellipsoid of the same volume. Using oxygen diffusion coefficients[20] and consumption rates[21, 22] from the literature, the model predicted the presence of a hypoxic region in an ideal spheroid, whereas this region is absent in an ellipsoid of the same volume with a 2:1 deformed aspect ratio (Fig. 4-1a). This simulation shows that spheroid geometry has a direct effect on the physical characteristics of transport gradients.

Using the same approach we also estimated the effect of compactness on spheroid transport properties. Compactness refers to the degree of remodeling and density of a spheroid. As cells come into contact with each other, from the initial step of aggregation through spheroid formation, they can manipulate and secrete ECM proteins leading to reorganization and compaction. Here we simulate the effect of compaction by modeling the steady-state concentration of oxygen in two spheroids with an identical number of cells, and hence identical overall oxygen consumption rate. The first is a reference spheroid with uniform oxygen consumption rate, compared to a compact spheroid half the diameter (1/8 the volume). In other words, the compact spheroid would have a specific volumetric oxygen consumption rate that is eight times higher than the reference spheroid to account for the loss of volume. Assuming similar oxygen diffusion kinetics for both spheroids, the model predicted a steep hypoxic gradient from the surface to the core of the compact spheroid compared to the reference spheroid (Fig. 4-1b). These simulations indicate that the uniformity, strength and steepness of a solute gradient within a spheroid are directly proportional to the circularity and compactness, or morphology, of a spheroid. The simulations support the notion that spheroid responses to small molecules can be impacted significantly by spheroid morphology. Therefore any meaningful comparisons between pharmacokinetics of different drugs must be conducted using spheroid models with similar, reproducible physical characteristics.

Effect of additives on spheroid morphology in hanging drop cultures

Additives in hanging drops can affect the speed, quality, longevity and robustness of spheroid formation. Many of the advantages of spheroid culture, including transport limitation and establishment of a nutrient gradient, are based on the assumption that cells form a compact and symmetrical spheroid mass. Here, we assessed MethoCel, an additive that does not adhere to

cells, in its ability to enhance spheroid formation. Unlike ECM proteins additives, such as collagen or fibronectin, MethoCel does not bias toward cell aggregation by acting as a scaffolding protein that binds multiple cells through surface receptors. However, given the widespread use of collagen as an aggregating/crosslinking agent in 3-D culture, we included it to serve as a comparison to MethoCell as well as assess the combined effects of collagen and MethoCel on spheroid formation using several cell lines.

One challenge in assessing spheroid morphology is to determine a standardized metric that correlates with spheroid function. As demonstrated with finite element models, circularity and compactness have a significant impact on transport gradients within spheroids. To this end, we developed a visual comparison-based, 5-point scale to assess circularity and compactness of spheroids. The uneven brightness of spheroid and background caused by the curvature of hanging drop complicates the determination of the spheroid border necessary for computer image analysis. Circularity and compactness of each spheroid were scored by comparing phase-contrasted micrographs to the 5-stages of development for each metrics (Fig. 4-6 and 4-7). The scores were generated blinded and independently by two researchers and the averages are presented as a gradient map (Fig. 4-2).

We tested several tumor cell lines since these would be of most interest to drug screening applications. In agreement with previously observed results, spheroids generally become more circular and compact when supplemented with low concentration of collagen compared to unsupplemented control conditions [12]. Whereas high collagen concentrations had varied responses, primarily a negative impact on spheroid circularity and compactness and in some cell types (A549 and HeLa) completely abrogating single spheroid formation, similar to previously reported formation of small multi-spheroids within cultures containing higher concentrations of

matrigel [17]). In contrast, cells behave in a much more uniform fashion in the presence of MethoCel. For most cells tested (DU145, A549, HeLa, MDA-MB-231, MCF-7), the presence of MethoCel improved circularity and compactness of spheroids in a dose dependent manner with varying degrees of effectiveness. The exceptions were HEK293 cells, where circularity and compactness scores were high and favorable regardless of MethoCel addition, and PC3 cells, where MethoCel conferred almost no improvement. In MethoCel only culture, further addition of MethoCel combined with low concentration of collagen did not enhance spheroid morphology in a dose dependent manner, but instead caused no change or negatively impacted spheroid morphology. Finally, high collagen concentration combined with MethoCel lead to mixed results with no discernible trends.

Like in most tissue constructs, cells remodel and reshape the spheroid over time. MethoCel demonstrated its ability in enhancing spheroid morphology in the acute phase of spheroid culture (2 days), but it was unclear whether such enhancement would be sustained over a long culture period. To test this we chose three tumor cell lines (MDA-MB-231, DU145 and PC3) to further examine the effects of MethoCel on monoculture spheroid formation over a period of 4 days. Spheroids consisting of either MDA-MB-231 or DU145 became more circular and compact from day 1 to 4 post seeding (Fig. 4-3). The addition of 0.24 mg/mL of MethoCel led to further enhancement over time when compared to cultures with no additives. Interestingly, PC3 spheroid morphology was minimally affected by culture time and presence of MethoCel. This finding suggests that the effectiveness of MethoCel may be cell-type dependent.

Spheroid formation generally improved using collagen concentrations within the range previously described in the literature [12, 15, 23]. At higher concentrations, collagen led to formation of multiple spheroids instead of a single one as expected, reflecting previously

reported results in increased matrigel concentrations[17] and in some cases, we observed significant adhesion to the hanging drop plate and formation of an elongated cell mass. The latter may be caused by non-specific absorption of protein, including collagen, onto the hanging drop plate that leads to subsequent cell adhesion and nucleation around the rim of the plate.

The final spheroid size in a hanging drop platform can be controlled by varying the initial cell seeding number in each droplet. The assumption is that higher initial cell numbers in a droplet will result in a larger spheroid, and this generally seems to hold true for different cell types [10] and additive concentrations we have tested (data not shown). However, at high collagen concentration, cells may form clusters to create multiple nucleation sites as they are settling, which in turn increases the likelihood of multi-spheroid formation [17]. Another aspect to consider is that some cell types have a natural tendency to form clusters of certain size irrespective of seeding density, especially in high ECM concentrations. This is seen in mammary epithelial cells, which form hollow acini with uniform size when seeded in Matrigel irrespective to cell quantity [24]. These factors should be considered if the goal is to generate single spheroid within each hanging drop.

Viscosity mediated spheroid stability for improved imaging and analysis in hanging drop culture

Among the many techniques to assess anti-tumor drug efficacy, microscopic imaging remains a commonly used modality due to its simplicity and compatibility with online, automated high throughput screening. However, the motion blur associated with the vibration of the microscope or sample movement within the hanging drop can limit the quality of images, especially for long exposures necessary in fluorescence imaging. The free-floating nature of spheroids within the hanging drop culture results in the lack of steadfastness or spheroid stability, resulting in motion blur artifacts which can limit the ability to automate imaging of these high throughput spheroid arrays. We went on to confirm that MethoCel additionally reduces motion artifacts during

microscopy of spheroids in hanging drops. By tracking spheroid movement and analyzing the center-of-mass path length we observed that as little as 0.024 mg/mL of MethoCel in medium is sufficient to reduce motion artifact in small or larger (25 and 500 cells, respectively) spheroids. In larger spheroids (500 cells), motion artifacts appeared to be slightly reduced as compared to smaller spheroids in the absence of MethoCel; however the stabilizing effect of MethoCel markedly reduced motion artifact in spheroids of both sizes tested (Fig. 4-4a). This secondary effect of MethoCel is particularly beneficial as it will improve the robustness to observe and image spheroids within the hanging drop culture. This is a significant finding as many of the clinically relevant hanging drop spheroid applications involve long-term culture of small (10 to 50 cells), patient-derived cell population in spheroid formats, which could benefit from a method to both improve spheroid formation and facilitate imaging of samples while not disrupting the longevity of culturing. Addition of MethoCel also did not change droplet contact angle (Fig. 4-4b) or evaporation rate (Fig. 4-4d) as compared to the control culture media, indicating that the motion dampening and subsequent spheroid stability was most likely conferred by viscosity as opposed to changes in Marangoni or thermo-convective flow profiles.

It is not surprising that the increase in viscosity imparted by the presence of MethoCel would dampen external vibration and reduce the amount of forces transmitted to the spheroid for improved stability. Due to MethoCel's viscosity mediated stabilization, and multiple descriptions eluding that its' semi-solid, inert viscosity modulating properties maybe responsible for spheroid formation, we assessed other long chain macromolecules in their ability to achieve similar levels of spheroid stabilization, as well as their ability to promote spheroid formation. In fact we found other long chain macromolecules, including dextran (DEX), Ficoll and polyethylene glycol (PEG), supplemented to match 0.024% MethoCel viscosity (Fig. 4-4e) achieved similar level of

motion artifact reduction for spheroid imaging (Fig. 4-4c) and slightly reduced evaporation rates (Fig. 4-4c).

Regardless of comparable viscosity, we identified that of the additives tested, MethoCel resulted in the most improved spheroid circularity and compactness in poor-spheroid forming cells, such as MDA-MB-231. Conversely, these macromolecule additives may interfere with spheroid formation, in a cell-type dependent manner, as noted when they are present in HEK293 spheroid culture. Specifically, even though all HEK293 cultures resulted in the formation of spheroids regardless of additives, each hanging drop culture with either PEG or DEX supplements resulted in the formation of multiple spheroids (Fig. 4-5). As previously discussed, multi-spheroids in a single droplet are non-ideal for screening applications, further indicating that regardless of viscosity modification there are secondary macromolecule effects necessary for robust promotion of spheroids in hanging drop cultures. Such factors may be crowding or "swelling" effects which could produce localization of ECM proteins [25, 26] or the aggregation of cells [27] within the hanging drop cultures. These phenomena have been demonstrated to result in mechanisms that should induce particle and cellular aggregation when using certain macromolecules as additives [27], one such macromolecule being MethoCel.

4.3 Experimental procedures

Cell culture

Cells were cultured at 37 °C at5% CO_2 using a culture medium composed of Dulbecco's Modified Eagle's Medium (DMEM) (Invitrogen) supplemented with 10% Fetal Bovine Serum (FBS) and 1% antibiotic-antimycotic. Cells were cultured in 100mm culture dishes until reaching ~ 80% confluence and were then passaged using 0.25% Trypsin/EDTA (Gibco) to detach cells from plates prior to diluting and transferring them to the hanging drop plates. All cell lines were

obtained from ATCC. Cell lines cultured for spheroid formation were human embryonic kidney HEK 293 (ATCC CRL-1573), breast cancer MDA-MB 231 (ATCC CRM-HTB-26) and MCF7 (ATCC HTB-22), lung cancer A549 (ATCC CCL-185), cervical cancer cells HeLa (ATCC CCL-2), prostate cancer PC3 (ATCC CRL-1435) and DU145 (ATCC HTB-81).

Spheroid Culturing and Assessment for Methyl Cellulose and Collagen Type I

Prior to usage, a hydrophilic coating (0.1%, Pluronic F108, BASF Co., Ludwigshafen, Germany) is applied onto the entire hanging drop plate surface. The plate is subsequently UV sterilized before cell seeding. To form hanging drops, cell suspension solution is pipetted from the top side through the access holes with the end of each pipette tip inserted into the access hole to guide the sample liquid to the bottom surface. Spheroid formation was tested for the different cell types across multiple concentrations of A4M MethoCel (Dow Chemical, MI) and bovine type I collagen (Corning, NY). The following concentrations for collagen 0, 0.3%, 1.5% were paired with the following concentrations of MethoCel 0, 2, 10, 20% of stock MethoCel (1.2% w/v). These different conditions were assessed to determine spheroid formation as a result of the additives in the media. These combinations were assessed and used to generate a gradient map of increased spheroid formation. Samples were assessed and compared to the spheroid formation scale seen in Figure 4-6 and 4-7.

Spheroid morphology scoring

Brightfield images of spheroids were collected at 10x magnification and assigned scores based on circularity and compactness. These images were randomized and scored by blinded observers. Observers were given a series of images describing the criteria for each metrics and were asked to score each image out of a 5-point scale. These scores were averaged and tabulated with

gradient scale to allow visual comparison of the effects of medium additives across different cell lines.

Viscosity measurement of medium with additives

Solutions were prepared for viscosity testing using culture media composed of DMEM (LifeTechnologies, Carlsbad, CA) with 10% FBS and 1% antibiotic-antimycotic (Life Technologies, Carlsbad, CA) with the addition of the different additives. Viscosity testing was done on a total of five solution types, culture media as well as the four solutions with additives. Additives were placed into the culture media to match the viscosity of MethoCel 0.024% w/v in culture media. The following additives were used: Dextran 500K (Pharmacosmo), PEG 35K (Sigma), and Ficoll 40 (Sigma) to generate similar viscosity with the different additives. Viscosity testing was done using a 52501/0b ubbelohde viscometer, testing each sample 5 times to determine average viscosity. The viscosity was determined prior to using the solutions as a spheroid culturing solution. Upon using the different solutions, spheroid formation was assessed against each culture condition.

Spheroid stability measurement

The stabilizing effects of polymer additives in hanging drop spheroid culture were assessed by video analysis. Spheroids with initial cell seeding number of 25 or 500 cells were cultured in medium with or without polymer additives (MethoCel, PEG, DEX, or Ficoll) for 2 days. Polymer-supplemented media were formulated to have comparable viscosities and osmolarities (Figure 4E). Spheroids in hanging drop plates were imaged on a Nikon Eclipse Ti inverted microscope at 10x magnification for 10 seconds at a frame rate of 100 frame/sec. Using an open source cell tracking software [28], the recorded images were analyzed to determine the center of

mass of each spheroid. The stability of spheroid was defined as the cumulative path length using a template-matching based tracking method. Cumulative path length was calculated by summing the total distance covered by the center of mass over 10 seconds (1000 frames total). In cases where cells formed more than one spheroid, the largest one out of the group was measured.

Oxygen depletion simulations

Finite element simulations were conducted in a commercially available finite element package (Comsol v. 4.2; Burlington, MA). To study the effect of spheroid shape on oxygen distributions, cells were assumed to consume oxygen equally throughout the cell aggregate. Equivalent-volume (33.5 μL) spherical and ellipsoidal geometries were generated using a 2D axisymmetric model, and the 'transport of diluted species' module was used to model oxygen consumption and transport within the spheroid. Appropriate parameters were selected based on values previously reported in the literature (diffusion coefficient $D = 2 \times 10^{-10}$ m^2/s [20], oxygen consumption rate $k = 3.09 \times 10^{-4}$ $mol/(m^3\ s)$ [21, 22]. To adjust for oxygen consumption differences in loose spheroids, the volumetric oxygen consumption rate was reduced by a factor equivalent to the expanded volume of the spheroid.

4.4 Conclusions

The multicellular spheroid model has found applications in many fields of biomedical research and will play a major role in next-generation drug-screening platforms. Using computational modeling we have demonstrated that the morphologies of a spheroid expressed as circularity and compactness, are both important parameters that determine its transport characteristics. We found that the morphologies of a spheroid is a function of cell type but can also be affected by the presence of additives in culture medium. We investigated the effect of collagen, an adhesive ECM protein, and MethoCel, a cell repelling polysaccharide, on spheroid morphologies. For all cell

types tested, use of moderate amounts of an appropriate additive improved spheroid morphology. MethoCel was beneficial for all cells except PC3 cells. Collagen, at low concentration, was beneficial for all cells except HeLa cells. Combinations of MethoCel and collagen in medium yielded mixed results depending on the cell type, highlighting the importance of tailoring additive formulations for specific spheroid models. The additive formulation that was always better than no additive was a combination of a low concentration of Methocel (0.24 mg/mL) and collagen (28.2 μg/mL). To obtain the highest degree of morphology improvement, however, each cell type would have to be tested for a broader range of additive formulations. In addition, we tested other macromolecule –supplemented medium formulations with similar viscosity and osmolarity as MethoCel and saw no improvement in spheroid morphology. This finding implies that the spheroid enhancement property of MethoCel cannot be entirely attributed to medium thickening alone. Overall, our results are in agreement with others in the literature and suggest that additives may affect spheroid morphologies by other biophysical factors unrelated to medium viscosity, such as altering ECM availability in the peri-cellular space.

4.5 References:

[1] Hirschhaeuser F, Menne H, Dittfeld C, West J, Mueller-Klieser W, Kunz-Schughart LA. Multicellular tumor spheroids: an underestimated tool is catching up again. J Biotechnol. 2010;148:3-15.

[2] Fennema E, Rivron N, Rouwkema J, van Blitterswijk C, de Boer J. Spheroid culture as a tool for creating 3D complex tissues. Trends in Biotechnology. 2013;31:108-15.

[3] Wirz W, Antoine M, Tag CG, Gressner AM, Korff T, Hellerbrand C, et al. Hepatic stellate cells display a functional vascular smooth muscle cell phenotype in a three-dimensional co-culture model with endothelial cells. Differentiation. 2008;76:784-94.

[4] Lin RZ, Chang HY. Recent advances in three-dimensional multicellular spheroid culture for biomedical research. Biotechnol J. 2008;3:1172-84.

[5] Kurosawa H. Methods for inducing embryoid body formation: in vitro differentiation system of embryonic stem cells. J Biosci Bioeng. 2007;103:389-98.

[6] Tung YC, Hsiao AY, Allen SG, Torisawa YS, Ho M, Takayama S. High-throughput 3D spheroid culture and drug testing using a 384 hanging drop array. The Analyst. 2011;136:473-8.

[7] Timmins NE, Dietmair S, Nielsen LK. Hanging-drop multicellular spheroids as a model of tumour angiogenesis. Angiogenesis. 2004;7:97-103.

[8] Kelm JM, Ehler E, Nielsen LK, Schlatter S, Perriard JC, Fussenegger M. Design of artificial myocardial microtissues. Tissue Eng. 2004;10:201-14.

[9] Wagner I, Materne EM, Brincker S, Sussbier U, Fradrich C, Busek M, et al. A dynamic multi-organ-chip for long-term cultivation and substance testing proven by 3D human liver and skin tissue co-culture. Lab Chip. 2013;13:3538-47.

[10] Hsiao AY, Tung YC, Qu X, Patel LR, Pienta KJ, Takayama S. 384 hanging drop arrays give excellent Z-factors and allow versatile formation of co-culture spheroids. Biotechnol Bioeng. 2012;109:1293-304.

[11] Hsiao AY, Tung YC, Kuo CH, Mosadegh B, Bedenis R, Pienta KJ, et al. Micro-ring structures stabilize microdroplets to enable long term spheroid culture in 384 hanging drop array plates. Biomed Microdevices. 2012;14:313-23.

[12] Ivascu A, Kubbies M. Diversity of cell-mediated adhesions in breast cancer spheroids. Int J Oncol. 2007;31:1403-13.

[13] Gwak SJ, Choi D, Paik SS, Cho SW, Kim SS, Choi CY, et al. A method for the effective formation of hepatocyte spheroids using a biodegradable polymer nanosphere. J Biomed Mater Res A. 2006;78:268-75.

[14] De Bank PA, Hou Q, Warner RM, Wood IV, Ali BE, Macneil S, et al. Accelerated formation of multicellular 3-D structures by cell-to-cell cross-linking. Biotechnol Bioeng. 2007;97:1617-25.

[15] Lin RZ, Chou LF, Chien CC, Chang HY. Dynamic analysis of hepatoma spheroid formation: roles of E-cadherin and beta1-integrin. Cell Tissue Res. 2006;324:411-22.

[16] Longati P, Jia X, Eimer J, Wagman A, Witt MR, Rehnmark S, et al. 3D pancreatic carcinoma spheroids induce a matrix-rich, chemoresistant phenotype offering a better model for drug testing. BMC Cancer. 2013;13:95.

[17] Haeger JD, Hambruch N, Dilly M, Froehlich R, Pfarrer C. Formation of bovine placental trophoblast spheroids. Cells Tissues Organs. 2011;193:274-84.

[18] Urich E, Patsch C, Aigner S, Graf M, Iacone R, Freskgard PO. Multicellular self-assembled spheroidal model of the blood brain barrier. Sci Rep. 2013;3:1500.

[19] Dang SM, Kyba M, Perlingeiro R, Daley GQ, Zandstra PW. Efficiency of embryoid body formation and hematopoietic development from embryonic stem cells in different culture systems. Biotechnol Bioeng. 2002;78:442-53.

[20] Sasaki N, Horinouchi H, Ushiyama A, Minamitani H. A new method for measuring the oxygen diffusion constant and oxygen consumption rate of arteriolar walls. Keio J Med. 2012;61:57-65.

[21] Mueller-Klieser W. Method for the determination of oxygen consumption rates and diffusion coefficients in multicellular spheroids. Biophys J. 1984;46:343-8.

[22] Grimes DR, Kelly C, Bloch K, Partridge M. A method for estimating the oxygen consumption rate in multicellular tumour spheroids. J R Soc Interface. 2014;11:20131124.

[23] Ivascu A, Kubbies M. Rapid generation of single-tumor spheroids for high-throughput cell function and toxicity analysis. J Biomol Screen. 2006;11:922-32.

[24] Debnath J, Brugge JS. Modelling glandular epithelial cancers in three-dimensional cultures. Nat Rev Cancer. 2005;5:675-88.

[25] Chen C, Loe F, Blocki A, Peng Y, Raghunath M. Applying macromolecular crowding to enhance extracellular matrix deposition and its remodeling in vitro for tissue engineering and cell-based therapies. Adv Drug Deliv Rev. 2011;63:277-90.

[26] Satyam A, Kumar P, Fan X, Gorelov A, Rochev Y, Joshi L, et al. Macromolecular crowding meets tissue engineering by self-assembly: a paradigm shift in regenerative medicine. Adv Mater. 2014;26:3024-34.

[27] Kojima N, Takeuchi S, Sakai Y. Rapid aggregation of heterogeneous cells and multiple-sized microspheres in methylcellulose medium. Biomaterials. 2012;33:4508-14.

[28] Sacan A, Ferhatosmanoglu H, Coskun H. CellTrack: an open-source software for cell tracking and motility analysis. Bioinformatics. 2008;24:1647-9.

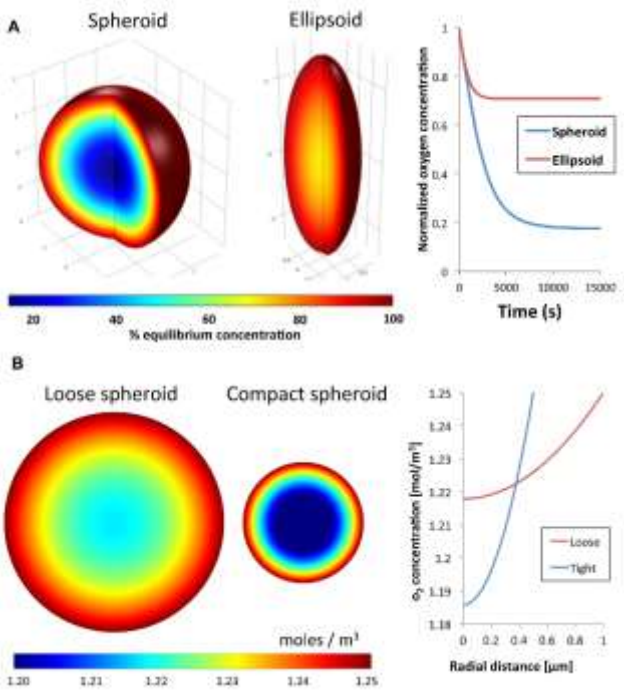

Figure 4-1: Computational models of oxygen gradients diffusion formed in a spheroid containing a constant number of cells with different circularity and compactness.
A) The model predicts that as the spheroid elongates and becomes less circular, the average core-to-surface distance decreases and the oxygen gradient decreases with the spheroid becoming more evenly saturated with oxygen. B) Similarly, modeling of a loose, non-compact spheroid demonstrates a shallower hypoxic gradient compared to a compact spheroid with the same number of cells due to the lower volumetric oxygen consumption rate.

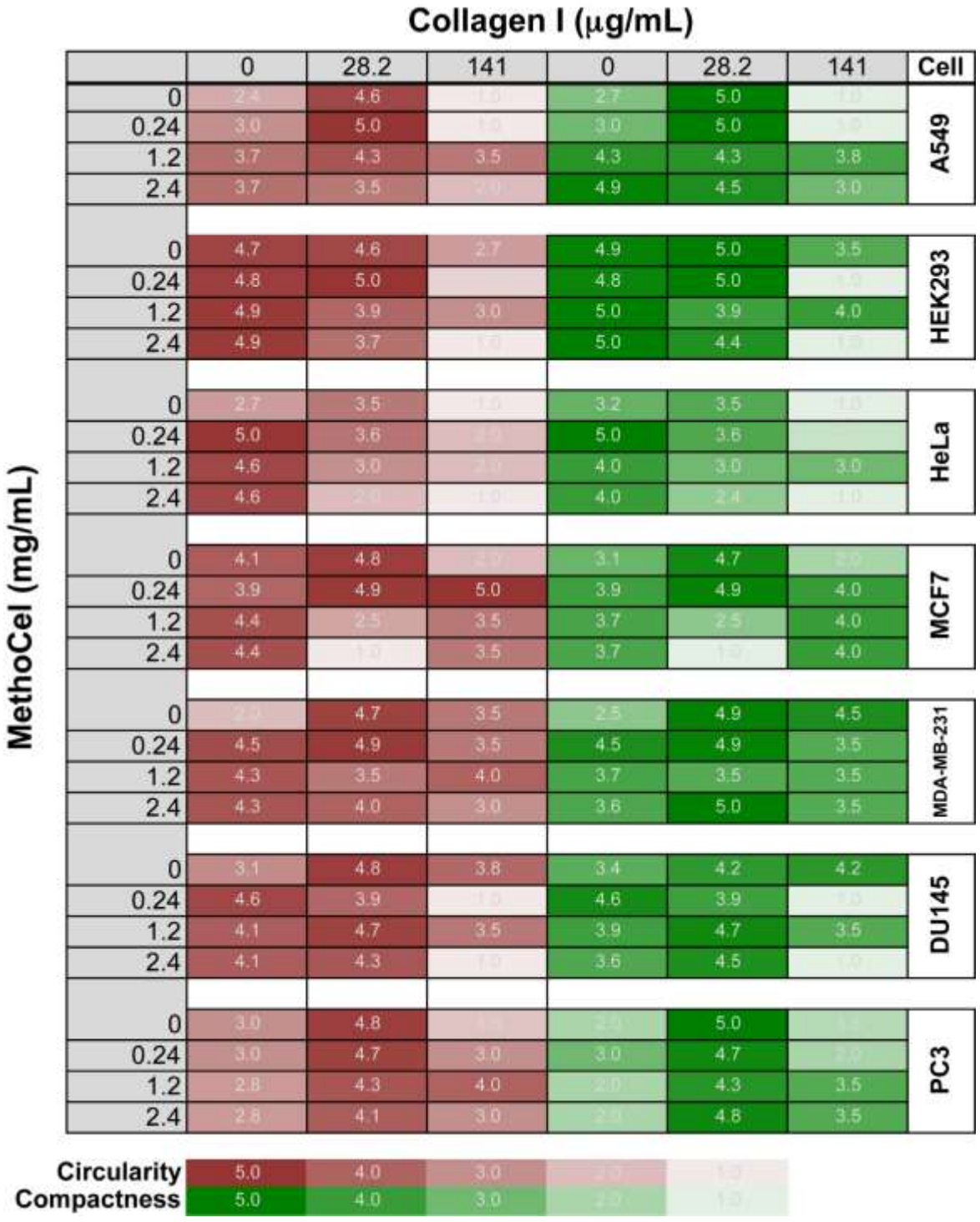

Figure 4-2: Circularity and compactness of spheroids after two days in culture.
Several common tumor cell lines were tested. Circularity and compactness were rated on a 5-point scale by blinded observers (n=2). Final score represent the average of 5 spheroids cultured in identical conditions.

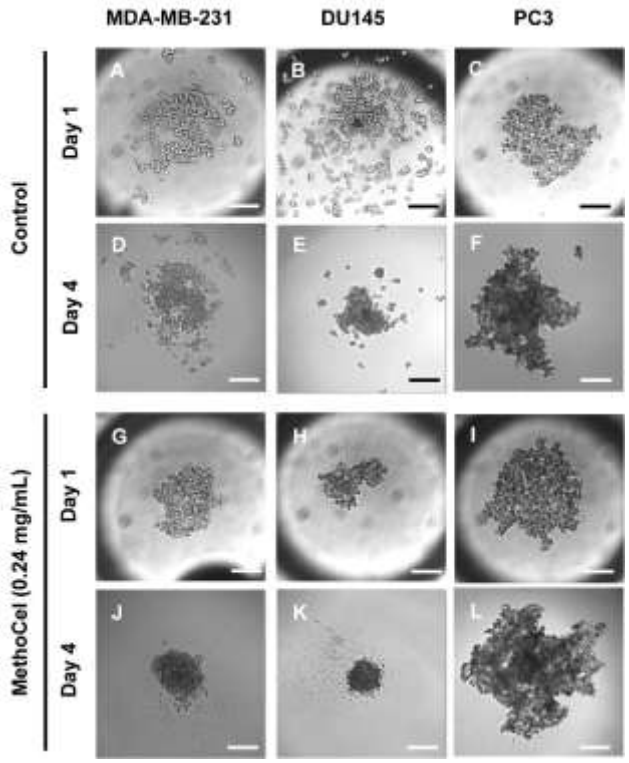

Figure 4-3: Changes in tumor spheroid morphologies over 3 days.
The presence of MethoCel improved both acute and sustained spheroid circularity and compactness. Scale bar = 200 μm

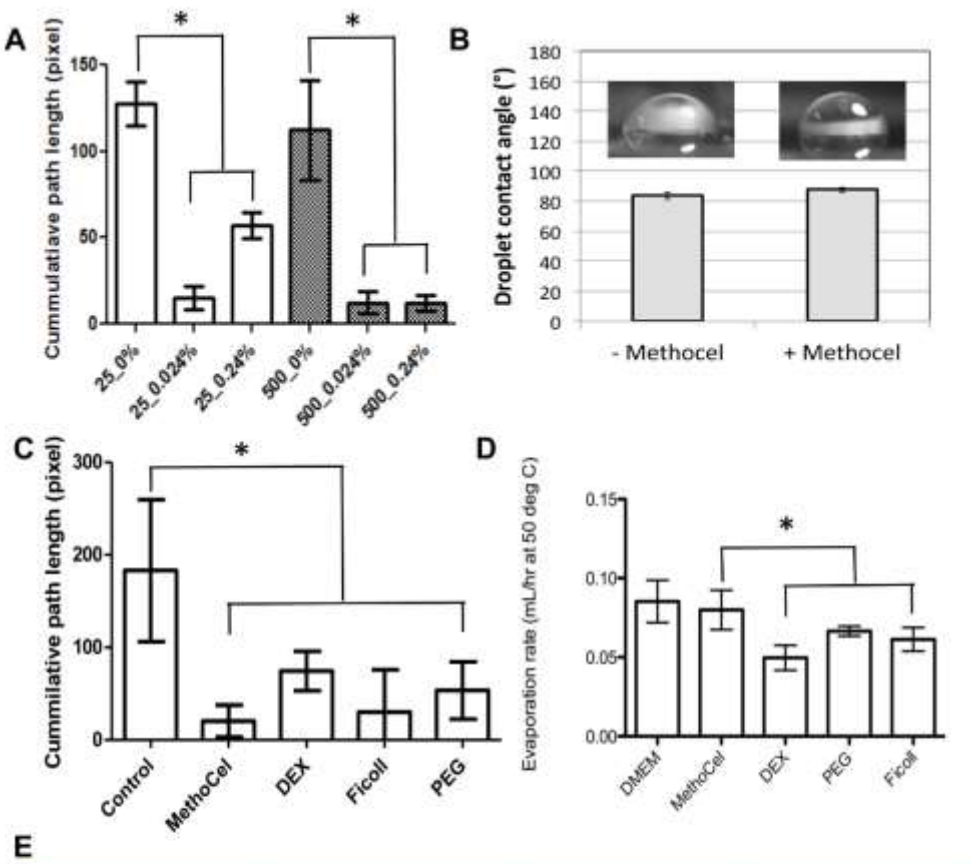

E

Additive	Additive Conc. (% w/v)	Viscosity (mm^2/s^2)	Osmolarity (mmol/kg)
MethoCel	0.024	1.1372	344
DEX 500K	0.383	1.2017	330
PEG 35K	0.297	1.1688	335
Ficoll 40	1.132	1.1889	336
FBS (control)	0	1.0322	344

Figure 4-4: Physical characterization of spheroids in hanging drop culture.
A) Presence of MethoCel improved the stability of hanging drop cultures (25 and 500 cells spheroids), evident by the reduction of cumulative path length compared to no additive controls (* $P<0.01$). B) The presence of MethoCel did not change the contact angle and evaporation rate of medium, suggesting minimal difference in thermo-convective flow within hanging drop culture. C) Media containing DEX, PEG or Ficoll at comparable viscosity to medium with MethoCel led to similar level of motion artifact reduction compared to no additive control (25 cells spheroids, * $P<0.05$). D) The presence of DEX, Ficoll and PEG led to slight reduction in evaporation rates compared to MethoCel supplemented medium (*$P<0.05$) E) Comparison of viscosity and osmolarity between media with different additives and control (10% FBS in DMEM).

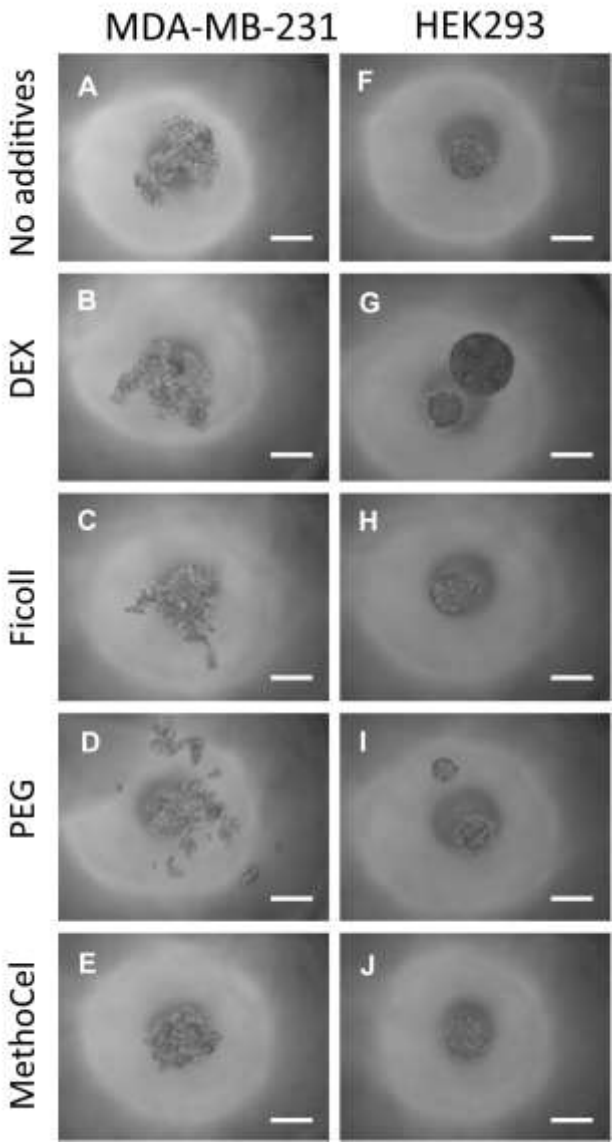

Figure 4-5: Effects of polymer additive in spheroid formation.
Media containing polymer additives (formulation in Figure 4E) were used to culture MDA-MB-231 and HEK293 cells. The presence of MethoCel (E) improved spheroid morphology in non-spheroid forming MDA-MB-231 cells. Other polymers (B, C and D) produced spheroids similar to control (A). In normally spheroid forming HEK293 cells (F), the presence of DEX (G) and PEG (I) led to the appearance of satellite bodies. MethoCel (J) and Ficoll (H) led to spheroids with normal morphologies. Scale bar = 200 μm

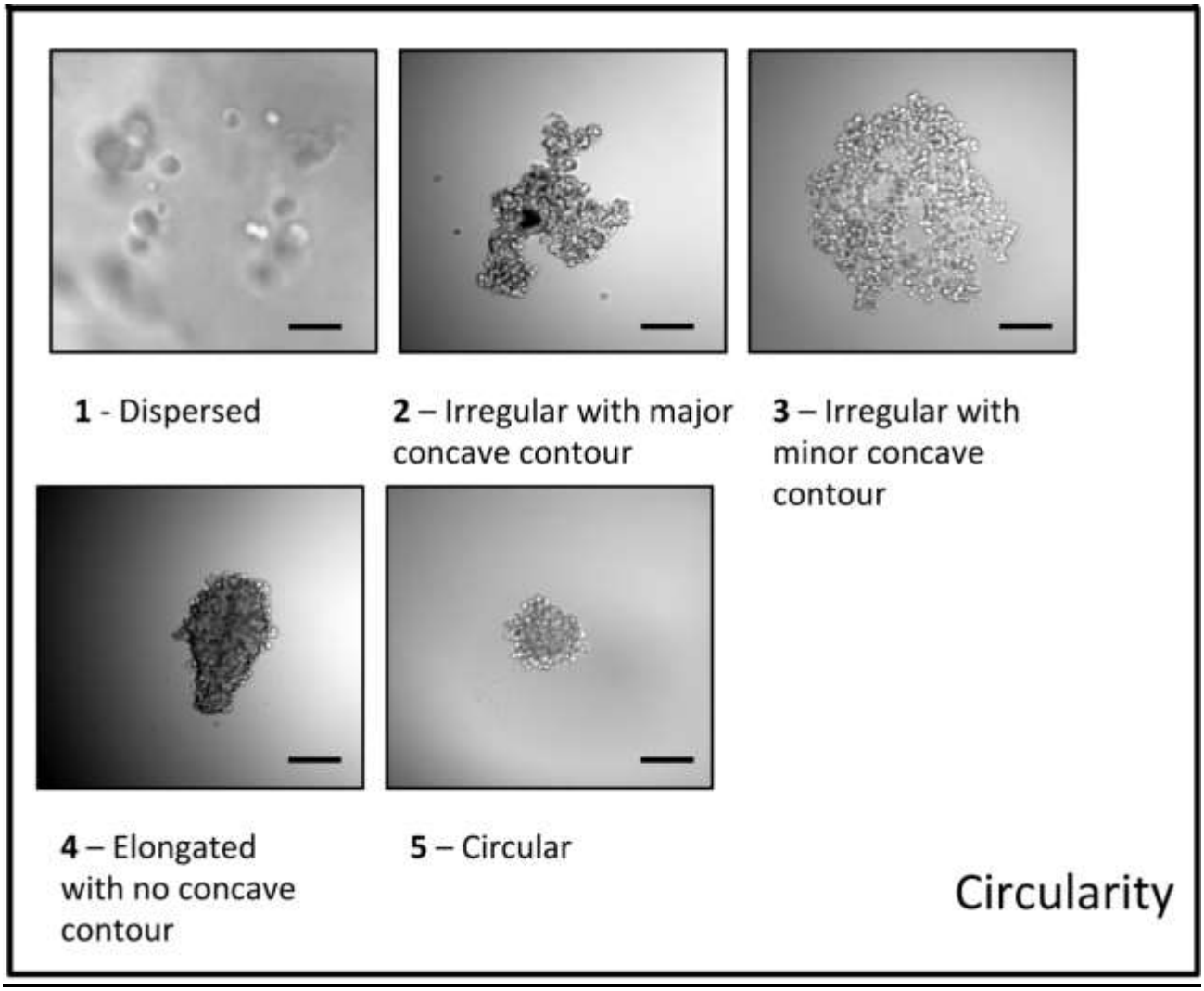

Figure 4-6: Scoring guide for circularity scores.
Scoring guide given to blinded scorer for the assignment of circularity score. Scale bar = 200 μm

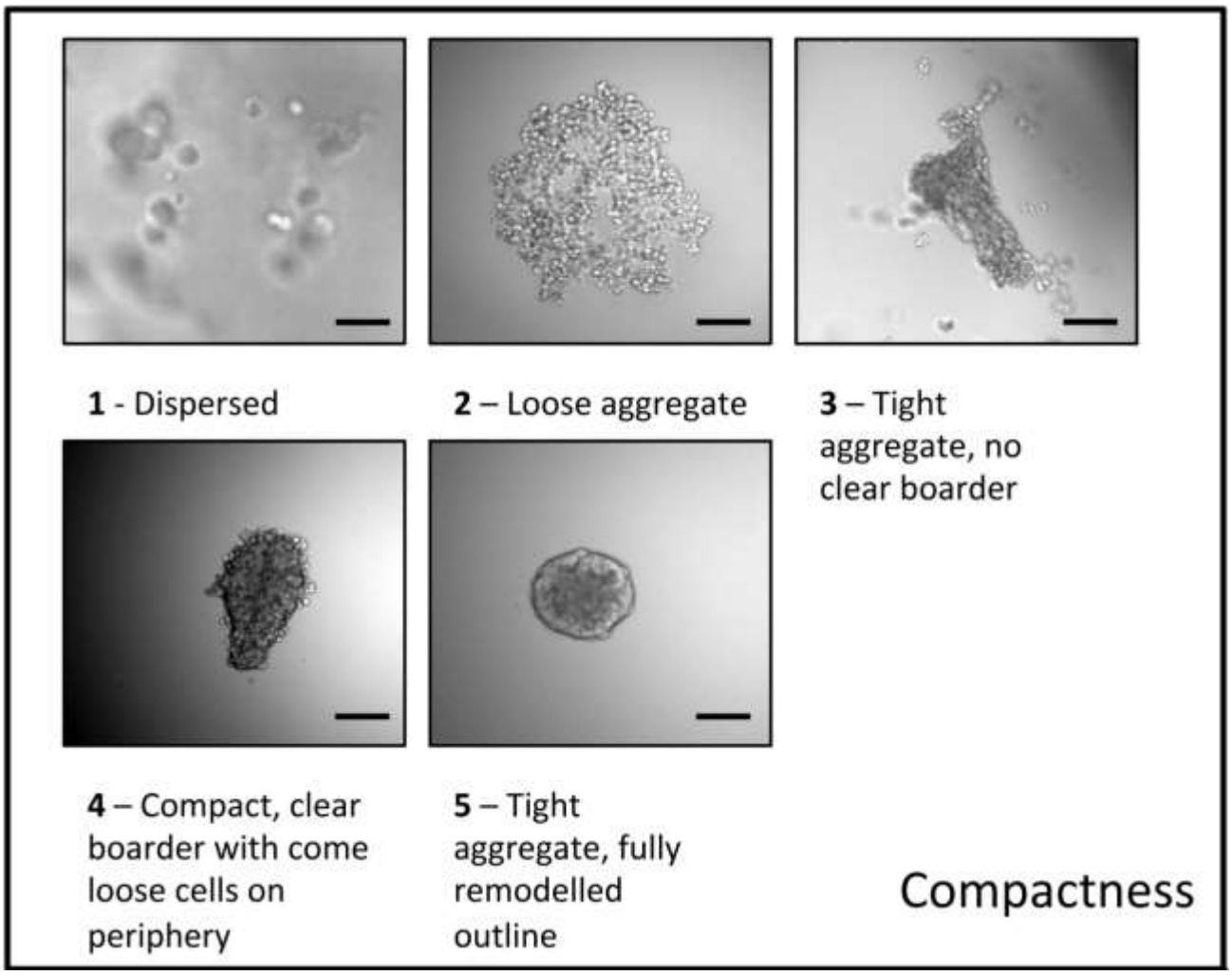

Figure 4-7: Scoring guide for compactness scores.
Scoring guide given to blinded scorer for the assignment of compactness score. Scale bar = 200 μm

Chapter 5: Dispersible oxygen microsensors map oxygen gradients in three-dimensional cell cultures.

5.1 Introduction

Three-dimensional (3D) cultures that utilize hydrogels[1] or specialized culture vessels are increasingly used to elicit more physiological cellular responses compared to conventional 2D cultures[2]. Oxygen levels within these tissue cultures is an important regulator of cell function. Physiological oxygen levels *in vivo*, range from ~14% in the alveoli down to ~3% oxygen in some tissues[3], and still lower levels in tissues with different pathologies, such as tumors, ischemia, and obesity[4,5]. To develop culture systems with oxygen tension profiles that portray the spatially and temporally dynamic oxygen environments *in vivo*, robust monitoring systems are needed to map oxygen levels within these increasingly complex *in vitro* tissue cultures.

Historically, Clark electrodes or variations thereof have been employed as oxygen sensors[6]. These oxygen detectors are reliable but consume oxygen and can thus also alter the local concentration during measurements[7]. Miniaturized micro-electrodes can reduce such consumption and are able to fit within micropipettes[8], but the need to pierce tissue constructs, limits the oxygen measurements to a singular point; where inserting an array, may both damage the tissue, as well as significantly alter the oxygen concentration throughout the tissue. Also the need for sensor electrodes and electrical connections make it difficult to handle/manipulate the sample with the embedded sensor[7].

Optical sensors and luminophores have also been developed to study cellular oxygen microenvironments. Phosphorescent organometallic complexes are particularly useful due to their rich excited states, large shift between excitation and emission wavelength (Stokes' shift), long decay lifetimes, high luminescence quantum yields and high stability in regards to oxygen sensing[9]. These complexes have been employed in different modalities/structures, such as nano-particles[10,11]/-fibers[12,13], thin films[14,15], microplates[16], and microbeads[17,18]. The majority of the cell culture work done with laboratory sensor systems in the various formats rely on intensity-based measurements, which are easily affected by light path differences from culture vessels and optical attenuation by dense 3D cell cultures and hydrogels. Thin films, patches, and plates, such as the Ocean Optics neoFox® which utilize phase fluorimetry to measure oxygen, or microplates such as the Becton-Dickinson Biosensor® plates can utilize temporal (phase) based imaging techniques[19]. Unfortunately, these commercial sensor systems are too large to be placed within microscale tissue culture systems limiting these technologies to peripheral measurements.

Here, we describe an optical oxygen microsensor –fabricated by infusing PDMS microbeads with an oxygen-sensitive ruthenium dye– that is non-toxic and provide real-time oxygen monitoring of cell culture of extended periods. The beads are used with phase fluorimetry, which uses oxygen lifetime-quenching instead of intensity-quenching to mitigate the drawbacks associated with intensity-based measurements[20,21]. We use the sensor beads to characterize peri-cellular oxygen concentrations for cell spheroids cultured in microwells versus hanging drops. Because of the high stability and very small sensor-to-sensor variability, multiple microsensors could be dispersed throughout 3D cell cultures and hydrogel constructs to provide maps of the spatial distribution of oxygen levels without the need for multiple calibrations. We believe these

small and robust oxygen sensors will be useful for a variety of 3D cell culture, organ-on-a-chip, and tissue engineering applications where oxygen plays a key role in determining cell function.

5.2 Methods and Materials

Generation of PDMS beads

PDMS beads were generated using microfluidic flow focusing devices typically used for droplet generation. Specifically, we used a 3-to-1 converging flow-focusing micro-channel (100 µm high channels) device to fabricate PDMS beads, however, the device design can be modified to generate beads of different sizes[22]. Microfluidic flow focusing devices used the same master fabrication, and PDMS layer preparation as previously presented[23]. PDMS layer, had inlets and outlets punched biopsy punches, prior to plasma bonding the PDMS layer onto a glass slide. Metal blunt end needle-tips (Jensen Global, Santa Barbara, CA, USA) were used to connect tubing into device; Tygon tubing (Saint-Gobain™ Tygon™ R-3603 Clear Laboratory Tubing, Saint-Gobain Performance Plastics, Akron, OH, USA) was inserted into continuous flow inlets, whereas PTFE Tubing (Cole-Parmer, Vernon Hills, IL, USA) was directly inserted into dispersive flow inlet. Inserted tubes and tips were sealed with uncured 1:10 – PDMS.

After fabrication, devices were prepared for bead generation by applying corona treatment to the device, to enhance hydrophilicity of the microchannels; immediately after a surfactant solution of either 0.1% (w/v) Pluronic F108 (BASF Co., Ludwigshafen, Germany) or 0.5% (w/v) Sodium Dodecyl Sulfate (Sigma Aldrich, Saint Louis, MO, USA) in dH_2O was flowed through tubing and channels. For flow focusing, the surfactant solution of 0.1% Pluronic F108 0.5% SDS was flowed through the side channels, to make up the continuous phase, and a 1:1 mixture of toluene and 1:10 PDMS pre-polymer solution (Sylgard 184, Dow Corning, Midland, MI, USA) was flowed through the middle channel, making up the dispersive phase. Flows were driven by two

distinct syringe pumps (KD Scientific, Holliston, MA, USA) to differentially modulate flow rates. Flow rates were slowly ramped up and down in the continuous and dispersive flows, respectively. Flow rate ramping steps for both continuous phase driving pumps and disperse phase driving pump are controlled carefully to minimize the time needed to initiate convergence of two liquid phases, and to maintain stable focusing flow in the microchannel device.

The low surface energy of the surfactant solution helps to maintain the PDMS micro-droplets in the outlet reservoir after they have been formed. After being collected at the outlet reservoir into glass scintillation vials, the PDMS microdroplets were cured at 60 ºC overnight, forming solid PDMS microspheres. In experimental observations, the size of the cured PDMS microspheres do not change significantly compared to the pre-cured microdroplets (data not shown).

Infusion of Ruthenium into PDMS for O_2 Sensing

Post fabrication, beads were washed with dH_2O. dH_2O solution was removed, and 5mg/mL of tris(4,7-diphenyl-1,10-phenanthroline) ruthenium(II) dichloride (Alfa Asar, Ward Hill, MA, USA) in dichloromethane (Sigma, Saint Louis, MO, USA) was introduced into the scintillation vial. Beads were allowed to incubate in the ruthenium-dicholoromethane solution for 24 hours at room temperature, in the dark. The majority of ruthenium-dicholoromethane solution was removed from the scintillation vial, and 5 mg/mL of ruthenium in isopropanol was applied onto the beads for 30 minutes to dilute out the dichloromethane (at least 1:4 dilution). The isopropanol was then removed, and the beads were washed with dH_2O to remove organic solvents. Final washes were done in 0.1% Pluronic F108 to minimize bead sticking.

Calibration of PDMS Microsensors

Phase-shift measurements (phase fluorimetry) were taken of the oxygen microsensing beads using a microscope with a fluorescence attachment connecting a monochromatic 455 nm 5 W LED light source (Mightex Systems, CA) to excite the beads in a pulsatile manner. The LED was driven by a function generator (33220A, Agilent Technology, Inc., CA, USA), with a square wave at a 100 kHz frequency and 50% duty cycle. A 590 long pass filter was used, to minimize extraneous noise; silicon PIN photodiode with preamplifier (PDA36A, Thorlabs, Inc., NJ, USA) was used to capture fluorescent emission. The PIN photodiode, was set at a gain of 30 dB, and was connected to a lock-in amplifier (SR830, Stanford Research System, Inc., Sunnyvale, CA, USA) for output signal assessment and comparison. The system is controlled by a personal computer with LabVIEW graphic user interface program for operation with data acquisition through a GPIB interface (LabView and GPIB-USB-HS, respectively, National Instruments, Co., Austin, TX, USA). A schematic similar to the setup used in this work can be seen in previously published work[24]. Beads were measured at 21% (room air), 15%, 10%, 5%, 2.5% and 0% O_2; measurements were taken by flowing in a pre-mixed N_2 and O_2 gas composition (Cryogenic Gases Inc., Detroit, MI, USA) into a custom-made purging chamber, except when equilibrating with air, which was allowed to equilibrate to ambient conditions. Beads responded and stabilized $\leq$ 10 seconds of gas flow into the purging chamber (specific time dependent on bead size), for calibration a minimum of a minute of gas flow was used. All measurements also captured intensity data for beads, which was used for the intensity based measurements.

Cell Culture

All cells, Human Embryonic Kidney 293T (HEK 293T) cells(ATCC® CRL-1573™); Human Bone Marrow Stroma (HS-5) cells (ATCC® CRL-11882™); Human Epithelial Adenocarcinoma MDA-MB-231-eGFP cells used were cultured with Dulbecco's modified Eagle medium (Gibco,

Carlsbad, CA, USA) supplemented with 10% fetal bovine serum (FBS) and 1% antbiotic-antimycotic. Medium was refreshed every 2 to 3 days and cells passaged, using 0.25% Trypsin/EDTA (Gibco, Carlsbad, CA, USA) when sub-confluent, 70~80%.
Cytotoxicity assessment was done with HS-5 cells. HEK 293T cells were used for spheroid cultures. MDA-MB 231 cells with constitutively expressed eGFP were used for cell-laden hydrogel work, to assess cell generated oxygen gradients.

Assessing Live/Dead (Cytotxicity)

HS-5 cells were cultured with beads for 36 hours and 120 hours, on tissue culture plates (Corning, NY). Impact of ruthenium loaded microbeads on cell viability was assessed using the LIVE/DEAD cytotoxicity kit (Invitrogen, Waltham, MA, USA). Samples were washed with dPBS (Gibco, Carlsbad, CA, USA), and then incubated with a 2 µM calcein AM and 4 µM ethidium homodimer in dPBS for 30 minutes before aspirating and washing with dPBS. Images were collected around and away from beads using a digital camera (Canon EOS Rebel T3i, Canon, Japan), and then analyzed either by imageJ or counting manually.

Assessing oxygen levels generated by spheroids in different culture formats

Spheroids were generated using high-throughput hanging drop array plates[25] using culture methods recently presented[26]. Prior to usage, a hydrophilic coating was applied onto the entire hanging drop plate surface by soaking the plate overnight in 0.1%, Pluronic F108. The plate was then dried and UV sterilized before cell seeding. To form hanging drops, 25 µL of a cell suspension solution of 2.0×10^5 HEK 293T cells/mL was pipetted from the top side through the access holes with the end of each pipette tip inserted into the access hole to guide the sample liquid to the bottom surface. Media was supplemented with A4M MethoCel (Dow Chemical Co.,

Auburn Hills, MI, USA) at 0.024% (w/v). Spheroids were formed over 24 hours, at this time microsensors were either placed into hanging drops with spheroids, or within round bottom 96 well plate wells. Round bottom wells were then filled with 1, 5, 10 or 50 spheroids. Microsensors were also placed in media only hanging drops and round bottom wells as controls. Spheroids were monitored a minimum of 18 hours in the different culture formats.

Mapping oxygen distribution in cell pattered hydrogels

A more complete protocol to generate a spatially-patterned cell laden collagen hydrogel, surrounded by a cell-free collagen hydrogel was previously described[27]. Briefly the spatial patterning was done by coating PDMS onto a glass slide, which was then covered with polyacrylamide. The polyacrylamide coating was selectively oxidized using a protective mask and applying plasma oxidation (Covance MP, FemtoScience, Hwaseong-si, Gyeonggi-do, South Korea). Trypsinized MDA-MB-231 e-GFP cells were mixed with the oxygen microsensors and neutralized type I bovine collagen (BD Biosciences, San Jose, CA, USA), to create a suspension of 1.0×10^7 cells/mL and 2,000 beads/mL in 2 mg/mL of collagen; 8 µL of the suspension was dispensed onto the adhesive pattern, and allowed to polymerize for 45 minutes at 37 °C. The overlaying gel was made up to create a suspension of oxygen microsensors 200 beads/mL in 2.5 mg/mL collagen, 250 µL were dispensed over the polymerized core region, and incubated at 37 °C for 1 hour to polymerize the overlaying gel. 2 mL of cell culture media were added to each well and the samples were cultured at 37 °C. Microsensor distance from the center of the cell-laden region was used to map oxygen levels throughout the 3D tissue culture after 24 hours of culturing (steady state).

5.3 Results

Generation of oxygen microsensors

Dispersible microsensors were generated by first successfully producing PDMS microbeads using a microfluidic flow focusing system (Figure 1a), generation of monodispersed beads (Figure 1b,c) was possible with the appropriate flow rates; where modification of bead size could be accomplished by modifying device architecture[22] (i.e. aperture of dispersive flow), or ratio of continuous and dispersive flow rates[28]. Changing flow rate can generate differing size beads, but may also lead to an increase in bead polydispersity. PDMS beads were successfully infused with ruthenium (Figure 1d).

Microsensor calibration and lifespan assessment

Ruthenium infused microbeads demonstrated luminescent differences as oxygen was modified between 0% and 21% in our calibration chamber (Figure 2a, b), indicating oxygen sensing capability. These microsensors were calibrated using two modalities: intensity-based quenching and phase fluorimetry, (Figure 2 a, and c, respectively). Consistent with previous work with other intensity-based calibration curves published[14,17] significant variations exist in calibration curves (using Stern-Volmer relationship), particularly at higher oxygen levels. Phase shift measurements (Figure 2C) presented minimal variation at the different oxygen levels measured. These experiments were repeated across 5 batches of fabricated beads, demonstrating reliable and consistent measurement capabilities.

To determine the working-/shelf-life of our sensors, we assessed stability of the phase fluorimetry signal for months after fabrication. Phase fluorimetery is independent of oxygen based changes in intensity levels, however, this imaging method does require sufficient intensity

to detect the optical signal. Reduction of the signal intensity overtime for one bead is presented (Figure SI 2) against the respective phase shift measurements. Additionally the average reduction of beads exposed to light in ambient room conditions for one week, demonstrated a drop in intensity by ~ 22.5% whereas the phase fluorimetry measurements had an average fluctuation of ~ 2.4% (Table SI 1). As long as the signal intensity for microsensors was above the detection threshold limit, we demonstrated reproducible phase shift measurements for up to one year (Figure 2d) when cycling between the two extremes of interest: normoxic (21% O_2) and anoxic (0% O_2).

Microsensor cell culture compatibility

Microsensor cell biocompatibility was assessed by performing live/dead assay on cells cultured with microsensors to identify any cytotoxic effects. We exposed multiple cell types to our microsensors and did not see any changes that indicated concerns for cell viability. We specifically quantified cell viability culturing with HS-5 cells at 36 hours (Figure SI 1), and at 120 hours (data not shown) and saw no appreciable cell death in the HS-5 or in the other cell cultures.

Oxygen monitoring in different spheroid culture platforms

Dispersible oxygen microsensors were used to compare two different spheroid culture formats, hanging drops and 96 well round bottom plates. Oxygen levels were measured after 18 hours when culturing a single HEK 293T spheroid (5.0×10^3 cells/spheroid) in these two culture formats. Spheroids in hanging drop cultures did not change oxygen levels in the media as compared to media controls (hanging drop or round bottom well), whereas oxygen levels around spheroids in round bottom wells were lower (Figure 3a). Since a significant drop in oxygen was

measured in the microwell even with just a single spheroid, the platform was further interrogated for effects with multiple spheroids. As seen in Figure 3a, more spheroids (e.g. one, five, ten, and fifty) resulted in lower steady-state (18 hr) oxygen levels. Figure 3b shows the ability to perform real-time, continuous monitoring of pericellular oxygen concentrations as well as the spheroid number-dependence (1, 5, or 50 spheroids) of the rate of decrease in oxygen concentration.

Oxygen gradient mapping of 3D hydrogel cultures

Oxygen microsensors were also integrated into micropatterned cell-laden hydrogel constructs[27] (Figure 4a, b). Using phase fluorimetry, we mapped oxygen from hypoxic levels of 0.5% O_2 within the interior of the cell laden region to higher oxygen levels in the cell-free regions with a discontinuity point between the cell-laden/cell-free border (Figure 4c).

5.4 Discussion

Importance of oxygen not only as an essential cell substrate for cell survival and growth but also as a regulatory molecule that induces different gene expression and function in cells, together with a recent increase in the use of 3D cell culture platforms has led to a need for new oxygen sensors that are non-toxic to cells, non-tethered, microscale, and reliable. This need has led to development of a variety of microscale optical oxygen sensors. Similar size oxygen sensors, composed of PDMS partially or in whole, have previously been reported but relied solely on fluorescence intensity oxygen measurements.[17,18] Intensity-based measures are generally less accurate and reliable due to sensor production heterogeneity that lead to inherent intensity differences, photobleaching over time, and variable light attenuation unavoidable in most 3D cell and hydrogel cultures. Even ratiometric imaging with an oxygen-insensitive reference dye present challenges as photobleaching properties will be different and the emission spectra will be

different resulting in differential signal attenuation of signal from each dye, thus skewing the ratiometric relationship and consequently oxygen measurements.

In contrast, phase fluorimetric measurements at a given temperature[20,24] are only impacted by the molecular response to oxygen within the sensors. This eliminates inconsistencies that arise from optical path variability inherent to 3D tissues.[29] Indeed our microsensors demonstrate much tighter reproducibility across the physiological range of oxygen concentration (Figure 2c) using phase fluorimetry compared to intensity-based measurements. Further the microsensors retained the tightly reproducible oxygen measurement function for up to a year (Figure 2d). The longevity of these microsensors should suffice for the duration of most *in vitro* tissue culture experiments. The reproducibility and tightness of the phase fluorimetry measures extend across different beads, over different batches, as well as the longevity of the measurement systems reminiscent of commercial patch and film systems which are typically much larger and difficult to disperse in 3D cultures.

After validating their robustness, we used the microsensors to evaluate different 3D cell cultures. We observed higher oxygen levels (similar to no cell controls) in hanging drop spheroid cultures, whereas round bottom microwell cultures showed significantly lower oxygen levels at 18 hours. We attribute these differences the distance between the spheroids and the air-liquid interface (0 mm for the hanging drops and 6 mm for the microwells). Because of the less efficient oxygen transfer rate of microwells, an increase in cell mass (number of spheroids) led to even lower steady-state oxygen levels (Figure 3a) some of which approach hypoxic/anoxic levels[30–32]. We also mapped the oxygen profile (Figure 4c) for a micropatterned cell-laden hydrogel culture (Figure 4a, b). This demonstrates the accuracy and versatility of the sensor and its ability to

measure hypoxic to normoxic to ambient air levels of oxygen in 3D cell cultures. The method may also be useful as a method for assessing oxygen uptake rate of cells in 3D hydrogel cultures.

5.5 Conclusions

Accurate measurement and mapping of oxygen gradients in 3D cell cultures present new challenges for an old category of biosensors. Utilizing the temporal-domain over intensity-based optical oxygen measurements, phase fluorimetry drastically reduced measurement errors and uncertainties that arise from heterogeneity in microsensor fabrication, signal decay over time, and the attenuation and scattering effects that may be present when imaging in tissues and hydrogels. The biocompatibility and small size of the microsensors allowed convenient dispersion of the sensors within different 3D cell culture formats to assess their oxygen levels. The accuracy of the microsensors were demonstrated by mapping the oxygen concentrations in a micropatterned cell-laden hydrogel and showing clear discontinuities in the oxygen gradient between the cell-laden and cell-free regions. We envision these microsensors and optical detection protocols to be useful in a broad range of culture systems such as bioreactors, organoid cultures, and 3D organ-on-a-chip systems.

5.6 References

1. Pampaloni, F., Reynaud, E. G. & Stelzer, E. H. K. The third dimension bridges the gap between cell culture and live tissue. *Nat. Rev. Mol. Cell Biol.* **8,** 839–845 (2007).

2. Moraes, C., Mehta, G., Lesher-Perez, S. C. & Takayama, S. Organs-on-a-Chip: A Focus on Compartmentalized Microdevices. *Ann. Biomed. Eng.* **40,** 1211–1227 (2011).

3. Carreau, A., Hafny-Rahbi, B. E., Matejuk, A., Grillon, C. & Kieda, C. Why is the partial oxygen pressure of human tissues a crucial parameter? Small molecules and hypoxia. *J. Cell. Mol. Med.* **15,** 1239–1253 (2011).

4. Hosogai, N. *et al.* Adipose Tissue Hypoxia in Obesity and Its Impact on Adipocytokine Dysregulation. *Diabetes* **56,** 901–911 (2007).

5. Trayhurn, P. Hypoxia and Adipose Tissue Function and Dysfunction in Obesity. *Physiol. Rev.* **93,** 1–21 (2013).

6. Clark, L. C. & Lyons, C. Electrode Systems for Continuous Monitoring in Cardiovascular Surgery. *Ann. N. Y. Acad. Sci.* **102,** 29–45 (1962).

7. Grist, S. M., Chrostowski, L. & Cheung, K. C. Optical Oxygen Sensors for Applications in Microfluidic Cell Culture. *Sensors* **10,** 9286–9316 (2010).

8. Silver, I. A. Polarography and its Biological Applications. *Phys. Med. Biol.* **12,** 285 (1967).

9. Feng, Y., Cheng, J., Zhou, L., Zhou, X. & Xiang, H. Ratiometric optical oxygen sensing: a review in respect of material design. *The Analyst* **137,** 4885 (2012).

10. Kuang, Y. & Walt, D. R. Detecting oxygen consumption in the proximity of Saccharomyces cerevisiae cells using self-assembled fluorescent nanosensors. *Biotechnol. Bioeng.* **96,** 318–325 (2007).

11. Clark, H. A., Hoyer, M., Parus, S., Philbert, M. A. & Kopelman, R. Optochemical Nanosensors and Subcellular Applications in Living Cells. *Microchim. Acta* **131,** 121–128 (1999).

12. Rosenzweig, Z. & Kopelman, R. Development of a Submicrometer Optical Fiber Oxygen Sensor. *Anal. Chem.* **67,** 2650–2654 (1995).

13. Xue, R., Behera, P., Viapiano, M. S. & Lannutti, J. J. Rapid response oxygen-sensing nanofibers. *Mater. Sci. Eng. C Mater. Biol. Appl.* **33,** 3450–3457 (2013).

14. Thomas, P. C. *et al.* A Noninvasive Thin Film Sensor for Monitoring Oxygen Tension during in Vitro Cell Culture. *Anal. Chem.* **81,** 9239–9246 (2009).

15. Fernández-Sánchez, J. F., Cannas, R., Spichiger, S., Steiger, R. & Spichiger-Keller, U. E. Novel nanostructured materials to develop oxygen-sensitive films for optical sensors. *Anal. Chim. Acta* **566,** 271–282 (2006).

16. Wang, W., Upshaw, L., Strong, D. M., Robertson, R. P. & Reems, J. Increased oxygen consumption rates in response to high glucose detected by a novel oxygen biosensor system in non-human primate and human islets. *J. Endocrinol.* **185,** 445–455 (2005).

17. Jiang, K., Thomas, P. C., Forry, S. P., DeVoe, D. L. & Raghavan, S. R. Microfluidic synthesis of monodisperse PDMS microbeads as discrete oxygen sensors. *Soft Matter* **8,** 923–926 (2012).

18. Wang, L., Acosta, M. A., Leach, J. B. & Carrier, R. L. Spatially monitoring oxygen level in 3D microfabricated cell culture systems using optical oxygen sensing beads. *Lab. Chip* **13,** 1586 (2013).

19. Rolo, A. P., Palmeira, C. M. & Cortopassi, G. A. Biosensor plates detect mitochondrial physiological regulators and mutations in vivo. *Anal. Biochem.* **385,** 176–178 (2009).

20. McDonagh, C. *et al.* Phase fluorometric dissolved oxygen sensor. *Sens. Actuators B Chem.* **74,** 124–130 (2001).

21. Holst, G. A., Köster, T., Voges, E. & Lübbers, D. W. FLOX—an oxygen-flux-measuring system using a phase-modulation method to evaluate the oxygen-dependent fluorescence lifetime. *Sens. Actuators B Chem.* **29,** 231–239 (1995).

22. Lee, W., Walker, L. M. & Anna, S. L. Role of geometry and fluid properties in droplet and thread formation processes in planar flow focusing. *Phys. Fluids 1994-Present* **21,** 032103 (2009).

23. Lesher-Perez, S. C., Weerappuli, P., Kim, S.-J., Zhang, C. & Takayama, S. Predictable Duty Cycle Modulation through Coupled Pairing of Syringes with Microfluidic Oscillators. *Micromachines* **5,** 1254–1269 (2014).

24. Mehta, G. *et al.* Hard Top Soft Bottom Microfluidic Devices for Cell Culture and Chemical Analysis. *Anal. Chem.* **81,** 3714–3722 (2009).

25. Tung, Y.-C. *et al.* High-throughput 3D spheroid culture and drug testing using a 384 hanging drop array. *Analyst* **136,** 473–478 (2011).

26. Leung, B. M., Lesher-Perez, S. C., Matsuoka, T., Moraes, C. & Takayama, S. Media additives to promote spheroid circularity and compactness in hanging drop platform. *Biomater. Sci.* **3,** 336–344 (2015).

27. Kojima, T., Moraes, C., Cavnar, S. P., Luker, G. D. & Takayama, S. Surface-templated hydrogel patterns prompt matrix-dependent migration of breast cancer cells towards chemokine-secreting cells. *Acta Biomater.* **13,** 68–77 (2015).

28. Anna, S. L., Bontoux, N. & Stone, H. A. Formation of dispersions using ‘flow focusing’ in microchannels. *Appl. Phys. Lett.* **82,** 364–366 (2003).

29. Welch, A. J., Yoon, G. & Van Gemert, M. J. C. Practical models for light distribution in laser-irradiated tissue. *Lasers Surg. Med.* **6,** 488–493 (1987).

30. Mueller-Klieser, W. Method for the determination of oxygen consumption rates and diffusion coefficients in multicellular spheroids. *Biophys. J.* **46,** 343–348 (1984).

31. Acker, H., Carlsson, J., Mueller-Klieser, W. & Sutherland, R. M. Comparative pO2 measurements in cell spheroids cultured with different techniques. *Br. J. Cancer* **56,** 325–327 (1987).

32. Kunz-Schughart, L. A., Groebe, K. & Mueller-Klieser, W. Three-dimensional cell culture induces novel proliferative and metabolic alterations associated with oncogenic transformation. *Int. J. Cancer* **66,** 578–586 (1996).

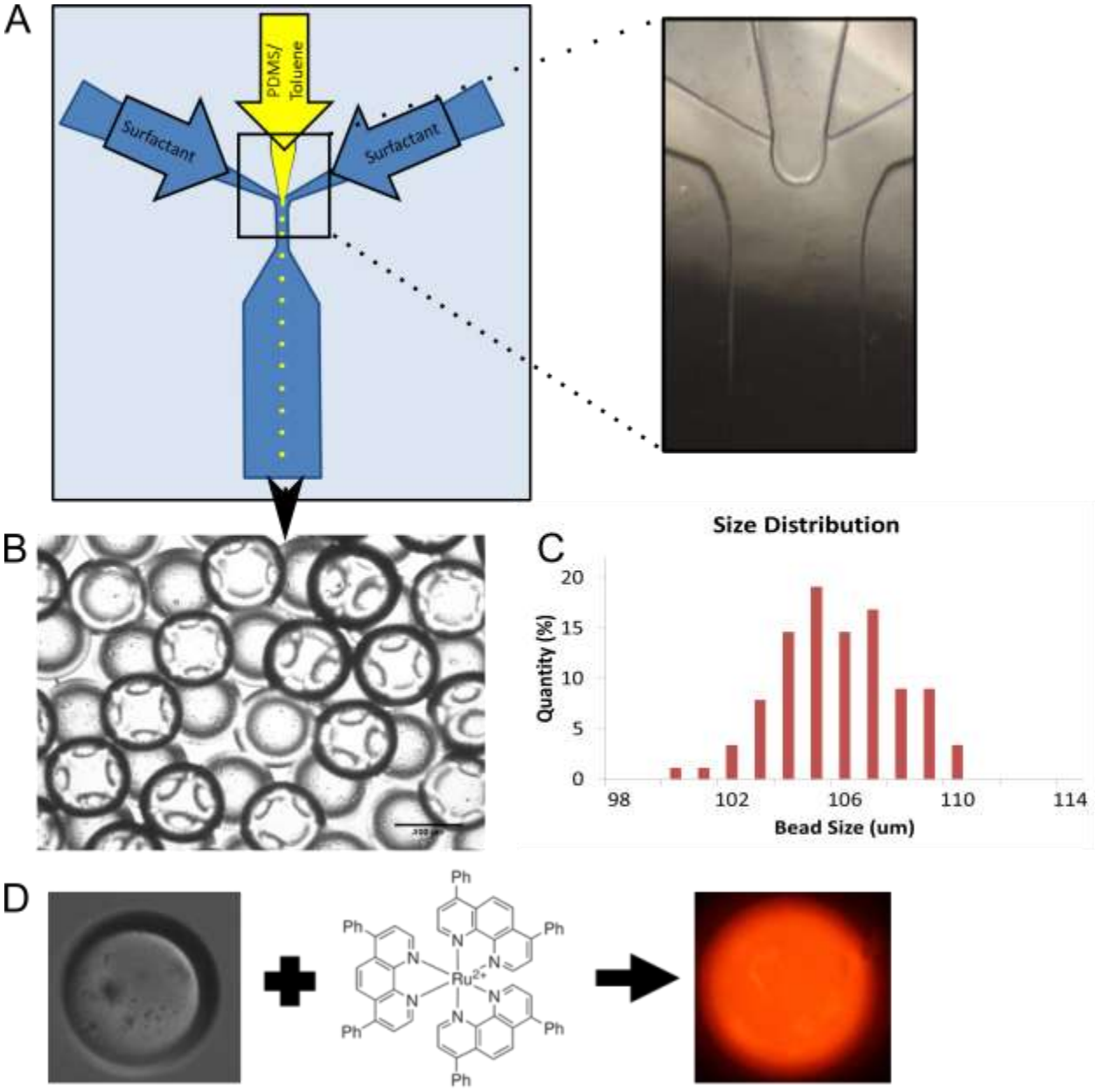

Figure 5-1: Microbead generation to produce microsensors.
A) Flow focusing schematic demonstrating a dispersive flow of PDMS-toluene with surfactant solution in the continuous flow, with the inset as an image of the dripping behavior within the device. B) Dripping behavior generated monodispersed beads; C) monodispersed bead size is quantified over 100 beads. D) Beads were infused with tris(4,7-diphenyl-1,10-phenanthroline) ruthenium(II) dichloride to generate optical oxygen microsensors.

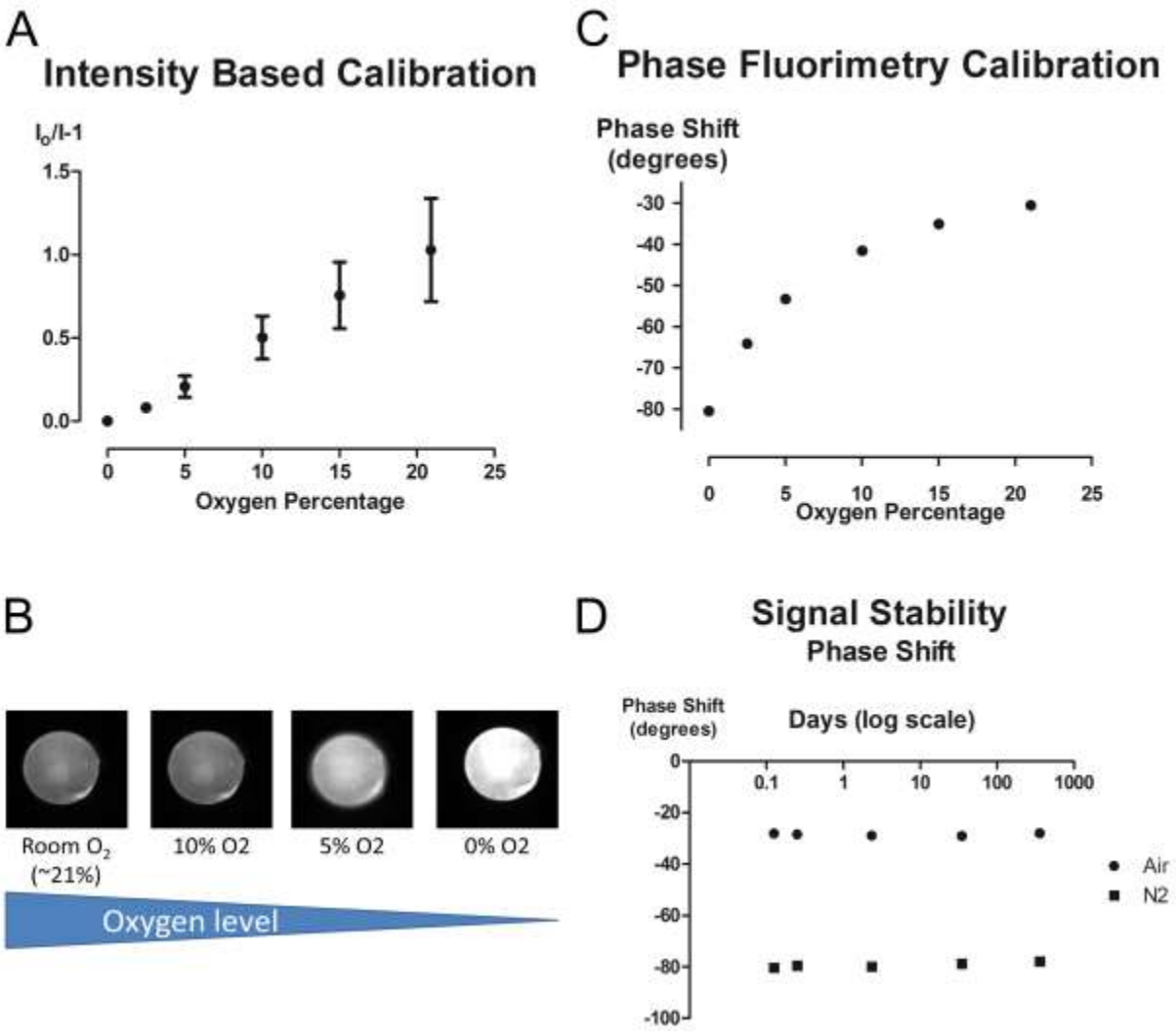

Figure 5-2: Oxygen responsivity of microsensors.
A) Intensity-based quenching calibration curve in response to different oxygen levels plotted according to Stern-Volmer relationship ($I_o/I-1$), error bars presented are standard deviation. B) Intensity change of a microsensor as a reponse to different oxygen levels; error bars presented are standard deviation (n=20). C) Phase fluorimetry calibration curve; error bars presented are standard deviation, however, they cannot be seen (n=20). D) Phase fluorimetry demonstrates stability in phase shift between normoxic and anoxic conditions, data from (n = 5) beads monitored over the course of one year.

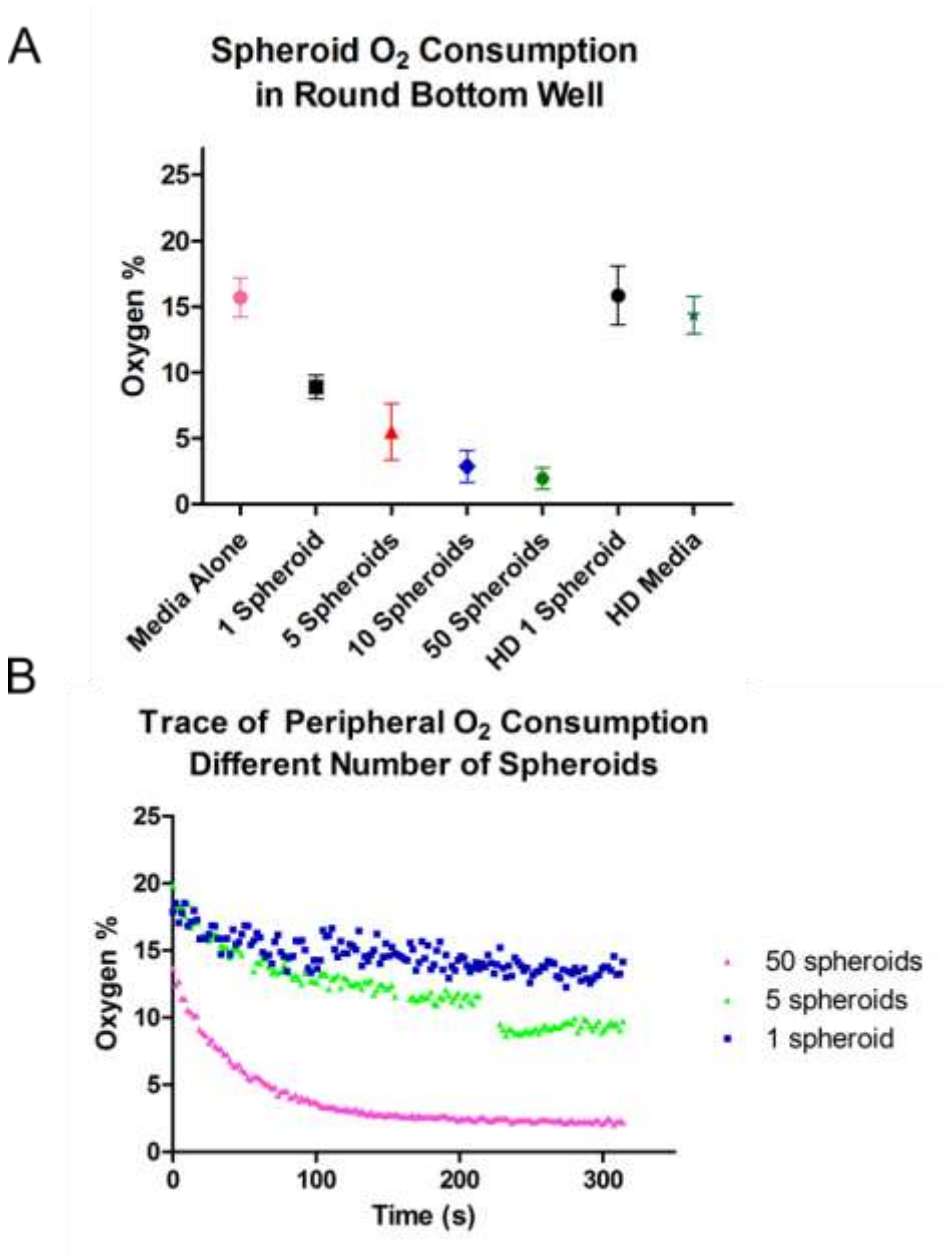

Figure 5-3: Oxygen Levels as a function of cell mass and culture vessel.
A) Microsensors were placed into 96 round-bottom well plate wells with 0 (media control), 1, 5, 10, or 50 spheroids or into hanging drops with one spheroid, or just media (control). Samples were observed over 18 hours, with the stabilized oxygen values presented for 18 hours. Oxygen measurements were averaged per sample well together regardless of microsensor position in regards to cell mass to generate an oxygen level per well, n = 4 well samples assessed per condition. B) Oxygen levels monitored after mixing media, in an effort to increase oxygen distribution, and watch oxygen consumption over time, demonstrating real-time continuous measurement capability of microsensors. Continuous oxygen measurements were presented for microsensors on the periphery of the cell mass.

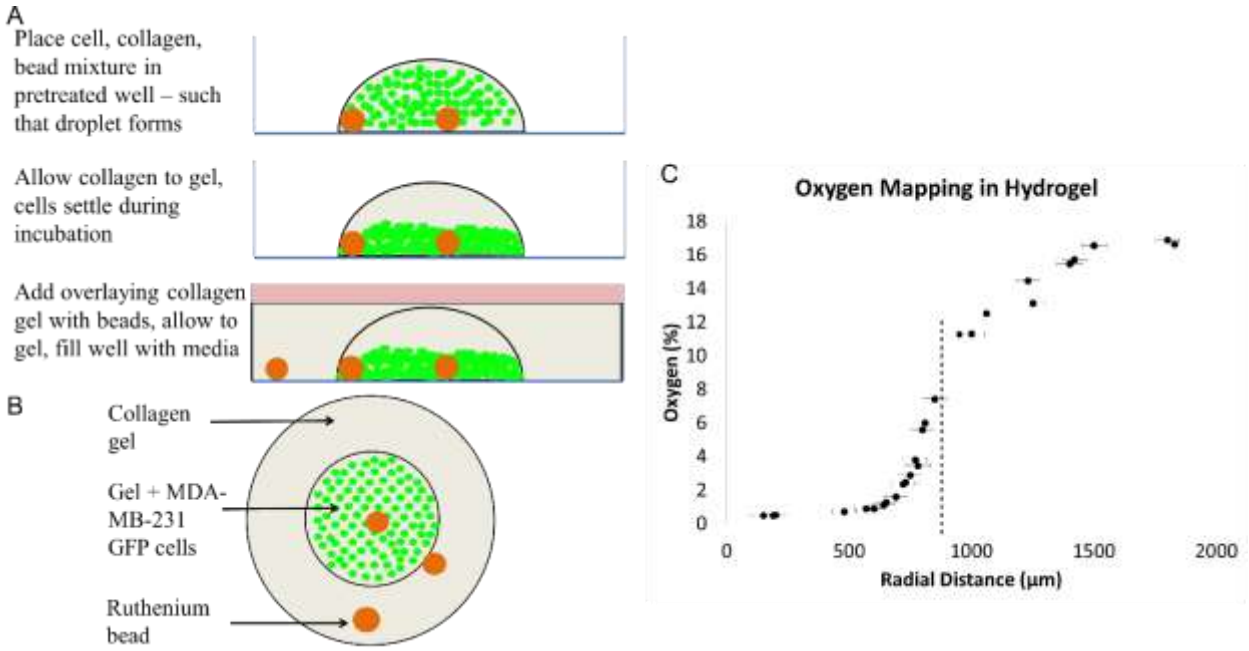

Figure 5-4: Mapping cell-generated oxygen gradients.
A) Side view schematic of the chronological process for spatial patterning, where a cell-laden hydrogel core is enveloped by a cell-free overlaying gel. Microsensors are dispersed within the two hydrogel regions. B) Top down view of spatial pattern. C) Oxygen measurements throughout the 3D tissue culture, cell-laden/-free border is demarcated by the dotted line at 925 µm.

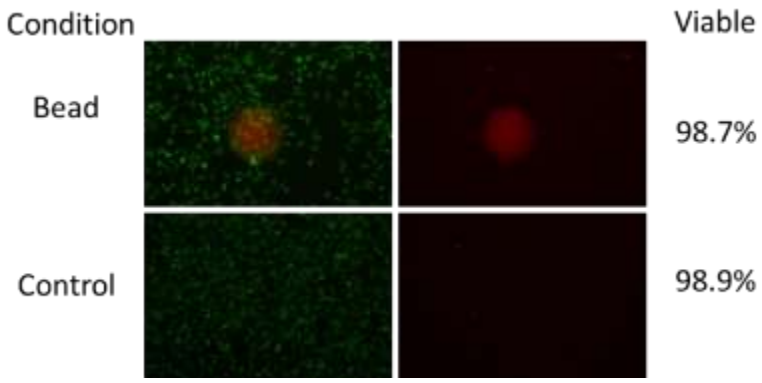

Figure 5-5: Microsensors demonstrate no cytotoxicity.
Live/dead stain for HS-5 cells cultured with microsensors for 36 hours, quantified percent viability present for microsensor treated samples or control samples.

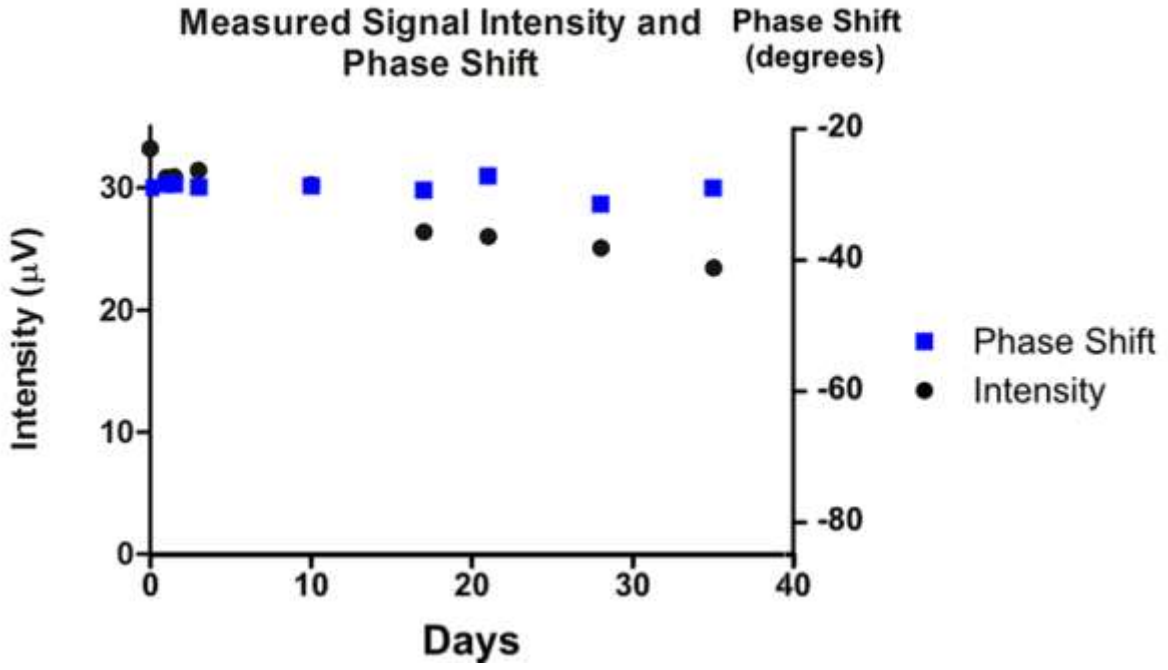

Figure 5-6: Microsensor intensity reduction over 35 days compared to phase shift signal data. All data was collected from one bead at 21% oxygen, in ambient conditions, microsensor was exposed to intermittent light as it was kept in microscopy room.

	Intensity Reduction	Phase Shift Change
Average % Difference	22.5226132	2.39619997
Standard Deviation	14.9849286	1.26419388

Table 5-1: Percent intensity reduction and percent phase shift fluctuations of microsensors
Percent intensity reduction and percent phase shift fluctuations of microsensors after one week of light exposure. Percent difference between day 1 and day 7, were determine for n = 15 microsensors.

Chapter 6: Conclusions and Future Direction:

6.1 Summary

An enduring challenge for translating technological or therapeutic innovations from preclinical studies into clinical use is the misinterpretation or lack of translatability of preclinical data from cell culture and animal models [1]. For example, the drug development process has become increasingly inefficient with billion dollar investments required to fill pharma drug development pipelines. These inefficiencies of therapeutic innovations stem from various areas, one of which is the model systems being used to collect the data. Recently there has been a substantial interest in the development of complex *in vitro* surrogate systems. The possibility of producing these systems has been fuelled in large part by novel micro-engineering toolsets and tissue engineering advances. The development of engineered tissues as model systems has partially bridged the gap, between *in vitro* and *in vivo* models, and recent efforts have focused on making these models more relevant by creating an organ-like microenvironment. Microengineered strategies provide a number of unique advantages and benefits in studying organ biology. The ability to pattern relatively large surfaces with subcellular resolution features allows precise control over various aspects of the cellular microenvironment, while maintaining the size necessary to allow for complex interactions between system components. These microscale systems are made to mimic sufficient native microenvironmental cues to induce the tissue cultures within them to behave in a manner representative of an organ or complex tissue system, achieving *in vitro* surrogate model systems [2].

The development of these surrogate model systems is highly dependent on various aspects, such as their adoptability, reproducibility, scalability, and manufacturability. Furthermore, as these surrogate models are still being designed and developed, it is critical to effectively characterize them such that they can quickly evolve into enabling technologies for preclinical research. This dissertation research contributed to developing microscale toolsets to enhance the ability to manipulate, control, and monitor the cellular microenvironment within microfluidic devices and microscale tissue cultures. These toolsets provide the integration of readily quantifiable and biologically meaningful measurement capabilities into these microfluidic systems. The described work was focused on microscale tissue culture enhancing technologies; however, a large effort in all our presented technologies, previously understated, was to produce highly reproducible and easily translatable systems. Specifically this led to robust predictability, easy implementation, simple tunability of the systems, or a combination of these parameters for each technology presented.

In Chapter 2 we describe the ability to elicit distinct duty cycles from the same self-regulating microfluidic oscillator device without needing to redesign the device architecture [3]. Biological and physiological systems are fundamentally regulated by oscillatory processes operating at discrete spatial and temporal scales, such that this work results in improved usability of previously described microfluidic oscillators. We reported a novel approach to realize this using the coordinated modulation of input volumetric flow rate ratio and fluidic capacitance ratio. The demonstration of this user-defined duty cycle control uses a straightforward experimental system where fluid inflow to the oscillator is provided by two syringes (of symmetric or asymmetric cross-sectional area) mounted upon a single syringe pump applying pressure across both syringes at a constant linear velocity. This produces distinct volumetric outflow rates from each syringe

that are proportional to the ratio between their cross-sectional areas. The difference in syringe cross-sectional area also leads to differences in fluidic capacitance; this underappreciated capacitive difference allows us to present a simplified expression to determine the microfluidic oscillators duty cycle as a function of cross-sectional area. The significance of this work, provides the end-user a simple method to produce predictable and robust duty cycles within self-regulating microfluidic oscillator.

In Chapter 3, we provide a practical solution to problems of variability between identically-designed autonomous microfluidic oscillators. Device-to-device oscillation variability arises due to inconsistencies in fabrication, materials, and operation conditions. This work demonstrates, experimentally and theoretically, that by coupling these devices via an appropriate capacitive unit, these microfluidic oscillators can be synchronized. The size and characteristics of the capacitive link needed and the range of input flow rate differences that can be synchronized are also characterized. Interestingly, in addition to synchronization, the oscillation stability of each coupled oscillator also improves upon oscillator coupling. As long as the coupling strength meets the minimum requirement for a system, it is also possible to couple and synchronize an array of more than two oscillators. The ability to synchronize multiple autonomous oscillators is a first step towards enhancing their usefulness as tools for biomedical research applications where multiplicate experiments with identical conditions are required.

In Chapter 4, we provide a low cost, improvement on standardizing three-dimensional spheroid tissue cultures [4]. We discuss the role that circularity and compaction has on spheroids, and demonstrate the impact MethoCel and collagen additives in the culture media can contribute to more compact and circular spheroid morphology. Furthermore, we demonstrate that improved spheroid formation is not a simple function of increased viscosity of the different macromolecule

additives, suggesting that other macromolecular characteristics contribute to improved spheroid formation. Of the various macromolecular additives tested for hanging drop culture, MethoCel provided the most desirable spheroid formation. These results indicate, the low cost macromolecular supplement, can improve the reproducibility of compact, circular spheroids, which contributes to standardizing and increasing the fidelity of the desired gradient profiles in these drug screening three-dimensional tissue cultures.

In Chapter 5, we describe the development of dispersible PDMS microbeads infused with oxygen sensitive ruthenium dye, to be used as optical oxygen microsensors. These oxygen microsensors are biocompatible and because of their size and geometric configuration can be readily dispersed into different tissue culture vessels or in vitro generated 3D tissues. Using phase fluorimetry as the imaging modality allows the microsensors to be used as real-time, continuous oxygen microsensors, circumventing the optical interference of different culture platforms, as well as the issues that intensity-dependent measurements would have with continuous monitoring, i.e. photobleaching. We demonstrate the use of our developed microsensors to measure in vitro oxygen levels in different culture formats, observing oxygen depletion in media surrounding different cell aggregate masses. We also demonstrated the utility of the microsensors by mapping the oxygen profile of a spatially-patterned cell laden 3D hydrogel. These microsensors have the potential of being implemented into culture systems such as bioreactors, organoid cultures, and 3D organ-on-a-chip systems.

6.2 Limitations

The work presented in this dissertation covered a broad range of technologies focused on improving in vitro cultures and analytical assessment of these tissues culture systems. The technologies described, specifically microfluidic oscillators (Chapters 2 and 3) and oxygen microsensors (Chapter 5), are still in the process of being developed and consequently still have limitations associated with them. In this section we highlight the limitations of these technology platforms to elucidate potential obstacles to the reader, and ideally producing new ideas and work for the future trajectory of these technologies. We chose to not focus on limitations of technologies presented in Chapter 4, low cost, improvement on standardizing three-dimensional spheroid tissue cultures, because this work was in large part only limited to the amount of cells and supplement types we tested to improve the reproducible generation of three-dimensional spheroid tissue cultures. We identified this as a challenge for scaling multiplicate experiments, such that researchers can identify the best supplement formulation for their experimental designs, not specifically a technical challenge limiting the technologies utility and implementation.

Microfluidic self-regulated circuits, and specifically microfluidic oscillators, provide a platform, which researchers and industrial developers can design devices based on preset principles similar to electronic circuits, however, there are several gaps of knowledge in this hydro-electronic analogy that need to be filled in order to further the pre-design process of these microfluidic circuits. First, not all components are fully characterized to fully identify how the fluidic components respond to system feedback, or complex feedback loops. Additionally, the dynamic range of the components is not yet known and needs to be determined to understand what the margin of error tolerated by devices such that they can perform as designed. Currently, this limits our ability to adequately design and fabricate these self-regulated devices, as well as consider

building modular components that can interact together, similar to electronics. Recent work has gone on to characterize external capacitors [5], the role of normally closed valves and the associated pressure thresholds of the valves [6–8]. However, there is still a gap in understanding of the components, limiting the ability to produce more complex circuits while increase the fidelity between the theoretical models and the empirical results.

Within this dissertation we only present constant-volumetric flow rate-driven oscillators, these systems are driven by fluctuating input pressures, limiting the ability to have parallel output flows with different flow-switching periods. This is because the input pressures of the flow-driven oscillators connected in parallel fluctuates synchronously, such that parallel output flows with different flow-switching suffer severe crosstalk or are just not possible with devices in their current forms, limiting the ability to scale these devices into more complex systems.

Additionally, current devices are limited in the type of chemical, output signals they would present to cells, where the stimulant concentration profiles are square waves. These waveforms are not present in oscillatory biochemical processes, where in vivo waveforms tend to be more similar to sinusoidal waveforms. The current concentration square-wave profiles may recapitulate timing of periods or stimulant exposure, however, they still lack concentration ramping of a stimulant as seen in vivo, which would be captured by sinusoidal waveforms, or at a minimum triangular or saw-tooth waveforms.

Finally, all devices used were made manually in small batches, however, for this technology platform to grow, more sophisticated fabrication techniques are needed to ensure proper alignment of individual layers, uniform thickness of elastic membranes, and consistent feature dimensions. Beyond the reproducibility, the size of batch fabrication needs to increase in scale. Achieving these criteria, we would maximize the translation of these technologies into more

laboratory settings. Furthermore, material properties such as stiffness and stickiness, especially important for valve units, have a direct effect on how the fluid pressurizes and depressurizes features in the valve components. PDMS was used in our work, because it is an ideal material for prototyping in the lab, however, its material properties change over time, resulting in differential mechanical properties depending on the time since fabrication of the device. PDMS stickiness also changes over time if static but will differentially change when exposed to proteins or water for extended periods of time. Shifts in mechanical properties of the devices, generally in the membranes, limit the longevity of these devices to perform in a time-independent manner. This requires the identification and incorporation of new materials for these systems to become sufficiently reliable within research setting beyond the first few weeks after fabrication. Finally moving away from PDMS would minimize specific issues within cell culturing, which are the evaporation of water through nanoporous PDMS [9], and also the incorporation of PDMS oligomers into cellular membranes [10].

The developed dispersible oxygen microsensors, provided a technology for oxygen measurements for different cell culture environments and also within three-dimensional hydrogel tissue cultures. Currently the system is limited due to the efficiency of the fabrication process, there is a reasonable loss (~25%) of microsensors during fabrication. Additionally, infusing a high-level of ruthenium, such that all microsensors generated would remain functional for a minimum of one year would be ideal. This high-level infusion would also enhance our ability to produce smaller microsensors, as smaller microsensors (< 25 μm) generally don't generate enough signal to capture via our photo-detection setup. Generation of brighter, smaller sensors would increase the diversity of culture systems our microsensors could be incorporated into. Finally, by improving the infusion technique, using brighter sensors, would allow us to measure

in more culture platforms, as well as in thicker in vitro generated tissues and potentially within small animals.

The distribution of the microsensors is generally done passively by adding them into the different cultures via media. Active placement has been done manually, but is time consuming and inefficient. Developing an active method to easily array or move the microsensors would allow researchers to array in beads to the desired configurations, increasing the potential of mapping different culture vessels, without worrying about the vessels geometry and microsensor settling.

The oxygen measurement system has a minor limitation for translating our microsensor technology to more labs, due to the hardware being uncommon in most biology labs, restricting the ease of translation.

6.3 Future work

The next steps for technologies in this dissertation is additional validation and adoption on a larger scale, and into a diverse range of research labs. Considering areas of growth for microfluidic oscillators and microsensors, applications into biological systems is a priority. However, both of these technologies have exciting next generation extensions beyond increasing their application in wet lab settings.

Seven next steps that I see as key areas for further development of the microfluidic actuators are the following: 1) Generation of new concentration signal waveforms; 2) Producing tunable velocity profiles across cells, allowing researchers to tune shear stress applied to cells without limiting the performance of microfluidic actuators; 3) Further developing and characterizing coupling mechanisms and connection systems between different microfluidic units, and understanding the feedback and influence of connecting these units with each other; 4) Increasing the complexity of function (i.e. built in timing delays, multi-functional units) via modular combination of microfluidic units; 5) Begin developing new electrohydraulic components parallel to the development of electronic systems such as a memristor [11,12] fluidic analog; 6) Enhancing the user-friendliness of these systems and generating a how-to guide for other researchers to support the translation of these devices out of microtechnology labs and into biomedical research; 7) Introduction of new materials to improve fidelity of theoretical responses over time, and in device to device variability.

The different directions for the future work of the microactuators are not mutually exclusive, and could be investigated in combination. If given the opportunity to continue advancing this work, I would pursue steps 1), 3), 4) for microfluidic actuators. Generating new wave forms (1) such as sinusoidal, or even sawtooth waveforms would allow recapitulation of a more physiological

stimulus profile. Step 3) I believe is critical to accomplish step 4), by not having an informed understanding of different interactions between microfluidic units, the ability to develop interacting modules would be greatly limited. By accomplishing both step 3) and 4) the barrier to translate these microactuators would be reduced by having defined components that could be "clicked" together to produce a desired output. Successful implementation of steps 3) and 4) would produce a microfluidic systems with high utility for biologists with a low barrier of adoption. With this development, I envision step 6) to be an obvious progression that would arise because of the expected utility of these modular units.

Future work building off of the developed oxygen microsensors, could be focused in six directions: 1) Improved efficiency in the fabrication process; 2) Incorporation into a more diverse set of tissue cultures; 3) Assess the ability of the microsensors to work within larger/thicker tissue constructs; 4) Implant them within tumor precursors or regenerative scaffolds into mice and assess the ability to track oxygen changes within the tissues and then confirm the corresponding blood vessel formation; 5) Implement microsensors within oxygen modulating microfluidic culture systems to assess aerotaxis of cancer (or other) cells, to monitor oxygen levels and respective cell migration response; 6) Develop microsensors to measure secondary targets, such as but not limited to nitrogen oxide, glucose, glutamine, or pH.

Similar to the microfluidic actuators, the different directions for the future work of the microsensors are not mutually exclusive, and could be investigated in combination. If given the opportunity to continue advancing the microsensors, I would pursue directions 4) and 5). The ability to use the oxygen microsensors to assess responses within *in vivo* tissues, would satisfy direction 3), while providing us a technology to build *in vitro* tissues, assess their oxygen profiles prior to implantation, and then monitor the response of vascularization, within these implants.

Assuming we could retrieve the tissues for further assessment, this could be a highly useful tool to assess real-time the implant integration into the host, this would be especially useful within the regenerative medicine field. Direction 5) provides a unique area, the migratory response of cells to oxygen, which seems to have limited studies. By employing discrete, validated microsensors, we could have real-time continuous verification of the *in vitro* oxygen levels, while monitoring the cellular migratory response. I specifically envision doing this work with an oxygen controlling microfluidic platform, similar to those recently published [13,14].

Collectively this continued research with microfluidic actuators and microsensors would further enhance these tools for the microenvironmental control and monitoring of *in vitro* (and potentially *in vivo*) model systems. By further validating them or progressing them forward as discussed in future work, I expect they could reach broader audiences and improve *in vitro* model systems.

6.4 References

[1] Begley CG, Ellis LM. Drug development: Raise standards for preclinical cancer research. Nature 2012;483:531–3. doi:10.1038/483531a.

[2] Moraes C, Mehta G, Lesher-Perez SC, Takayama S. Organs-on-a-Chip: A Focus on Compartmentalized Microdevices. Ann Biomed Eng 2011;40:1211–27. doi:10.1007/s10439-011-0455-6.

[3] Lesher-Perez SC, Weerappuli P, Kim S-J, Zhang C, Takayama S. Predictable Duty Cycle Modulation through Coupled Pairing of Syringes with Microfluidic Oscillators. Micromachines 2014;5:1254–69. doi:10.3390/mi5041254.

[4] Leung BM, Lesher-Perez SC, Matsuoka T, Moraes C, Takayama S. Media additives to promote spheroid circularity and compactness in hanging drop platform. Biomater Sci 2015;3:336–44. doi:10.1039/C4BM00319E.

[5] Kim S-J, Yokokawa R, Takayama S. Microfluidic oscillators with widely tunable periods. Lab Chip 2013;13:1644–8. doi:10.1039/C3LC41415A.

[6] Kim S-J, Yokokawa R, Lesher-Perez SC, Takayama S. Constant Flow-Driven Microfluidic Oscillator for Different Duty Cycles. Anal Chem 2012;84:1152–6. doi:10.1021/ac202866b.

[7] Shin J, Park H, Dang VB, Kim C-W, Kim S-J. Elastomeric microfluidic valve with low, constant opening threshold pressure. RSC Adv 2015;5:23239–45. doi:10.1039/C4RA16696E.

[8] Kim S-J, Yokokawa R, Takayama S. Analyzing threshold pressure limitations in microfluidic transistors for self-regulated microfluidic circuits. Appl Phys Lett 2012;101. doi:10.1063/1.4769985.

[9] Heo YS, Cabrera LM, Song JW, Futai N, Tung Y-C, Smith GD, et al. Characterization and Resolution of Evaporation-Mediated Osmolality Shifts That Constrain Microfluidic Cell Culture in Poly(dimethylsiloxane) Devices. Anal Chem 2007;79:1126–34. doi:10.1021/ac061990v.

[10] Regehr KJ, Domenech M, Koepsel JT, Carver KC, Ellison-Zelski SJ, Murphy WL, et al. Biological implications of polydimethylsiloxane-based microfluidic cell culture. Lab Chip 2009;9:2132–9. doi:10.1039/b903043c.

[11] Garcia-Redondo F, Lopez-Vallejo M, Ituero P. Building Memristor Applications: From Device Model to Circuit Design. IEEE Trans Nanotechnol 2014;13:1154–62. doi:10.1109/TNANO.2014.2345093.

[12] Chua LO. Memristor-The missing circuit element. IEEE Trans Circuit Theory 1971;18:507–19. doi:10.1109/TCT.1971.1083337.

[13] Brennan MD, Rexius-Hall ML, Elgass LJ, Eddington DT. Oxygen control with microfluidics. Lab Chip 2014;14:4305–18. doi:10.1039/C4LC00853G.

[14] Lo JF, Sinkala E, Eddington DT. Oxygen gradients for open well cellular cultures via microfluidic substrates. Lab Chip 2010;10:2394–401. doi:10.1039/C004660D.